KERNFORSCHUNGSANLAGE JÜLICH GmbH
Institut für Kernphysik

LARGE AMPLITUDE NUCLEAR COLLECTIVE MOTION AND THE QUANTIZED ATDHF THEORY

by

D. Provoost

Jül – Spez – 348
March 1986
ISSN 0343–7639

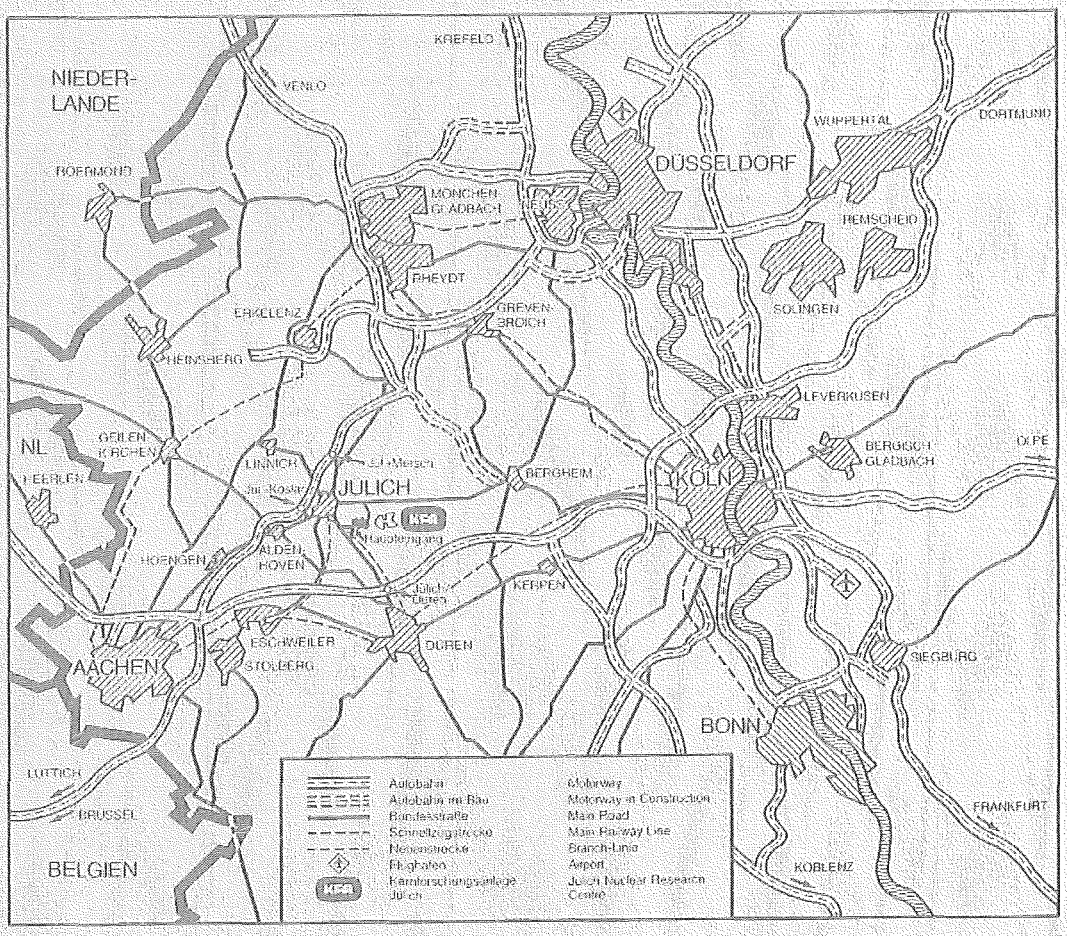

Als Manuskript gedruckt

Spezielle Berichte der Kernforschungsanlage Jülich – Nr. 348

Institut für Kernphysik Jül – Spez – 348

Zu beziehen durch: ZENTRALBIBLIOTHEK der Kernforschungsanlage Jülich GmbH

Postfach 1913 · D-5170 Jülich (Bundesrepublik Deutschland)

Telefon: 02461/610 · Telex: 833556-0 kf d

LARGE AMPLITUDE NUCLEAR COLLECTIVE MOTION AND THE QUANTIZED ATDHF THEORY

by

D. Provoost

Table of Contents

	page
INTRODUCTION	1
THEORY	4
1. The Adiabatic Time-Dependent Hartree-Fock Theory (ATDHF)	5
2. The Generator Coordinate Method (GCM)	8
3. The Quantized Adiabatic Time-Dependent Hartree-Fock Theory (qATDHF)	14
3.1 Theoretical Formalism	14
3.2 Practical Method of Solution	18
The $\alpha+^{16}O \leftrightarrow {}^{20}Ne$ System	22
1. Introduction	23
2. Static Properties of the α, ^{16}O and ^{20}Ne Systems	25
3. The Collective Path α-^{16}O	29
4. The Collective Coordinates	32
5. Solution of the Schrödinger Equation for Bound States and Resonances	38
6. GCM Structure Calculations	45
7. GCM Scattering Calculations	50
8. Poles and Decay Widths	55
9. Inclusion of Other Structural Configurations	58
The $\alpha+\alpha \leftrightarrow {}^{8}Be$ System	61
1. Introduction	62
2. GCM Structure Calculations	64
3. GCM Scattering Calculations	67
4. The Breathing Mode of 1 α-Particle	71
The $\alpha+^{12}C$ Structure of ^{16}O	74
1. Introduction	75
2. Approximate Projection of ^{12}C on 0^+	76
3. The Collective Paths	78
4. GCM Structure and Scattering Calculation	81
Appendix A1: Angular Momentum Projection Calculations on a Grid	87
A. Grid	88
B. Representation on a Grid	89
C. Eigenvalues and Eigenvectors of L_z	91
D. Completeness Relations	95

page

E. Example 97
F. Rotations 100
G. Example 104
H. Angular Momentum Projection 111
I. Calculation of Matrix Elements $\langle \phi | \hat{H} | \psi \rangle$ with the BKN and Skyrme-Type Forces 113
J. Numerical Example 117
K. Hartree-Fock Spectra of Deformed Light Nuclei with BKN, Modified BKN and Skyrme-Type Forces 120

Appendix A2: Elimination of Linear Dependence in the GCM Matrix Equation 125

Conclusions 129

References 133

Acknowledgements 140

INTRODUCTION

It was an objective for nuclear theory for many years to explain by microscopic means why the pure phenomenological liquid drop model, on one hand, and the shell model, on the other hand, were both successful in describing various nuclear properties. In this context the concept of a mean field played a dominant role because the Hartree-Fock approximation was able to link both models, although totally different from concept, in showing the importance of the coupling of the single particle degrees of freedom to the generated mean field. HF therefore gave basically the microscopic foundation to the shell model.

The collective model which is the dynamic extension of the liquid drop model also incorporates the correlation of the single nucleons with their own mean field. One may therefore expect that dynamic microscopic theories for the description of nuclear collective motion, which are related to the HF approximation, will be suited to give the microscopic foundation to the collective model.

One such approach is the Time-Dependent Hartree-Fock theory (TDHF) with a time-varying Slater determinant. Its small amplitude limit, the Random Phase Approximation, has given numerical results for certain types of collective motion which are in remarkable agreement with the experimental data. However, not only have many modes of collective motion a large amplitude, e.g. fission, fusion and soft vibrations, but already on the conceptual level the TDHF formalism does not allow to extract quantum-mechanical information, like scattering phase shifts or quantized vibrational energies. Indeed, TDHF is an initial value problem and hence not applicable to boundary value problems. Other approaches are more concentrated on large amplitude and slow collective phe-

nomena, these include various adiabatic theories and in particular the quantized Adiabatic Time-Dependent Hartree-Fock (ATDHF). It has been derived starting from the same variational principle as in TDHF and leads to the construction of an optimal, maximally decoupled, collective path, i.e. the set of wave functions which form the substratum along which the collective motion evolves. From this a unique collective Hamiltonian has been constructed, in analogy with the Bohr-Mottelson concepts, with an outcome which does not depend on the actual choice of the collective coordinate. This derivation of the collective Hamiltonian corresponds to a quantization of classical quantities. There exists, however, a theory, the Generator Coordinate Method, which is from the conceptual point of view completely quantum-mechanical. It diagonalizes the total Hamiltonian H in the subspace spanned by some nonorthogonal basis and the resulting Griffin-Hill-Wheeler equation can be solved for scattering states and structure states. This equation can also be transformed to a Schrödinger equation. Deficiencies are, however, that one needs a preconceived knowledge about the basis, and the mass parameter in the Schrödinger equation does not reproduce the correct value for pure translational motion if one uses Slater determinants as generating states.

However, it has been shown that the equation of the collective path in qATDHF can be derived starting from a GCM ansatz with a pair of conjugate collective parameters. The GCM, which has been proven to be a very useful technique, and this not only in nuclear physics, is therefore extended to a fully microscopic description of nuclear structure and phenomena with the nucleon-nucleon interaction as only input.

It is the aim of the present work to present some numerical results obtained within the ATDHF formalism. Both approaches have been considered, the con-

struction of the collective Hamiltonian as well as the solution of the Griffin-Hill-Wheeler equation, both using the ATDHF collective path. We want to show that a fully selfconsistent microscopic description of nuclear phenomena using general many-body techniques can be treated on the numerical level. We considered several different systems to indicate as much as possible the present possibilities and limits of the theory as well as of the numerical techniques.

THEORY

1. The Adiabatic Time-Dependent Hartree-Fock Theory (ATDHF)

There is a wealth of publications leading to the ATDHF equations, e.g. (Br76,Vi77,Ba78,Go78,Di86). All these derivations start from the TDHF time integral for the Slater-determinantal wave function $\Psi(t)$

$$I = \int_{t_1}^{t_2} \langle \Psi(t) | H - i\hbar \frac{\partial}{\partial t} | \Psi(t) \rangle dt \qquad (T1)$$

$$\delta\Psi(t_1) = \delta\Psi(t_2) = 0$$

where the stationary condition $\delta I=0$ leads to the TDHF equation which in the one-body density matrix notation looks like:

$$\boxed{i\hbar \frac{\partial \rho}{\partial t} = [W,\rho]} \qquad (T2)$$

$$\langle \alpha | W | \gamma \rangle = \langle \alpha | \hat{T} | \gamma \rangle + \sum_{\beta\delta} \langle \alpha\beta | \tilde{V} | \gamma\delta \rangle \rho_{\delta\beta}$$

with $\hat{T}$ the kinetic energy operator and $\langle \alpha\beta | \tilde{V} | \gamma\delta \rangle$ the antisymmetrized matrix element of the interaction $\hat{V}$ (if only effective two-body interactions are included into the Hamiltonian).

The adiabatic approximation to (T2) then starts with the decomposition

$$\rho(t) = e^{-i\chi(t)} \rho_0(t) e^{i\chi(t)} \qquad (T3)$$

where the single particle operators ρ_0 and χ are both hermitian and time-even. M.J. Giannoni (Gi81) has shown that the condition

$$\| \rho - \rho_T \| < 1$$

is necessary and sufficient for the existence of such a set ρ_o and χ. ρ_T means the time reverse of ρ where the norm has to be interpreted as

$$\|\rho\| = \sup_{|u\rangle \in \mathcal{H}} \frac{\|\rho|u\rangle\|}{\|\,|u\rangle\|}$$

Uniqueness can be achieved by the requirements

$\rho_o\chi + \chi\rho_o = \chi$ which means that χ has only ph elements with respect to ρ_o

all eigenvalues of χ lie within the interval $]-\frac{\pi}{4}, \frac{\pi}{4}[$

The condition $\|\rho-\rho_T\| < 1$ is valid for slow motion since then the wave function is almost in static equilibrium at all times and hence ρ must be almost the same as the time reverse motion ρ_T.

Expansion of (T2) in orders of χ leads to the ATDHF equations (up to second order) by separation of the time-even from the time-odd part:

$$\boxed{\begin{aligned} i\dot{\rho}_o &= [W_o,\rho_1] + [W_1,\rho_o] \\ \\ i\dot{\rho}_1 &= [W_o,\rho_o] + [W_o,\rho_2] + [W_1,\rho_1] + [W_2,\rho_o] \end{aligned}} \qquad (T4)$$

with

$$\rho_1 = i\,[\chi,\rho_o]$$
$$\rho_2 = -\frac{1}{2}\,[\chi,[\chi,\rho_o]]$$
$$W_o = \hat{T} + \mathrm{Tr}\;\tilde{V}\,\rho_o$$
$$W_1 = \mathrm{Tr}\;\tilde{V}\,\rho_1$$
$$W_2 = \mathrm{Tr}\;\tilde{V}\,\rho_2$$

Baranger and Véneroni (Ba78) have shown the classical nature of these equations, namely they can be obtained as Hamilton equations from the adiabatic Lagrangian whose zeroth order term is the collective potential energy

$$V(\rho_o) = \mathrm{Tr}\ \hat{T}\ \rho_o + \frac{1}{2}\ \mathrm{Tr}\ \mathrm{Tr}\ \rho_o\ \tilde{V}\ \rho_o$$

and the quadratic term is identified with the kinetic energy

$$K = \mathrm{Tr}\ W_o\ \rho_2 + \frac{1}{2}\ \mathrm{Tr}\ \mathrm{Tr}\ \rho_1\ \tilde{V}\ \rho_1$$

The second eqution of (T4) can also be obtained in the Lagrangian formalism.

It is further possible to obtain the RPA equations in the small amplitude limit by neglecting all terms of second order in (T4) and requiring ρ_o to be almost equal to the static Hartree-Fock solution.

Due to the close contact with the classical model the drawback of these derivations however is that one has to requantize the collective Hamiltonian which entails errors and arbitrariness problems.

There is however a theory, the Generator Coordinate Method, which is quantal right from the beginning such that no a posteriori quantization is necessary.

In the next section we will go deeper into this method before presenting the quantized ATDHF theory (qATDHF), because it is possible to derive the qATDHF equations starting from a general GCM ansatz.

2. The Generator Coordinate Method (GCM)

The usual GCM (HW53,GW57) starts with the assumption of some preconceived knowledge about the model wave functions

$$\phi(\bar{x}_1 \ldots \bar{x}_A, \alpha) \tag{T5}$$

which are in general nonorthogonal and depend on one or more "collective" parameters α (spin and isospin labels are contained in the x notation). The calculations are performed in the model Hilbert-space generated by linear combinations of the wave functions (T5)

$$\psi(\bar{x}_1 \ldots \bar{x}_A) = \int \phi(\bar{x}_1 \ldots \bar{x}_A, \alpha) f(\alpha) d\alpha \tag{T6}$$

where $f(\alpha)$ is called the Hill-Wheeler weight function and α the generator coordinate.

Requiring ψ to be a solution of the Schrödinger equation in the model space

$$\int d\bar{x}_1 \ldots d\bar{x}_A \; \phi(\bar{x}_1 \ldots \bar{x}_A, \alpha)[\hat{H}-E]\psi(\bar{x}_1 \ldots \bar{x}_A) = 0 \tag{T7}$$

leads to the well known Griffin-Hill-Wheeler equation

$$\boxed{\int d\alpha \; [H(\alpha',\alpha) - EN(\alpha',\alpha)]f(\alpha) = 0} \qquad \forall\, \alpha' \tag{T8}$$

which destinates the weight function f, the kernels are defined through

$$H(\alpha',\alpha) = \langle \phi(\alpha')| \hat{H} |\phi(\alpha)\rangle$$
$$N(\alpha',\alpha) = \langle \phi(\alpha')| \phi(\alpha)\rangle \qquad \text{(T9)}$$

According to J. Broeckhove and E. Deumens (BD79) at least one discrete countable set of α_i, $i = 1,2,\ldots$ can be found which generates the same Hilbert space as the continuous variational basis. Therefore (T6) can be replaced by

$$\psi(\bar{x}_1 \ldots \bar{x}_A) = \sum_{i=1}^{\infty} c_i \, \phi(\bar{x}_1 \ldots \bar{x}_A, \alpha_i) \qquad \text{(T10)}$$

and the Hill-Wheeler equation (T8) becomes

$$\boxed{\sum_{j=1}^{\infty} (H_{ij} - E N_{ij}) c_j = 0} \qquad \text{(T11)}$$

which is the usual employed discretized version of (T8).

If now the following 3 conditions are fulfilled:

i) The generator coordinate α is a real vector with 3 components $\bar{\alpha}$.

ii) The Hamilton operator is invariant under rotations.

iii) Rotation in the Hilbert space $R_H(\Omega)$ is equivalent to rotation in the parameter space $R_p^{-1}(\Omega)$

$$R_H(\Omega) \, \phi(\bar{x}_1 \ldots \bar{x}_A, \bar{\alpha}) = \phi(\bar{x}_1 \ldots \bar{x}_A, R_p^{-1}(\Omega)\bar{\alpha})$$

then one can deduce the partial wave version

$$\boxed{\int_0^{\infty} d\alpha [H_\ell(\alpha',\alpha) - E N_\ell(\alpha',\alpha)] f_\ell(\alpha) \alpha^2 = 0 \quad \forall \alpha'} \qquad \text{(T12)}$$

and due to (iii) Ψ has the same rotational properties as the weight function f. The angular momentum of relative motion is a good quantum number and therefore the partial waves ℓ will be decoupled.

Condition iii) holds for spherical nuclei which will be studied in this work.

The discretized version of (T12) is straightforward.

This powerful GCM method has been applied as well for structure as for scattering calculations (Mi73,Bo75).

Structure calculations require square integrable wave functions. For true bound states no extra boundary condition is necessary. However, for quasi-bound states an extra boundary condition is necessary to obtain square integrable wave functions, therefore we restricted the discretization points up to a certain cut-off radius R_c.

For scattering calculations we follow the procedure of Hüsken, Wedekind and Weiguny (Hu77). They start with model wave functions for the 2 cluster system of the following type:

$$\phi(\bar{x}_1 \ldots \bar{x}_A \bar{\alpha}) = \psi_{CM}(\bar{R}_{CM})\, A\, \{\phi_1(\xi_1)\phi_2(\xi_2) I(\bar{x}, \bar{\alpha})\} \qquad \text{(T13)}$$

with $\bar{R}_{CM}$ the position of the centre of mass and $\bar{x}$ the relative coordinate between the 2 clusters

$$\bar{x} = \frac{1}{A_1} \sum_{i=1}^{A_1} \bar{x}_i - \frac{1}{A-A_1} \sum_{i=A_1+1}^{A} \bar{x}_i$$

ϕ_1 and ϕ_2 are the wave functions of the two clusters depending only on the internal coordinates ξ_1, ξ_2 respectively.

Making use of (T13) one obtains for (T6)

$$\psi(\bar{x}_1 \cdots \bar{x}_A) = \psi_{CM}(\bar{R}_{CM})\ A\{\phi_1(\xi_1)\phi_2(\xi_2) \int d\bar{\alpha}\ \Gamma(\bar{x},\bar{\alpha})f(\bar{\alpha})\} \tag{T14}$$

such that asymptotically

$$\psi(\bar{x}_1 \cdots \bar{x}_A) \underset{\|\bar{x}\| \to \infty}{\to} \psi_{CM}\ g(\bar{x})\phi_1(\xi_1)\phi_2(\xi_2) \tag{T15}$$

with the wave function of relative motion defined through

$$g(\bar{x}) = \int d\bar{\alpha}\ \Gamma(\bar{x},\bar{\alpha})f(\bar{\alpha}) \tag{T16}$$

The partial wave expansion

$$f(\bar{\alpha}) = \sum_{LM} Y_{LM}(\hat{\alpha})f_\ell(\alpha) \tag{T17}$$

and the definition

$$\int d\hat{x} \int d\hat{r}\ Y_{LM}(\hat{x})\Gamma(\bar{x},\bar{r})Y_{L'M'}(\hat{r}) = \delta_{LL'}\delta_{MM'}\Gamma_L(x,r) \tag{T18}$$

leads to the partial wave version of (T16)

$$g_\ell(x) = \int_0^\infty d\alpha\ \Gamma_\ell(x,\alpha)f_\ell(\alpha) \tag{T19}$$

We know that, studying scattering solutions, for x outside the range R_o of nuclear interaction and antisymmetrization,

$$g_\ell(x) \to F_\ell(x) + \mathrm{tg}\ \delta_\ell\ G_\ell(x) \tag{T20}$$

with F_ℓ and G_ℓ the well known regular and irregular Coulomb functions and δ_ℓ the nuclear phase shift.

One now splits the relative motion wave function $g_\ell(x)$ in two parts

$$g_\ell(x) = g_\ell^{sr}(x) + g_\ell^{as}(x) \tag{T21}$$

where $g_\ell^{sr}(x)$ is a square integrable function and g_ℓ^{as} describes asymptotically the right behaviour of the wave function. g_ℓ^{sr} can then be approximated to any desired accuracy through a finite sum (if Γ_ℓ is square integrable too) (Hu74)

$$\| g_\ell^{sr}(x) - \sum_{i=1}^{N} c_i^\ell\ \Gamma_\ell(x,\alpha_i) \| < \varepsilon \tag{T22}$$

and for g_ℓ^{as}

$$g_\ell^{as}(x) = \int_0^\infty d\alpha\ \Gamma_\ell(x,\alpha) f_\ell^{as}(\alpha) \tag{T23}$$

where f_ℓ^{as} is this function which after being folded according to (T19) yields (T20). The corresponding many-body wave function can then be written as

$$\psi_\ell(\bar{x}_1 \ldots \bar{x}_A) = \sum_{i=1}^{N} c_i^\ell\ \phi_\ell(\bar{x}_1 \ldots \bar{x}_A, \alpha_i) + \int_0^\infty d\alpha\ \phi_\ell(\bar{x}_1 \ldots \bar{x}_A \alpha) f_\ell^{as}(\alpha) \tag{T24}$$

Projecting the Schrödinger equation onto the subspace spanned by the functions $\phi_\ell(\bar{x}_1 \ldots \bar{x}_A, \alpha_i)$ $i = 1 \ldots N$

$$\langle \phi_\ell(\bar{x}_1 \ldots \bar{x}_A \alpha_i) | H-E | \psi_\ell(\bar{x}_1 \ldots \bar{x}_A) \rangle = 0 \qquad i=1 \ldots N \tag{T25}$$

leads to N equations for the N+1 unknowns c_i^ℓ i=1...N plus δ_ℓ coming from (T20):

$$\boxed{\begin{aligned}&\sum_{i=1}^{N} \{H_\ell(\alpha_j,\alpha_i) - E\, N_\ell(\alpha_j,\alpha_i)\}c_i^\ell \\ &= \int_0^\infty d\alpha\, \{H_\ell(\alpha_j,\alpha) - EN_\ell(\alpha_j,\alpha)\}f_\ell^{as}(\alpha)\end{aligned}} \qquad \text{(T26)}$$

To close this system of equations one requires the additional equation

$$g_\ell^{sr}(R_o) = 0 \qquad \text{(T27)}$$

Usually one takes $R_o = \alpha_N$ and discretizes the right hand side of eq. (T26).

3. The Quantized Adiabatic Time-Dependent Hartree-Fock Theory (qATDHF)

3.1 Theoretical Formalism

Goeke and Reinhardt (Go78) have shown however how to obtain a unique procedure for quantizing a collective Hamiltonian, here obtained within the ATDHF theory. The quantum-mechanical character is still clearer indeed by the possible derivation of the ATDHF equations within the GCM formalism (Re79) and (Go80). Since for translational motion ATDHF leads to the correct mass one has to start certainly with a pair of conjugate collective parameters,

$$\psi(\bar{x}_1 \ldots \bar{x}_A) = \int dq \int dp\, f(q,p)\phi_{qp}(\bar{x}_1 \ldots \bar{x}_A) \qquad \text{(T28)}$$

in the ansatz for the wave function describing the collective motion of the A-body nuclear system. The ϕ_{qp} are restricted to Slater-determinantal wave functions. Contrary to the usual GCM as prescribed in §2 we now want not only to obtain the superposition function f but also the set of Slater determinants ϕ_{qp} selfconsistently by variational techniques applied to $\langle\psi|\hat{H}-E|\psi\rangle$.

Since variation of $\langle\psi|\hat{H}-E|\psi\rangle$ both with respect to f as well as with respect to ϕ would lead to a coupled set of equations some additional, however very plausible, assumptions will be made.

First assumption: Since we want to restrict ourselves to adiabatic motion we make the following separation:

$$\phi_{qp} = e^{ip\hat{Q}}\,\phi_q \approx (1+ip\hat{Q})\phi_q \qquad \text{(T29)}$$

where $\hat{Q}$ is a hermitian and time-even 1p1h-operator which is further taken to be dependent on q and not on p because then the decoupling between collective and intrinsic motion can be easily formulated due to time-reversal properties.

Second assumption: We want the path ϕ_q to be the same for a full spectrum of f solutions because this corresponds to the usual picture of a well established collective motion.

Third assumption: The expectation value of $\langle\psi|\hat{H}-E|\psi\rangle$ is evaluated within the Gaussian Overlap Approximation (GOA).

Under these 3 assumptions, the variation of $\langle\psi|\hat{H}-E|\psi\rangle$ with respect to ϕ_{qp} leads to the ATDHF equations which destinate the "collective path" $\{\phi_q\}$ and the operator $\hat{Q}(q)$:

$$\langle\delta\phi_q|\hat{H} - \frac{\partial V}{\partial q}\hat{Q}(q)|\phi_q\rangle = 0 \tag{T30}$$

$$\langle\delta\phi_q|[\hat{H},\hat{Q}] + \frac{i\hbar}{M(q)}\hat{P}(q)|\phi_q\rangle = 0 \tag{T31}$$

with the hermitian and time-odd operator $\hat{P}$

$$\hat{P}(q)|\phi_q\rangle = (i\hbar\frac{\partial}{\partial q})_{ph}|\phi_q\rangle \tag{T32}$$

The classical potential V(q) and mass parameter are given by

$$V(q) = \langle\phi_q|\hat{H}|\phi_q\rangle \tag{T33}$$

$$\frac{\hbar^2}{M(q)} = \langle\phi_q|[\hat{Q}(q),[\hat{H},\hat{Q}(q)]]|\phi_q\rangle \tag{T34}$$

The operators $\hat{Q}$ and $\hat{P}$ which are the generators for the momentum p and coordinate q respectively have to be normalized as

$$\langle \phi_q | [\hat{Q}(q), \hat{P}(q)] | \phi_q \rangle = i\hbar \tag{T35}$$

The set of equations (T30) and (T31) can further be reduced to a single non-linear differential equation

$$\boxed{\frac{\partial}{\partial q}|\phi_q\rangle = c(q)[\hat{H}, \hat{H}_{ph}(q)]_{ph}(q)|\phi_q\rangle} \tag{T36}$$

$$\boxed{c(q) = \left(\frac{\partial V}{\partial q}\right)^{-1} \frac{M(q)}{\hbar^2}} \tag{T37}$$

The missing initial condition for eq. (T36) is obtained by requiring minimal coupling of the collective degree of freedom to the intrinsic ones. This degree of coupling is measured by a validity condition (Re78,Go81,Di86), however by experience we know that the path starting from the saddle point shows the desired minimal coupling.

Variation of $\langle \psi | \hat{H} - E | \psi \rangle$ with respect to f leads to the collective Schrödinger equation with the following collective Hamiltonian:

$$\boxed{H_c(q, i\hbar \frac{\partial}{\partial q}) = -\frac{1}{4}\left\{\frac{d^2}{dq^2}\frac{\hbar^2}{2M(q)} + \frac{d}{dq}\frac{\hbar^2}{M(q)}\frac{d}{dq} + \frac{\hbar^2}{2M(q)}\frac{d^2}{dq^2}\right\} + V(q) - (Z(q) - Z(q \to \infty))} \tag{T38}$$

with the same definition for the potential V and the mass parameter as for the ATDHF equations, see (T33) and (T34). The term Z(q) accounts for the quantum corrections which include the kinetic and potential zero-point energies along

the collective path and an approximate projection on angular momentum zero and translational momentum zero.

$$Z(q) = Z_{kin}(q) + Z_{pot}(q) + Z_{rot}(q) + Z_{trans}(q)$$

$$Z_{kin}(q) = \frac{\hbar^2}{2M(q)} \langle \phi_q | \frac{\overleftarrow{\partial}}{\partial q} \frac{\overrightarrow{\partial}}{\partial q} | \phi_q \rangle$$

$$Z_{pot}(q) = \frac{1}{2} \langle \phi_q | \hat{Q}^2(q) | \phi_q \rangle \frac{\partial^2 V}{\partial q^2} \qquad \text{(T39)}$$

$$Z_{rot}(q) = \sum_{i=1}^{3} \frac{\hbar^2}{2\theta_i(q)} \langle \phi_q | \hat{J}_{ph}^{(i)}(q)^2 | \phi_q \rangle$$

$$Z_{trans}(q) = \sum_{i=1}^{3} \frac{\hbar^2}{2mA} \langle \phi_q | \overleftarrow{\nabla}_{ph}^{(i)}(q) \overrightarrow{\nabla}_{ph}^{(i)}(q) | \phi_q \rangle$$

Although one should take the selfconsistent Thouless-Valatin rotational moment of inertia, we took so far the approximated Peierls-Yoccoz expression

$$\frac{\hbar^2}{\theta_i(q)} = \frac{\langle \phi_q | \{ \hat{J}_{ph}^{(i)}(q), \{ \hat{H}, \hat{J}_{ph}^{(i)}(q) \} \} | \phi_q \rangle}{4 \langle \phi_q | \hat{J}_{ph}^{(i)}(q)^2 | \phi_q \rangle} \qquad \text{(T40)}$$

R. Gissler however showed recently (Gi85) that this approximation is certainly not allowed in the internal interaction region, where there is a big increase in the deviation between the Peierls-Yoccoz and Thouless-Valatin approximations.

In practical calculations we also neglect the Z_{pot} term since the calculated potentials are quite smooth. An additional centrifugal term $\frac{\hbar^2}{2\theta_x} \ell(\ell+1)$ is added to V(q) to have a centrifugal barrier if one calculates the unprojected matrix elements $\langle \phi_q | \hat{H} | \phi_q \rangle$ in the case of axial symmetric wave functions ϕ_q without good ℓ quantum number.

A further interesting point is that a one parameter GCM with correlated states $|\phi_c(q)\rangle$ which contain weak 2p-2h excitations leads to the same equation of the collective path (T36). The correlations are of the RPA type (Re79):

$$\{\hat{P}(q) + i\,\lambda(q)\hat{Q}(q)\}|\phi_c(q)\rangle = 0$$

$$\lambda(q) = 2\langle\phi_c(q)|\hat{P}^2(q)|\phi_c(q)\rangle \qquad \text{(T41)}$$

so that one could in principle construct from the HF solution, which is always a solution of (T36), the RPA modes, and from these take the relevant one to extend to large amplitudes. The actual method of solution however is described in the next subsection.

3.2 Practical Method of Solution

The differential equation (T36) is solved by choosing a finite step $\delta q\; c(q) = -\varepsilon$ which yields

$$|\phi_{n+1}\rangle = \{1-\varepsilon[\hat{H},\hat{H}_{ph}(n)]_{ph}(n)\}|\phi_n\rangle \qquad \text{(T42)}$$

where n is the discrete path labelling which makes clear that the path itself $\{|\phi_q\rangle\}$ is completely independent of the measuring operator $\hat{O}$ which was chosen for the definition of q

$$\langle\phi_q|\hat{O}|\phi_q\rangle = q$$

Transforming the differential equation (T41) to the single-particle states $\{|\alpha,n\rangle \alpha=1...A\}$:

$$\boxed{|\alpha,n+1\rangle = |\alpha,n\rangle - \varepsilon(1-\rho_0(n))\{W_1(n)+W_0(n)(1-2\rho_0(n))W_0(n)\}|\alpha,n\rangle} \qquad (T43)$$

where the single particle density matrix is given by

$$\rho_0(n) = \sum_{\alpha=1}^{A} |\alpha,n\rangle\langle\alpha,n| \qquad (T44)$$

The Hartree-Fock Hamiltonian W_0 reads

$$W_0(n) = T + Tr\{\rho_0(n)v\} \qquad (T45)$$

with the effective two-body interaction v. The linear response operator $W_1(n)$ is defined through

$$W_1(n) = Tr\{v[W_0(n),\rho_0(n)]\} \qquad (T46)$$

In this dissertation all calculations for the construction of the collective path are performed using the BKN interaction (Bo76) and a recently fitted interaction with finite-range Yukawa-terms (Re84) denoted by MBKN from here onwards. With these interactions the Hartree-Fock Hamiltonian W_0 and the W_1 become

$$W_0(\bar{r},\bar{r}') = \delta(\bar{r}-\bar{r}')\left\{-\frac{\hbar^2}{2m}\nabla^2 + U(\bar{r})\right\} \qquad (T47)$$

$$W_1(\bar{r},\bar{r}') = 0$$

where

$$U(\bar{r}) = \frac{3}{4} t_0 \rho_0(\bar{r}) + \frac{1}{16} \rho_0(\bar{r})\rho_0^{\alpha}(\bar{r})$$

$$+ V_0 \int \rho_0(\bar{r}') \left[\exp\left\{ - \frac{|\bar{r}-\bar{r}'|}{a}\right\} / \frac{|\bar{r}-\bar{r}'|}{a}\right] d^3\bar{r}' \qquad \text{(T48)}$$

$$+ \frac{1}{4} e^2 \int [\rho_0(\bar{r}')/|\bar{r}-\bar{r}'|\,]d^3\bar{r}'$$

The formulae for W_0 and W_1 using Skyrme-type interactions can be found in (GG85,Gi85). The parameters are given in Table 1 where x has to be taken as $x = 3(1+\alpha)$.

	BKN	MBKN
α	1.0	0.25
t_0 (MeV fm^3)	-497.726	0.00
t_3 (MeV fm^x)	17270.0	14316.2
V_0 (MeV)	-363.043	-5998.66
a(fm)	0.4598	0.2786

Table 1: The parameters of the effective interactions used. See eq. (T48) for the meaning of the coefficients.

The parameters of the new interaction have been fitted to the binding energies of ^{16}O and ^{40}Ca and to the elastic electron scattering form factors. As one notices from the 1/4 e^2 in front of the Coulomb term in (T48) we use quartet symmetry such that protons and neutrons are treated on the same level with an effective charge of 1/2 e.

All calculations are performed in a grid box of dimension 16x16x32 fm^3 with a spacing of .8 or 1. fm in every direction. A grid box in momentum space is

also introduced. The reason for working in momentum space is twofold. First it allows one to cut away the unphysical Fourier components of the wave functions which correspond to energies higher than ~ 100 MeV, which also reduces noticeably the dimensions to be used in the momentum space grid. Secondly the action of the kinetic energy operator in W_o is reduced to a simple multiplication with k^2 of the wave functions in momentum space. The stability of the results concerning a change in E_{cut} = 100 MeV and a variation of the grid constant 1 fm has been illustrated in ref. (Go83). In accordance with E_{cut} = 100 MeV we chose ε somewhat smaller than $(100\ \text{MeV})^{-2}$. One starts solving eq. (T43) with a harmonic oscillator guess for the wave functions of the two nuclei separated by a certain distance. The wave functions ϕ_n outgoing from various starting separation distances all converge in the end to the one starting as close as possible to the saddle point. If they have merged into that optimal path the validity condition is best fulfilled; before merging this is not the case.

The asymmetry of some systems that are studied in this dissertation however causes a spurious centre-of-mass motion in the grid, in contrast to the symmetrical systems that were studied so far. We therefore remove from the ATDHF propagation differential equation the dipole component in the following way:

$$|\phi_{n+1}\rangle = \{1-\varepsilon[\hat{H},\hat{H}_{ph}(n)]_{ph}(n) - \frac{\langle \hat{D}_{ph}\phi_n|[\hat{H},\hat{H}_{ph}(n)]_{ph}(n)|\phi_n\rangle \hat{D}_{ph}}{\langle \hat{D}_{ph}\phi_n|\hat{D}_{ph}\phi_n\rangle}\}|\phi_n\rangle \qquad (T49)$$

where $\hat{D}_{ph}$ is the particle-hole part of the dipole moment operator. This achieves that the very small dipole moment of the initial configuration is kept constant, which ensures the centre-of-mass of the total system to be fixed. The multipole moments of the system which will be discussed later on are in the actual calculations all corrected for this small finite dipole moment.

The $\alpha + {}^{16}O \leftrightarrow {}^{20}Ne$ System

1. Introduction

The concept of clustering in nuclei was proposed quite early in nuclear physics (We37,Wh37,VW38) and due to its nice features it remained one of the more interesting topics in nuclear structure (CL84).

Concerning ^{20}Ne it was already pointed out in 1960 by Sheline and Wildermuth (Sh60) that an α-^{16}O cluster structure can result in a $2^+,4^+,6^+,8^+$ rotational band in ^{20}Ne. Davis suggested in 1963 (Da63) that the ground state band $K_\pi = 0^+$ and the first $K_\pi = 0^-$ band in ^{20}Ne should be regarded as arising from an α-^{16}O di-nucleus configuration. However it was not until the weak-coupling model of Arima (Ar67) that attention has been paid to the study of α-correlations in light nuclei. From then on, shell-model calculations with higher-shell mixing, GCM clustering calculations, resonating group and orthogonality condition model calculations were used to study the different structures of the several bands in ^{20}Ne and the heavy ion $\alpha+^{16}O \leftrightarrow {}^{20}Ne$ reaction mechanism together with the other possible higher-lying structures according to the Ikeda diagram (Ik68,Ho68,Ik72,Fu80,Sa79,Hi83).

A disadvantage of those calculations, however, is the fact that these models all rely on certain assumptions regarding the single-particle wave functions used. Usually they are evaluated by means of the α-cluster model, harmonic oscillators for the fragments, mostly even with identical oscillator parameters, constrained Hartree-Fock with a given constraining operator, etc.

It is, however, not very clear how all these assumptions can be justified. Hence it is important to investigate the $\alpha+^{16}O \leftrightarrow {}^{20}Ne$ system by means of a microscopic approach which is free of adjustable parameters and is solely based on variational principles, such as the quantized ATDHF-theory.

We therefore want to apply the quantized ATDHF theory for a microscopic description of the clustering structure of ^{20}Ne and to the low-energy α-^{16}O heavy ion reaction.

2. Static Properties of the α, ^{16}O and ^{20}Ne Systems

If starting from a distance between the clusters, where the attractive nucleon-nucleon force is prevailing over the Coulomb repulsion, successive solution of (T42) finally converges to the HF ground state of the ^{20}Ne system. The final state one obtains depends only on the symmetries of the chosen initial starting configurations; in this case one reaches in the end the corresponding ^{20}Ne "ground state" configuration. Some relevant values for the nuclei under consideration are summarized in Table 1 and are compared with the experimental values. It turns out that it is impossible to describe equally well the binding energy for the α-particle and the ^{16}O system together with that of the ^{20}Ne compound nucleus with the present type of interactions. This will eventually cause low-lying rotational states in the spectrum of the ^{20}Ne ground state band to be unbound. The new interaction, however, will turn out to be a little more appropriate than the BKN force.

		exp.	MBKN	BKN
^{4}He:	E_{HF} (MeV)	-28.30	-17.51	-16.98
	E_{HF}^{ZPE} (MeV)	-28.30	-28.36	-29.16
^{16}O:	E_{HF} (MeV)	-127.62	-124.13	-116.40
	E_{HF}^{ZPE} (MeV)	-127.62	-132.14	-127.04
^{20}Ne:	$\langle r^2\rangle^{1/2}_{proton}$ (fm)	2.91	2.97	2.96
	$\sqrt{\frac{16\pi}{5}}\langle r^2 Y_{20}\rangle_{proton}$ (fm^2)	56.4±2.7	51.97	53.04
	E_{HF} (MeV)	-160.65	-151.55	-140.64
	E_{HF}^{ZPE} (MeV)	-160.65	-164.48	-154.78
	$E_{HF}^{(\pm)}$ (MeV)	-160.65	-152.31	-141.87
	$\Delta E^{(-)}$ (MeV)	5.78	5.44	4.68

Table 1: HF results of the ^{4}He, ^{16}O and ^{20}Ne systems for the two different interactions used in comparison with the experimental values. E_{HF} and E_{HF}^{ZPE} are the total binding energies without and with correction terms for the zero-point translational and rotational motions. $E_{HF}^{(\pm)}$ stands for the binding energy obtained in a calculation where the variation is performed after the projection on positive parity (VAP). $\Delta E^{(-)}$ gives the energy difference between the VAP on positive parity and a VAP on negative parity calculation. The proton rms radius is denoted by $\langle r^2\rangle^{1/2}_{proton}$ whereas the intrinsic proton quadrupole moment is given by $\sqrt{\frac{16\pi}{5}}\langle r^2 Y_{20}\rangle$. For both quantities point particles are assumed.

One can read from the table that the zero-point energy corrections increase the binding energy of ^{20}Ne by 13 MeV, from which 9.5 MeV are due to translational and 3.5 MeV due to rotational spurious motion of the total ^{20}Ne system. These are the numbers for the new interaction, those for the BKN force are 14 MeV, 10 MeV and 4 MeV respectively.

The pure HF ground state of ^{20}Ne, as coming out from the calculations, is reflection symmetric with respect to the plane orthogonal to its symmetry axis. This does not mean however that this ground state cannot be improved by admixing nonsymmetric configurations.

Since in reality the ^{20}Ne ground state has a good parity we have to perform a projection on good parity and vary with respect to the asymmetry degree of freedom after the projection.

We therefore construct the projected states following

$$|\phi_n^{\pm}\rangle = N\{|\phi_n\rangle \pm \hat{P}_z|\phi_n\rangle\} \qquad (N1)$$

where N is a normalisation constant and $\hat{P}_z$ an operator which transforms in the wave functions ϕ_n the $z \to -z$. The energy curves $V_n = \langle\phi_n^{\pm}|\hat{H}|\phi_n^{\pm}\rangle$ are shown in Fig. 1. The part to the right of the saddle point is constructed by starting

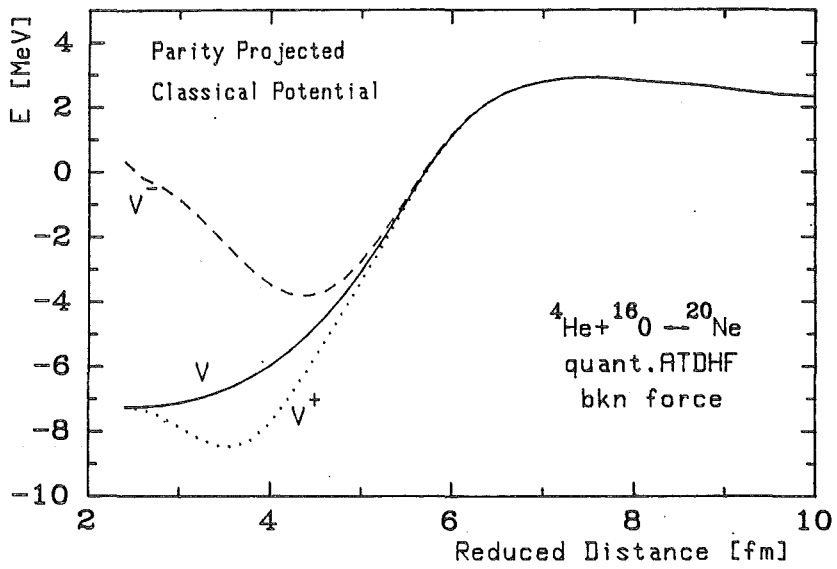

Fig. 1: Classical potential V and energy curves for the wave functions with positive parity V^+ and negative parity V^- as a function of the reduced distance. The BKN interaction is used.

at a cluster distance where the repulsive Coulomb force prevails over the attractive nuclear force. In this figure the states $|\phi_n\rangle$ are labelled by the so-called reduced distance, whose definition will be given later on. For separated fragments it coincides with the cluster distance, i.e. the distance between the centres of mass of the fragments.

Using the BKN interaction the symmetric ^{20}Ne HF ground state is reached at a reduced distance of 2.48 fm. Because of its symmetry it is also lying on the V^+ curve, however not at its minimum. This one lies at a reduced distance of 3.55 fm and is by 1.2 MeV more bound than the simple HF state. The search for the minima of the V^+ and V^- curves corresponds to an approximate variation after parity projection. Besides the gain of binding energy one also obtains a measure for the excitation energy of the head of the negative-parity band. This number is extracted from the energy difference between the minima of the V^+ and V^- curves and is given together with the experimental values in Table 1. A good agreement is achieved. As we have seen at the unprojected HF solution the zero-point energies due to translation and rotation are very important and result in about 14 MeV to be compared to the 1.2 MeV for parity projection. Thus the correct procedure would be to evaluate zero-point energy corrections for the parity-projected energy curves. Since, however, the rotational zero-point energy correction term has already in it some parity-projection properties we did not investigate this subject further because in one of the next sections we will introduce a full angular momentum projection. Nevertheless, it is clear that a proper description of the ^{20}Ne ground state system should also include the asymmetry degree of freedom of the α-^{16}O configuration.

3. The Collective Path α-^{16}O

The collective path is, in our case, the family of intrinsic Slater determinants leading from the separated fragments in a continuous way to the compound ^{20}Ne nuclear system. In Fig. 2 we show the single-particle wave functions

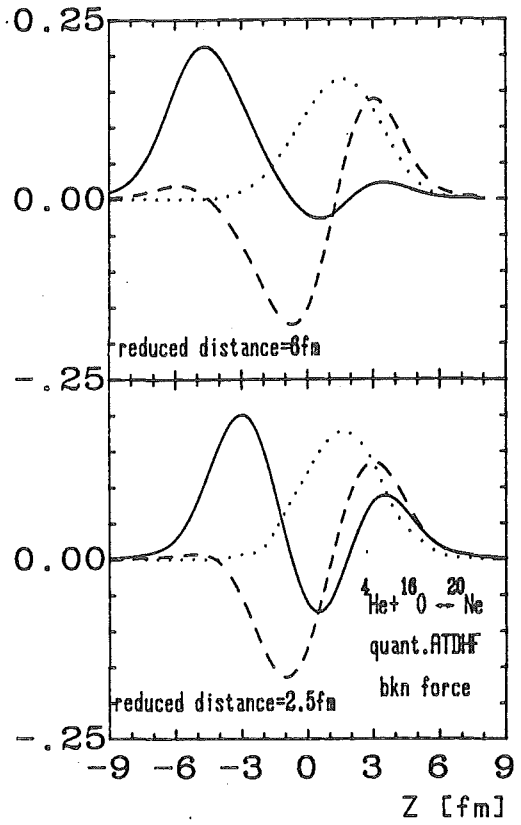

Fig. 2: Orthonormalized single particle wave functions along the axis of collision for two different configurations. The reduced distance 2.5 fm corresponds to the HF point of ^{20}Ne. Considered are the ($n_x = 0$, $n_y = 0$, $n_z = 0$) wave function of the α-fragment (solid line), the (0,0,0) wave function of the ^{16}O fragment (dotted line) and the (0,0,1) wave function of the ^{16}O fragment (dashed line). The quantum numbers correspond to the asymptotic region.

along the z-axis for two different configurations. In the first configuration at a reduced distance of 6 fm the α-particle overlaps only slightly with the ^{16}O so that we still recognize the asymptotic wave functions: the α s-wave

function on the left side and the ^{16}O s and p_z wave functions centered on the right side. The second configuration at a reduced distance of 2.5 fm is close to the HF state of ^{20}Ne and one can see how the original α s-wave is deformed. Although there is an arbitrariness in plotting these wave functions, since we are free to perform a unitary transformation among the occupied states, nevertheless these pictures reveal qualitatively the structural changes along the collective path. Three-dimensional plots of the particle densities in the (x,z) plane along the path are shown in Fig. 3. In the first picture the α-particle is separated from the ^{16}O cluster whereas in the next pictures the α-particle starts to overlap more and more with the ^{16}O until finally they both completely loose their own identity to form a symmetric ^{20}Ne HF ground state.

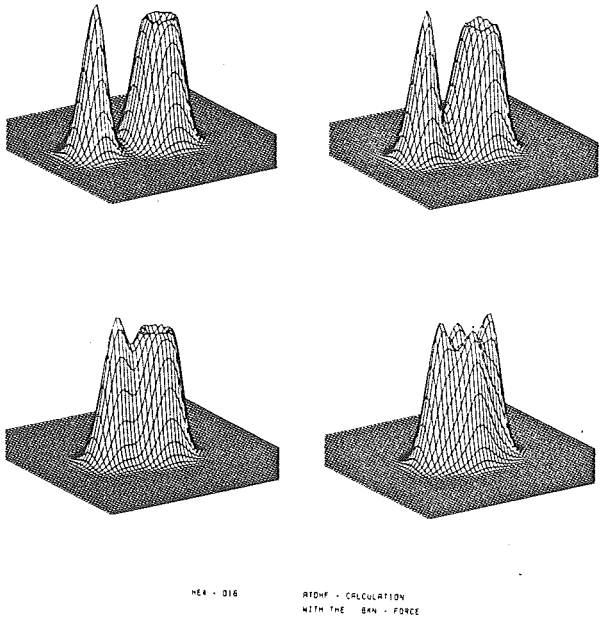

Fig. 3: Particle densities $\rho(x,y=0,z)$ at different cluster distances along the path; i.e. at a reduced distance of 7.4, 6.0, 4.4 and 2.5 fm respectively.

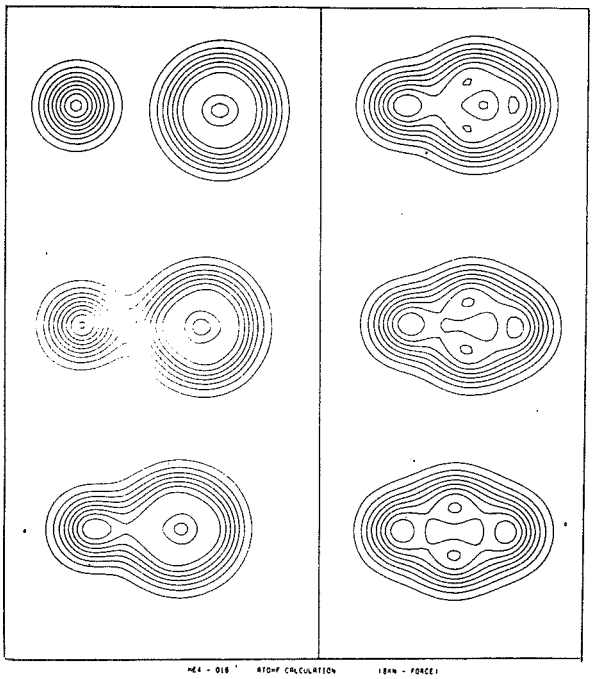

Fig. 4: Lines of equal density $\rho(x,y=0,z)$ at different cluster distances along the path; i.e. at a reduced distance of 7.4, 6.0, 4.2, 3.5, 3.1, 2.5 fm respectively.

Two-dimensional plots of the densities along the path are shown in addition in Fig. 4 because they will clarify some important remarks made in the next section. The middle of the ^{16}O in all these plots should be considered as a local minimum.

4. The Collective Coordinates

In order to extract a Schrödinger equation for the collective α-^{16}O relative motion it is convenient to label the determinants ϕ_n by a collective coordinate $q_n = \langle\phi_n|\hat{O}|\phi_n\rangle$ where $\hat{O}$ is a properly chosen measuring operator. A reasonable labelling of the path will be a coordinate which is equal to the distance between the clusters as long as both nuclei have a negligible overlap. This has also the advantage that the mass parameter becomes equal to the reduced mass in the asymptotic region where the main degree of freedom is the cluster distance. Of course, the physical information is contained fully in the set $\{|\phi_n\rangle\}$ and the labelling is only a matter of making the dynamics more illustrative. This important feature, which is necessary for a suitable collective theory but nevertheless often forgotten, will be explicitly demonstrated in this section.

Three different choices of such a "distance" have been made for this system:

(i) Quadrupole distance.

Two particles with quadrupole deformations $Q_2(1)$ and $Q_2(2)$ at a distance R from each other give the following quadrupole moment for the total system:

$$Q_2 = 2\,\mu\,R^2 + Q_2(1) + Q_2(2) \qquad \text{(N2)}$$

where μ is the reduced mass. This holds under the assumption that the centre of mass is at the origin. Hence we define in analogy the so-called quadrupole distance for the α-^{16}O system

$$R_2 = \sqrt{\left(\frac{16\pi}{5}\right)^{1/2} \frac{\langle\phi_n|r^2 Y_{20}|\phi_n\rangle}{2\mu}} \qquad \text{(N3)}$$

where $(\frac{16\pi}{5})^{1/2}\langle\phi_n|r^2Y_{20}|\phi_n\rangle$ is the total quadrupole moment of the $\alpha+^{16}O$ system along the collective path. The α-particle and the ^{16}O nucleus have no static deformation. Thus in the asymptotic region this R_2 agrees with the actual cluster distance. Since the calculated ^{20}Ne HF ground state has a quadrupole deformation the corresponding minimal value of the R_2 coordinate is 4.07 fm. For the BKN force the classical potential V and mass parameter M as functions of this R_2 coordinate are given in Fig. 5. The divergency of the

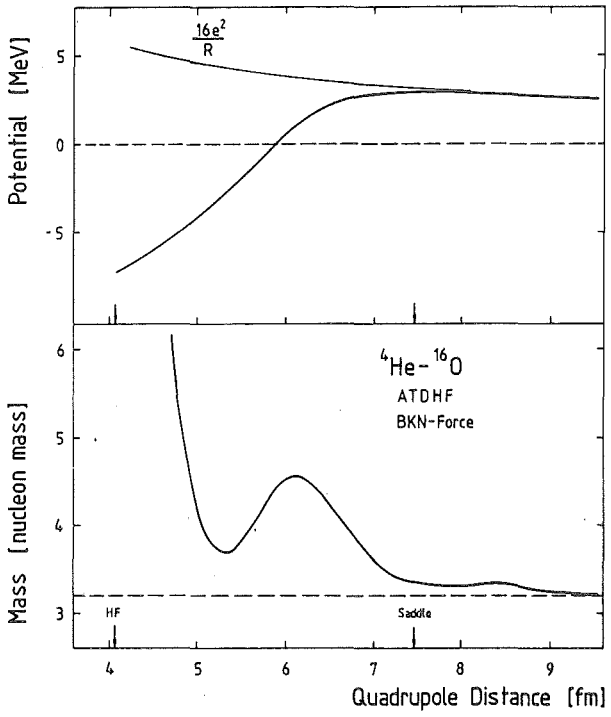

Fig. 5: Collective mass M and classical potential V as a function of the quadrupole distance. The calculations are done with the BKN-force.

mass in coming closer to the HF minimum is explained by the fact that the quadrupole moments of the three stages of the collision on the r.h.s. of Fig. 4 are more or less constant although there are noticeable changes in the mass distribution. The mass parameter is a measure of the amount of internal rearrangements of the wave functions for a given change of the collective coordinate chosen. Hence in the present case it is bound to diverge.

This feature tells us that in this region another coordinate might be more appropriate to label the different Slater determinants. So we looked for higher moments which still change near the HF point. Fig. 4 shows us that the octupole moment which goes to zero approaching the ^{20}Ne ground state seems to be an appropriate choice as well. So we define a new coordinate called the octupole distance.

(ii) Octupole distance.

The octupole moment for a two particle system with the centre of mass in the origin and for separate particles with quadrupole and octupole moments $Q_2(1)$, $Q_2(2)$, $Q_3(1)$, $Q_3(2)$ is given by

$$Q_3 = -2\mu \frac{A_2-A_1}{A_2+A_1} R^3 + \frac{3R}{A_1+A_2} (-A_2 Q_2(1)+A_1 Q_2(2)) + Q_3(1) + Q_3(2) \qquad (N4)$$

where R is the cluster distance, A_1 and A_2 the masses of the two separate particles and μ the reduced mass of the system. Hence we define in analogy the so-called octupole distance for the α-^{16}O system

$$R_3 = \sqrt[3]{\frac{A_1+A_2}{2\mu(A_2-A_1)} \left(\frac{16\pi}{7}\right)^{1/2} \langle \phi_n | r^3 Y_{30} | \phi_n \rangle} \qquad (N5)$$

which is in the asymptotic region again equal to the cluster distance. For the BKN-force the potential and mass parameter as functions of R_3 are shown in Fig. 6. One sees now that the region near the HF point gets expanded so that the potential shows a flat minimum. Whereas the potential is only influenced by a rescaling the divergency of the mass in R_2 is now overcome and the mass parameter goes now even to zero in approaching the HF point. A comparison between the two choices R_2 and R_3 is made in Fig. 7 which clearly illustrates the suitability of the R_3 coordinate near the HF point.

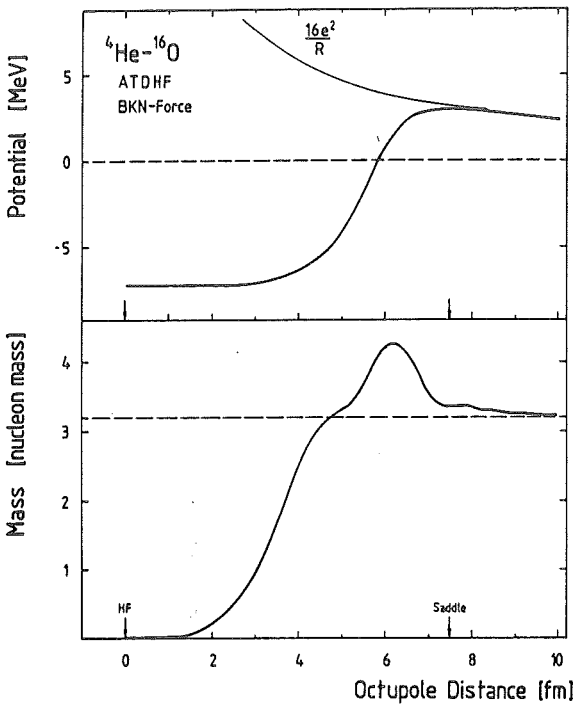

Fig. 6: Collective mass M and classical potential V as a function of the octupole distance. The BKN-force is used.

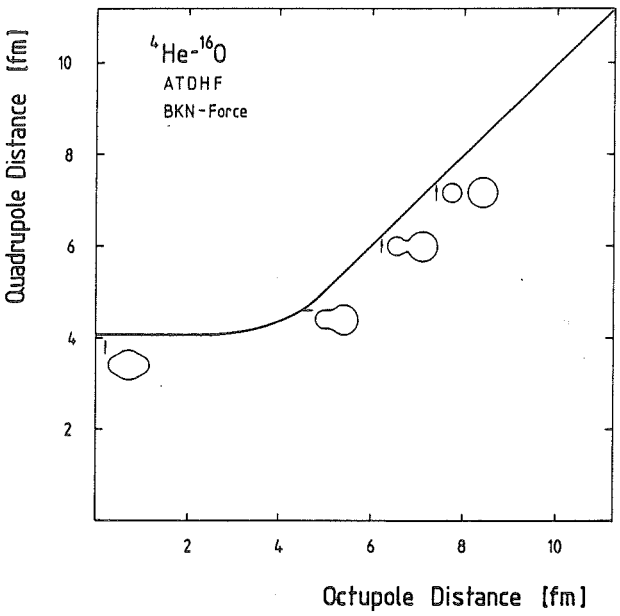

Fig. 7: Quadrupole distance as a function of the octupole distance.

(iii) Reduced distance.

As was already pointed out in the beginning of this section, the physical information contained in the quantities V, M and Z is identical no matter which coordinate is actually used. To illustrate this, we perform from R_2 as well as from R_3 a transformation to a new coordinate called the reduced distance R_{red} in which the mass parameter is constant. This is e.g. achieved by the following coordinate transformation:

$$dR_{red} = dR_3 \sqrt{\frac{M(R_3)}{\mu}} \qquad (N6)$$

which is integrated inwards from the asymptotic R_3 region. Since $M(R_3) = \mu$ at large distance, the reduced distance is equal to the cluster distance in the

asymptotic region. The fact that in this coordinate the mass parameter is constant and equal to the reduced mass can easily be shown using eqs. (T32), (T34) and (T35). The transformation (N6) has also been performed outgoing from the quadrupole distance R_2 obtaining identical results. The divergency of the $M(R_2)$ mass causes some technical complications which, however, can be solved. This reduced distance has besides a mere convenience also a clear advantage.

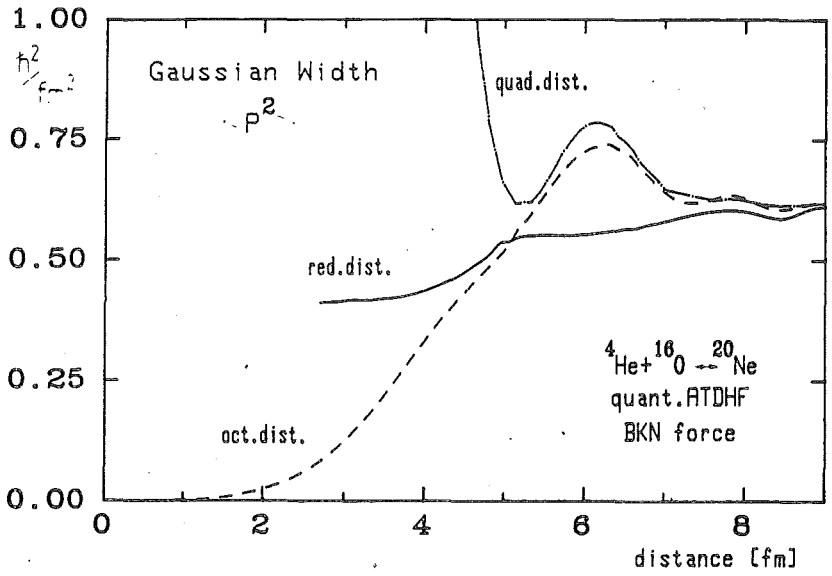

Fig. 8: Gaussian width $\langle \phi_n | \hat{P}^2 | \phi_n \rangle$ for the three different coordinates used: quadrupole, octupole and reduced distance.

As one can see at Fig. 8 the width

$$\lambda(q) = 2\langle \phi(q) | \hat{P}^2(q) | \phi(q) \rangle$$

shows only for the reduced distance a rather small variation. This indicates that the Gaussian Overlap Approximation (GOA), necessary for the derivation of the collective Schrödinger equation (T38) from the GCM, is well fulfilled (Re76) for the reduced coordinate distance in contrast to the cases where the

coordinates R_2 and R_3 are used. Actually the $\lambda(q)$ is closely connected with the mass parameter $M(q)$, as shown in eqs. (4.3) and (4.4) of Ref. (Go83). Thus the steep rise of $\lambda(R_2)$, seen in Fig. 8, shows that the divergence of $M(R_2)$ is not caused by any sort of level crossing but only by the inappropriate choice of the label R_2. In fact, the present ATDHF-formalism does not contain the possibility for level crossings at all since within the symmetries, set by the initial conditions near the saddle point, the single particle wave functions are free to perform any possible variation. And, as mentioned already, however the mass looks like in a given coordinate, one can always perform a transformation to the reduced coordinate with a constant mass parameter and nearly constant width parameter $\lambda(q)$.

5. Solution of the Schrödinger Equation for Bound States and Resonances

The potential V and the quantum-corrected V-Z which enters into the collective Hamiltonian, are shown in absolute values as a function of the reduced distance in Fig. 9. The different contributions to the zero-point energy Z are shown in Fig. 10.

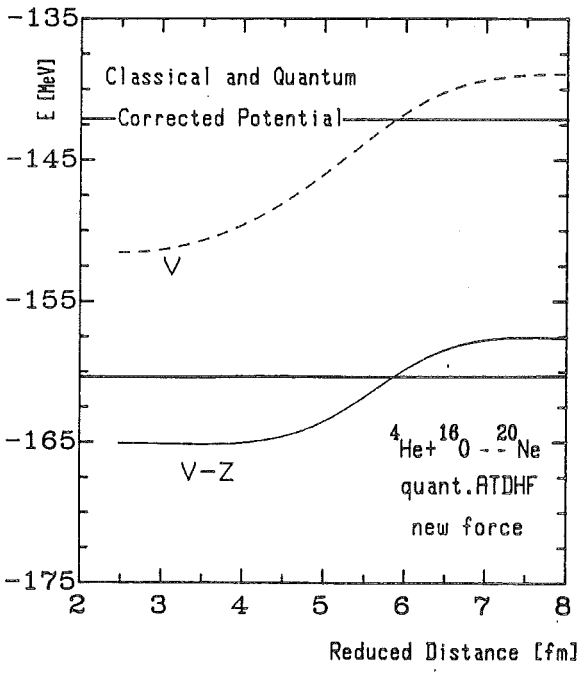

Fig. 9: The classical potential V and quantum corrected potential V-Z plotted in absolute values. The corresponding asymptotic binding energy is indicated by a straight line. The barrier height and potential minimum are respectively 2.72 and 9.91 MeV for the V potential and 2.94 and 4.65 MeV for the V-Z potential. The new force of Ref. (Re84) is used.

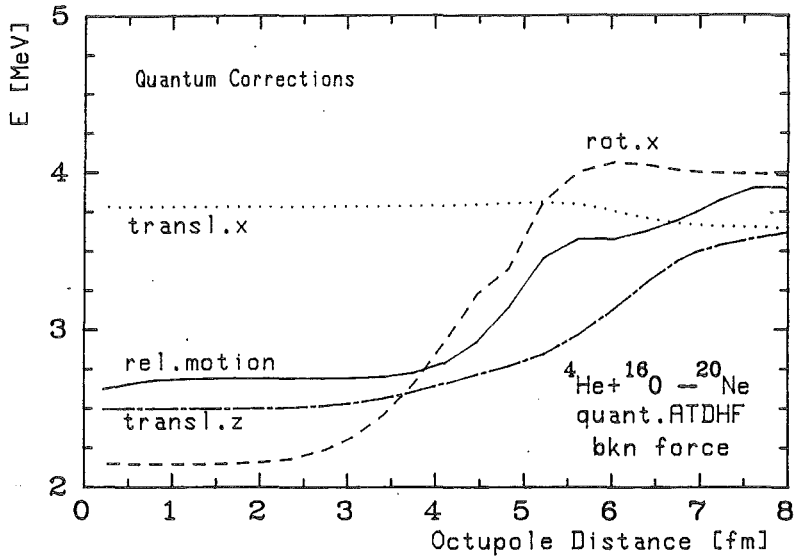

Fig. 10: The quantum corrections for relative motion, rotation around the x-axis (to be counted twice), for translation along the x-axis (to be counted twice) and for translation along the z-axis, i.e. the collision axis.

In order to allow for rotations of the total system we include the centrifugal term to our collective Hamiltonian (T38), which reduces, using the reduced distance, to

$$H_C^L(q, i\hbar \frac{\partial}{\partial q}) = -\frac{\hbar^2}{2\mu}\frac{d^2}{dq^2} + V(q) + \frac{\hbar^2}{2\theta(q)} L(L+1) - Z(q) \qquad (N7)$$

This is then solved for bound states following the method of Vautherin and Brink (Va72), and for scattering states following the procedure of Smith (Sm69).

To extract the "bound states" we took the calculated potentials up to the saddle point and assumed the extension of this barrier height to $r \to \infty$. The results for the two interactions are summarized in Table 2. The resonance energies (in brackets in the table) are the positions of the phase shifts going through $\pi/2$. The even partial waves were calculated in the V^+-Z potential and the odd

ones in the V^--Z potential. With the BKN interaction no bound states are obtained due to the small depth of the V-Z potential, whose minimum is only 2.27 MeV below the asymptotic binding energies of α and ^{16}O, whereas the experimental 0^+ ground state of ^{20}Ne is bound by 4.73 MeV. The new interaction yields a 0^+ bound state at -1.27 MeV which, however, is still not bound enough.

BKN				MBKN				exp.	
ℓ	E	ℓ	E	ℓ	E	ℓ	E	ℓ	E
0	.34 (.34)			0	-1.27			0	-4.73
		1	2.46 (2.40)			1	1.33 (1.32)	1	1.06
2	1.65 (1.63)			2	-0.06			2	-3.10
		3	4.28 (4.33)			3	3.21 (3.14)	3	2.43
4	4.49 (4.43)			4	2.75 (2.73)			4	-.48
		5	(8.19)			5	6.43 (6.57)	5	5.53
6	8.78 (8.98)			6	7.09 (7.05)			6	4.05
		7	(14.18)			7	(11.88)	7	10.61
8	(15.49)			8	12.77 (13.07)			8	7.22
		9	(22.00)			9	(19.10)		
10	(23.89)			10	(20.90)				

Table 2: "Bound state" energies and energies of the scattering resonances (in brackets) in MeV, solving the Schrödinger equation for the BKN and new interaction (MBKN) in the V^+-Z for the even and in V^--Z for odd partial waves. The energies are given with respect to the asymptotic $\alpha+^{16}O$ binding energies.

Similarly in Ref. (Ma83) where also the BKN force was used within a constrained Hartree-Fock model they obtain the ground state of the generator coordinate calculation only 0.6 MeV below threshold. Their hope to get an energy gain of 4-5 MeV resulting from a projection on the 0^+ state is in vain since our present zero-point energy Z contains in the Gaussian overlap approximation the correlation energy due to angular momentum projection.

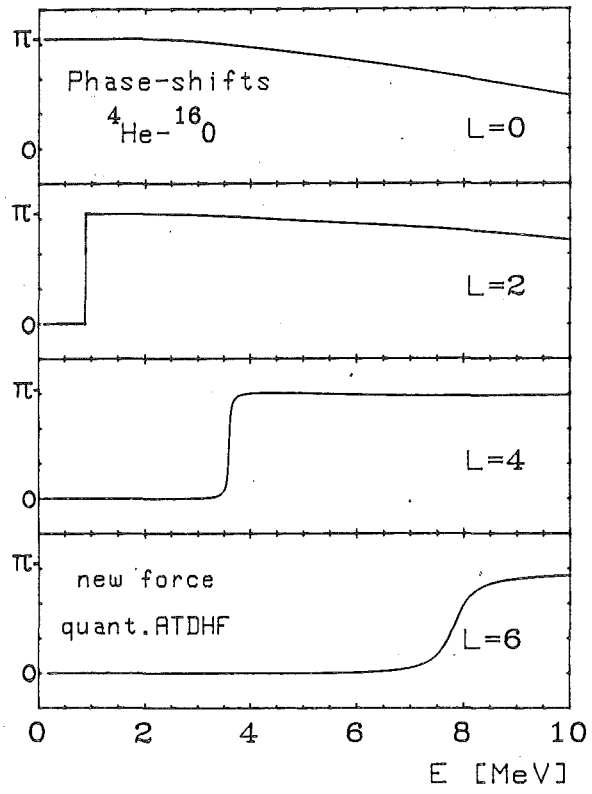

Fig. 11: Phase shifts for the ℓ = 0,2,4 and 6 α-^{16}O scattering. The new force of Ref. Re84 is used.

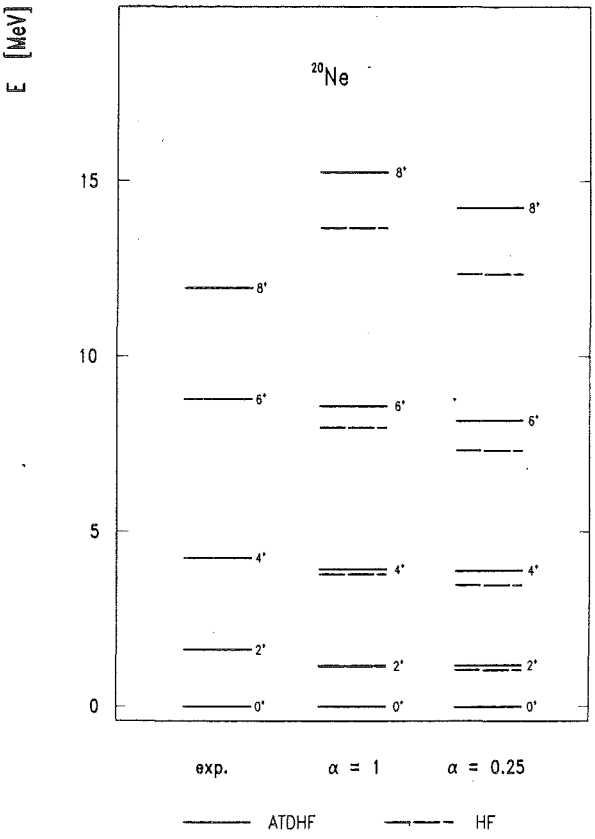

Fig. 12: Ground state rotational band of ^{20}Ne. Experimental levels, quantized ATDHF levels calculated with the BKN force (α=1.0) and with the new force (α=0.25) are compared. The results obtained with ^{20}Ne HF ground state plus adding a centrifugal term are also given.

An example of phase shifts is presented in Fig. 11, and in Fig. 12 we compare the positions relative to the 0^+ with the experimental (Aj83) ^{20}Ne ground state band. The excitation energies of the $2^+,4^+,6^+$ states are in good agree-

ment with experiment. The 8^+ however is known to have no longer a rotational structure. So we cannot expect to find agreement with experiment since we describe the rotational properties by a simple centrifugal term proportional to L(L+1). As a comparison the rotational spectra obtained by using solely the moment of inertia of the ^{20}Ne HF ground state are also given. The similarity of this spectrum to the ATDHF one is however cheating. Indeed the "correct" angular momentum projection of the ^{20}Ne HF intrinsic state, as shown in Fig. 2 of the Appendix A1, shows a much more compressed spectrum over a factor .6 in comparison to its Peierls-Yoccoz approximation.

The similarity between the HF and ATDHF spectrum, however, shows that the ground state band is indeed very close to the (8,0) classification of SU(3). The 1^- band head of the inversion doublet lies at 2.06 MeV for BKN and 2.59 MeV for MBKN above the 0^+ state which is in both cases too low in comparison to the experimental 5.78 MeV value.

This shows that the dissolution of the α into the ^{16}O goes not easy enough with the BKN force since, if both particles are not polarizable, one would obtain the spectrum of a rigid rotator with a negative parity band fitting into the positive parity band without energy shift. Therefore the greater this energy shift the higher the polarizability (Ik68).

A further remark concerns the fact that since ^{20}Ne is deformed in its intrinsic HF ground state, the moment of inertia is finite for the minimum value of the coordinate label. This makes all partial waves to start as s-waves since one does not have the usual $\frac{\ell(\ell+1)}{r^2}$ behaviour.

Another pecularity enters because the coordinate does not start from zero such that automatically a hard core enters into the calculation. This is contrary

to the usual two centre shell models where they impose artificially a r=0 choice. On the other hand, the authors Tanabe and Nemoto (Ta74) report in a GCM calculation with Volkov 2 force that "the α-^{16}O interaction has a feature as if it had an effective repulsive core with the radius of ~ 3 fm for L≤8" because the wave functions have an outermost nodal point of inner oscillation of about 3 fm.

Since it seemed for numerical reasons not possible to calculate form factors for even partial waves in V^+ and to add these with the form factors for odd partial waves in V^- at small angles, we calculated cross sections only in V-Z.

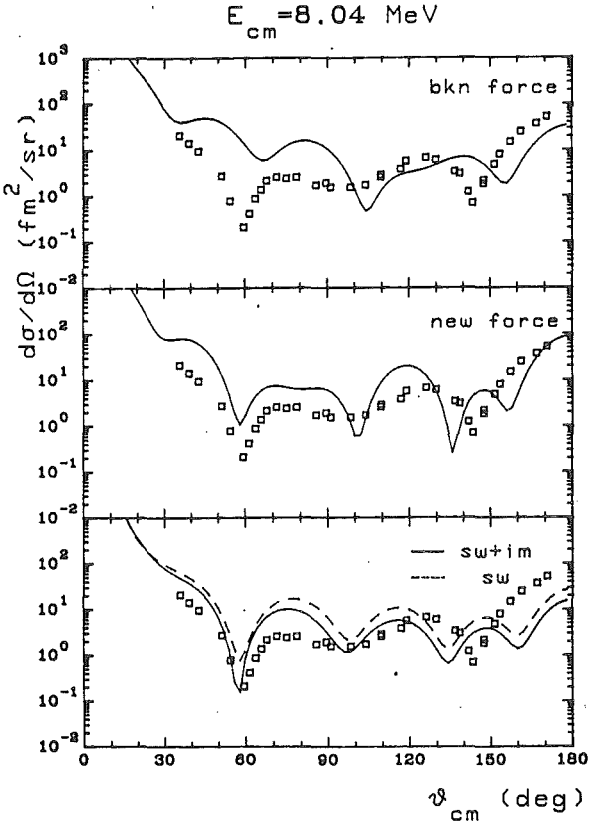

Fig. 13: Differential scattering cross sections for the elastic scattering of α on ^{16}O for a CM bombarding energy of 8.04 MeV. The experimental data, indicated by the open squares, are taken from (Me67) and compared with the BKN and new interaction calculations and with a Woods-Saxon fit (Me67) to the experimental data once with and once without the imaginary part.

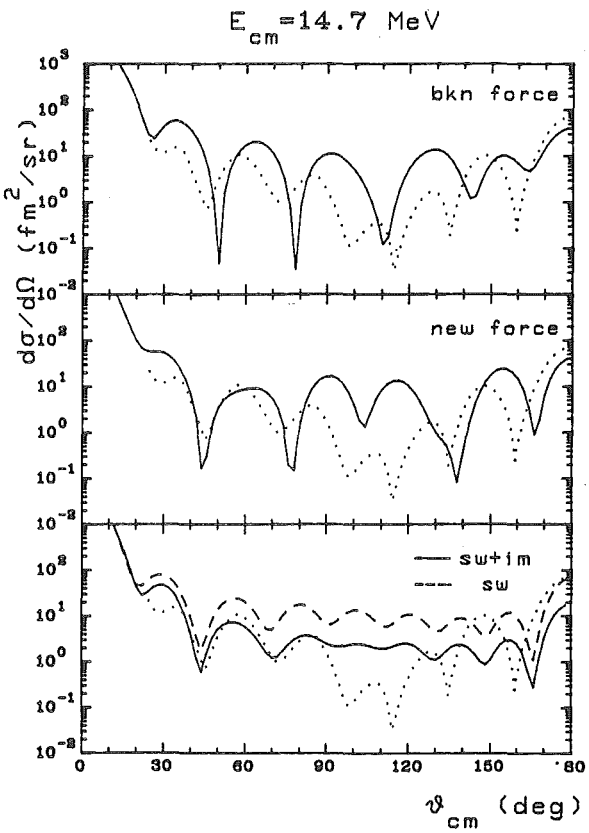

Fig. 14: Differential scattering cross sections for the elastic scattering of α on ^{16}O for a CM bombarding energy of 14.7 MeV. The experimental data, indicated by a dotted line, are taken from (Co59) and compared with the BKN and new interaction calculations and with a Woods-Saxon fit (Me67) to the experimental data once with and once without the imaginary part.

In Figs. 13 and 14 the elastic differential scattering cross sections are plotted for a CM bombarding energy of 8.04 and 14.7 MeV respectively. The two upper pictures show the comparison between experiment and the calculations done with the BKN and new interaction. The lower picture compares experiment with the Woods-Saxon fit to the experimental data. It turns out that the quantized ATDHF values with the new force are qualitatively as good as the fitted Woods-Saxon cross sections. At E_{CM} = 14.7 MeV there is around $\theta = 100^{o}$ a region which is poorly described by all models. Besides this the ATDHF cross sections agree in numbers and positions of the minima and maxima well with experiment. These examples demonstrate that, particularly at low energies, the quantized ATDHF theory is a suitable tool to describe elastic HI collision processes. It remains for the future to generalize the formalism to channel couplings.

6. GCM Structure calculations

GCM and the more restricted Resonating Group Method calculations (La74,Ma75, Mi76,He76,Fi76) lead to satisfactory results for the description of the ^{20}Ne system. We however want to study also the dependence of the results on the choice of the generating functions of the GCM. So far mainly two-centre harmonic oscillator wave functions or wave functions of Brink's α-cluster model have been chosen. In these models an r-dependent oscillator width b leads to wave functions which are contaminated by spurious centre-of-mass excitations. Although we therefore could expect in principle the same for our wave functions we omitted this additional time consuming projection. We hope nevertheless that the effects will be minimal. The wave functions we use are projected on good angular momentum following the method which is outlined in the Appendix A1. As a consequence we restrict ourselves to the BKN force in the following since the new interaction is not rotationally invariant.

i) qATDHF

The correct qATDHF procedure would be to do a one parameter GCM with the correlated states $\phi_c(q)$ described by (T41). As a first approximation, however, we took the uncorrelated wave functions. The diagonal kernels H_ℓ/N_ℓ are presented in Fig. 15. We took 11 points with an interdistance of 1 fm in the octupole coordinate. A cut-off radius of 7 fm was taken and an accuracy parameter δ for eliminating the linear dependent rows of the order $\delta = 10^{-4}$ gave consistent results. Consistent results in the sense that the 2 (equivalent) procedures "diagonalization before elimination" and "elimination before diagonalization" give the same answer. The results are presented in Table 3.

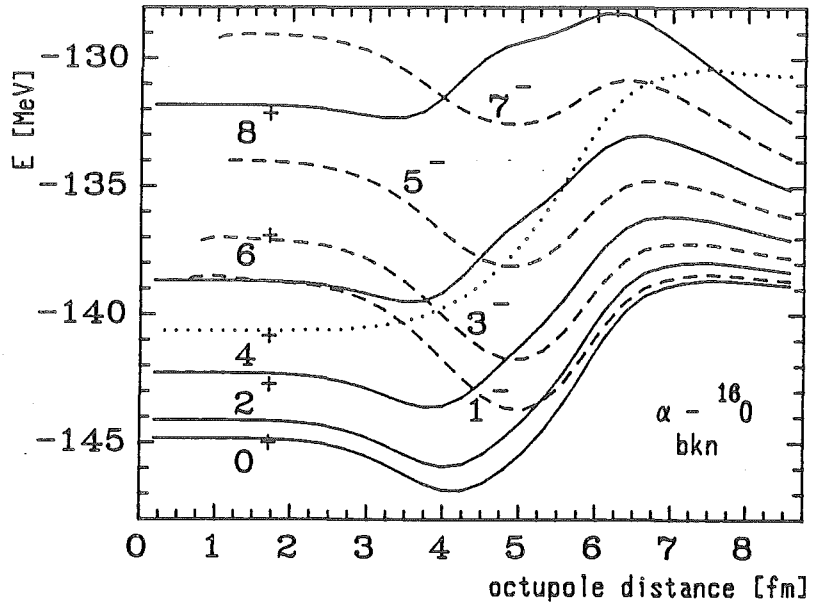

Fig. 15: Projected diagonal matrix elements $\langle \phi_\ell | \hat{H} | \phi_\ell \rangle / \langle \phi_\ell | \phi_\ell \rangle$. The dotted curve represents the unprojected values.

ℓ	0	1	2	3	4	5	6	7	8
	-2.07	1.09	-.90	2.92	1.52	6.30	5.91	11.24	13.29
	5.20	7.96	6.24	9.31	8.10	11.82	11.34	15.72	16.60
	11.00	16.26	12.06	17.56	13.86	20.01	17.13	23.91	23.28
	21.10	26.14	22.03	27.34	23.99	29.66	27.34	33.32	32.95
	29.73	33.77	30.46	35.15	32.32	38.15	35.63	43.58	40.56

Table 3: GCM bound state energies in MeV with respect to the α-^{16}O threshold energy using the qATDHF wave functions.

ℓ	0	1	2	3	4	5	6	7	8
	2.73	4.10	3.74	5.83	6.06	8.91	9.78	13.22	15.41
	7.82	9.40	8.53	10.79	10.14	13.38	12.81	17.55	18.11
	15.85	19.14	16.48	20.38	17.71	22.62	19.70	26.20	24.22
	26.26	32.99	26.60	33.77	27.90	35.25	29.97	37.67	34.93
	40.98	47.27	41.46	47.70	39.23	49.23	37.37	52.10	50.15

Table 4: GCM bound state energies in MeV with respect to the α-^{16}O threshold energy using the HF sudden approximation.

ii) HF sudden approximation

Just as in the 2 centre harmonic oscillator model one can use the HF wave functions of the separate nuclei, locate the single particle wave functions at several separation distances and antisymmetrize the total system. In Fig. 16 we compare the $\langle\phi_0|\hat{H}\phi_0\rangle/\langle\phi_0|\phi_0\rangle$ for the ATDHF and the HF sudden case. The other ℓ-values are similar. The GCM bound states are summarized in Table 4.

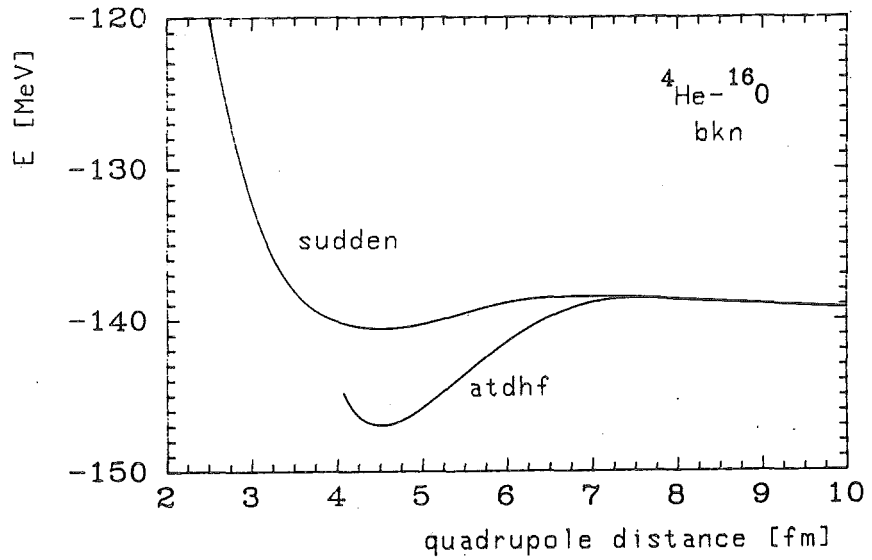

Fig. 16: Comparison of $\langle\phi_0(q)|\hat{H}|\phi_0(q)\rangle/\langle\phi_0(q)|\phi_0(q)\rangle$ for the ATDHF wave functions and the HF-sudden approximation.

From Fig. 16 and comparison between Table 3 and Table 4 one learns that there is certainly a difference between the two different set of generating functions, at least using the BKN force.

Comparison of Table 2 and Table 3 shows an energy gain for the ^{20}Ne 0^+ ground state of 2.41 MeV for the GCM calculation with respect to the solution of the Schrödinger equation. One should however remark that we corrected approximately for the CM-motion in the Schrödinger case whereas for the GCM calculation

no additional projection on translational momentum zero has been performed. According to the behaviour of the translational zero point corrections in Fig. 10 one expects that the ^{20}Ne system would become less bound with respect to the α-^{16}O threshold if one includes a CM projection.

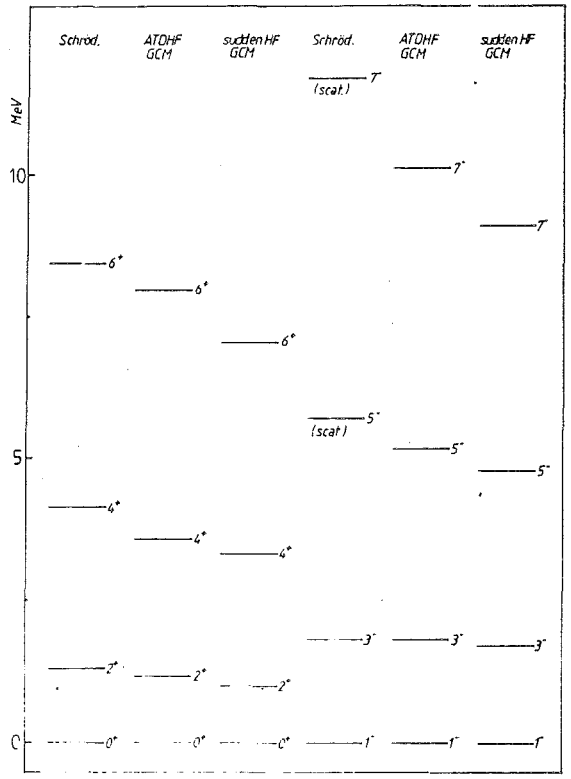

Fig. 17: Comparison between the lowest bands in ^{20}Ne by solving the Schrödinger equation, ATDHF+GCM and sudden-HF+GCM. The states indicated by (scat) were not obtained by a bound state calculation but from a phase shift analysis.

In Fig. 17 we compare the rotational bands obtained from solving the Schrödinger equation, ATDHF+GCM and sudden HF+GCM. The moments of inertia of the bands are not so much different, however the absolute position of the even and odd band heads differ appreciably. The L=1 band head is excited by 2.12 MeV (Schrödinger equation), 3.16 MeV (ATDHF+GCM) and 1.37 MeV (sudden HF+GCM) with respect to the L=0 ground state. Which structure wave functions (from which we have as many as discretization points were chosen) are the real quasi-bound

states of the compound nuclear system can be checked through a phase shift analyses or through the dependence of the energy position on the cut-off radius in the structure calculation.

7. GCM Scattering Calculations

To calculate scattering phase shifts one needs also the kernels at large separation distances in the asymptotic region (T26). Our procedure to construct wave functions in the asymptotic region is, however, so far not only very time consuming but one would also need a much bigger grid to allow for large separations. We therefore only constructed the kernels until the asymptotic region where only the Coulomb force is still active. From there onwards we used an analytic formula until we had in total 36 discretization points available. The analytic formula is derived from harmonic oscillator shell model wave functions with the same oscillator width b for the two clusters. For no interaction and no exchange between the clusters one obtains for free particles

$$N_\ell(q,q') = i^\ell \, j_\ell \left(-\frac{iqq'}{2\beta^2}\right) \exp\left\{-\frac{q^2+q'^2}{4\beta^2}\right\} \tag{N8}$$

$$H_\ell(q,q') = -\frac{\hbar^2}{2m\mu} \times \frac{2\ell+1}{\beta^2}\left\{\left(\frac{q^2+q'^2}{4\beta^2} - \ell - \frac{3}{2}\right)N_\ell - \frac{qq'}{2\beta^2} N_{\ell+1}\right\} \tag{N9}$$

$$\text{with} \quad \beta = \frac{b}{\sqrt{\mu}} \tag{N10}$$

To this hamilton kernel the Coulomb kernel has to be added. The b value can either be fitted so as to obtain a continuous kernel function or it can also be obtained from the following formulae for harmonic oscillator wave functions

$$\frac{\hbar^2}{2\mu} \langle \phi_q | \hat{P}(q)^2 | \phi_q \rangle \underset{q\to\infty}{=} \frac{1}{4}\hbar\omega \tag{N11}$$

$$\text{with} \quad b^2 = \frac{\hbar^2}{m\hbar\omega} \tag{N12}$$

or for all ℓ

$$\frac{\hbar^2}{2\mu} \frac{\langle \hat{P}_\ell \phi_q | \frac{\partial}{\partial q} \frac{\partial}{\partial q} | \hat{P}_\ell \phi_q \rangle}{\langle \hat{P}_\ell \phi_q | \hat{P}_\ell \phi_q \rangle} \underset{q \to \infty}{=} \frac{\hbar^2}{m} \times \frac{1}{4b^2} \tag{N13}$$

Calculation of the left hand side of (N13) for two neighbouring asymptotically obtained wave functions then gives an estimate for the oscillator width which we should take for the analytic formula.

i) qATDHF

The phase shifts obtained with the ATDHF kernels are presented in Fig. 18. They are obtained with a b-value (N13) equal to 1.637 fm. We shifted them over $n\pi$ with n fixed according to Levinson's theorem for two centre shell model wave functions. The ℓ = 1 and ℓ=4 should show a sharp resonance around 1 MeV and 1.50 MeV respectively. However due to the Coulomb interaction the method that was used does not allow for small CM energies according to the condition (Ba72)

$$kr \geq \frac{5}{3} n(k) + 7.5 \tag{N14}$$

with

$$n(k) = \frac{2\mu}{\hbar^2} \frac{Z_1 Z_2 e^2}{2k} \tag{N15}$$

$$E_{CM} = \frac{\hbar^2 k^2}{2\mu} \tag{N16}$$

which would mean for E_{CM} = 1 MeV kernels up to $r \geqslant 40$ fm should be taken into account. The positions of the GCM structure states are indicated by the verti-

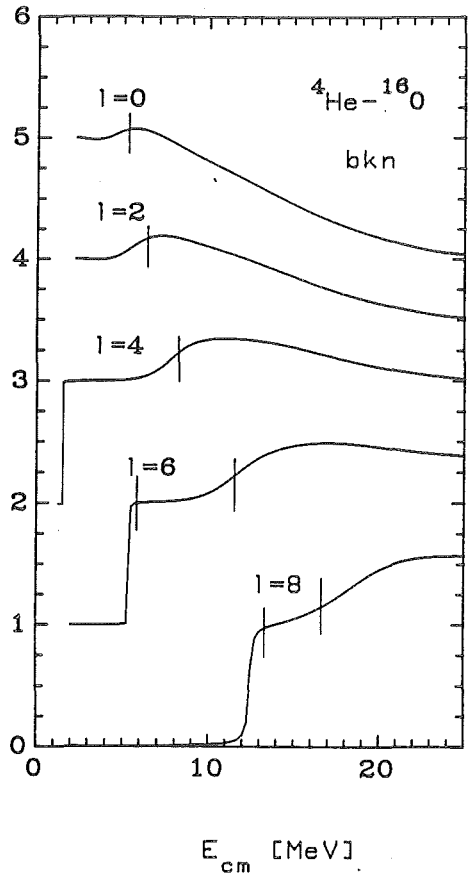

Fig. 18: Phase shifts of even partial waves using the ATDHF generating functions. The vertical lines denote the positions of the structure wave functions.

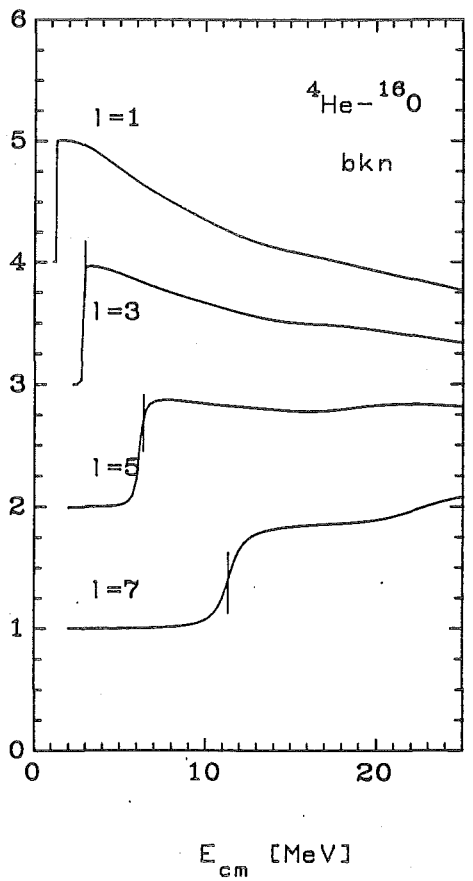

Fig. 18: Phase shifts of odd partial wave using the ATDHF generating functions. The vertical lines denote the positions of the structure wave functions.

cal lines. The phase shifts do correspond quite well to the results obtained in the literature (Fi76,Ma75,He76) except of course that our ℓ=1,3,4 have no bound states and hence appear as scattering resonances which is experimentally indeed the case for ℓ=1 and ℓ=3. The results shown are the results obtained after eliminating linear dependences according to a cut-off parameter of 1.D-4. This throws away 3 linear dependent ones in the interaction region up to 4 fm in the octupole coordinate distance. Changing the cut-off parameter a little such that only 2 are neglected then all odd phase shifts get very sharp extra resonances some 4-5 MeV above the first resonance, but do not change

elsewhere. The even partial waves do not change at all. Repeating the structure calculation with a smaller cut-off parameter also leads to an extra odd-ℓ band at the same positions as the extra scattering resonances. Two facts should be considered in this context. Although N_ℓ and H_ℓ go to zero for odd ℓ in the limit of the symmetric HF state the H_ℓ/N_ℓ value should tend towards a finite value. Due to the fact that our numerical methods do not give the same accuracy for the destination of the norm and hamilton kernel, problems start to occur close to the HF point for the odd ℓ values. Secondly instead of taking discretization points with a constant distance between them in some coordinate one should select the points according to their norm overlap with the other chosen wave functions, so that automatically then those points should be ignored which lie "close" to the HF point. Hence the above mentioned sharp resonances in the oddℓ phase shifts do not contain physics but are results of an overcomplete basis. It should also be noted that all phase shifts are no longer smooth-behaving above 30 MeV. This will be discussed in the section about the α-α system.

ii) HF sudden approximation

Since there is no difference with the qATDHF kernels in the asymptotic region the same b-value (N13) has to be taken. The results are shown in Fig. 19 and are completely different from the ones obtained with the ATDHF kernels. Although it is often believed that the sudden approximation is a valid one for the calculation of e.g. α-spectroscopic factors (Fl76), our results show that with semi-realistic forces like BKN only adiabatic wave functions result in good agreement with the experimental situation of the α-^{16}O system.

Indeed, although the two approaches use the same interaction and the same asymptotic wave functions, only the adiabatic approximation leads to a ground

state band with small α-decay widths and to an approximate description of the higher-lying 0_4^+ band.

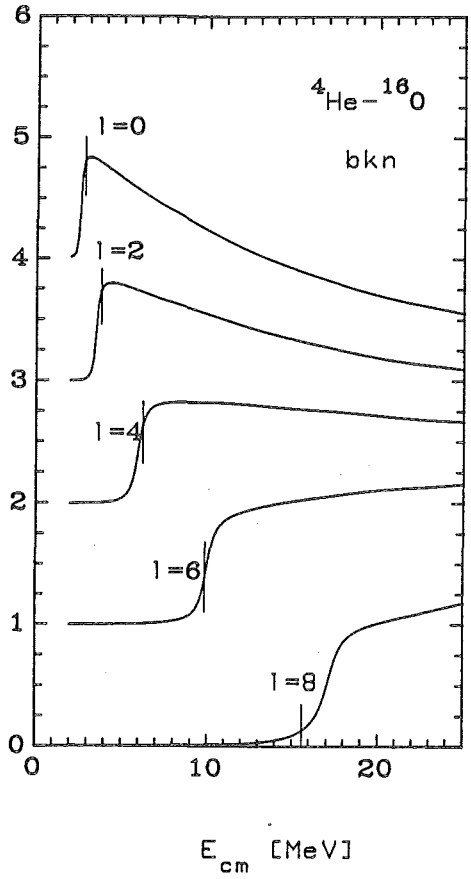

Fig. 19: Phase shifts of even partial waves using the sudden-HF wave functions. The vertical lines denote the positions of the structure wave functions.

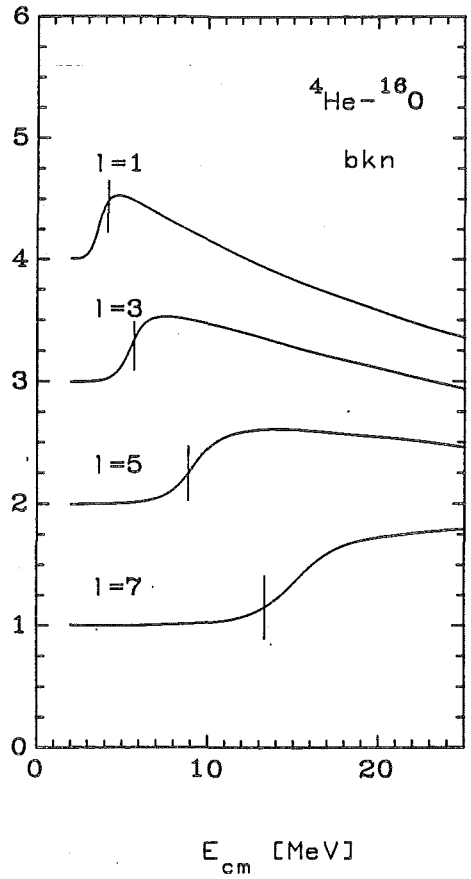

Fig. 19: Phase shifts of odd partial wave using the sudden-HF wave functions. The vertical lines denote the positions of the structure wave functions.

8. Poles and Decay Widths

The S-matrix defined through the phase shift, eq. (T20),

$$S_L(E) = e^{2i\delta_\ell(E)} \tag{N17}$$

can have poles in the complex E plane. Making use of the definition of the statistical operator (Di28,Ne32) one can show (Fr65,Fr70) that the decay widths of unstable nuclei are given by the position of the poles of the S-matrix. The only assumption is that only the α-decay channel is open and hence no γ-decay to bound states can occur. One has therefore to extend the GCM method to complex energies in order to extract the S_L-matrix. It is, however, more convenient to introduce another function, the K-matrix, which has a regular behaviour at the poles of the S-matrix. The definition of the K-matrix is

$$K_L = i\,\frac{1-S_L}{1+S_L} \tag{N18}$$

and for $S_L \to \infty$ one has $K_L \to -i$. Since K_L has singularities for $\delta_\ell = (n + 1/2)\pi$ it might in some cases be more convenient to use K_L^{-1} which shows in turn singularities for $\delta_\ell = n\pi$. Making use of the K_L matrix one has to choose a mesh in the complex energy plane such that it overlaps -i in the K_L plane. Choosing a finer net around the pole one can determine the corresponding complex energy to any desired accuracy. An example is given in Fig. 20. Position and width of some states are summarized in Table 5.

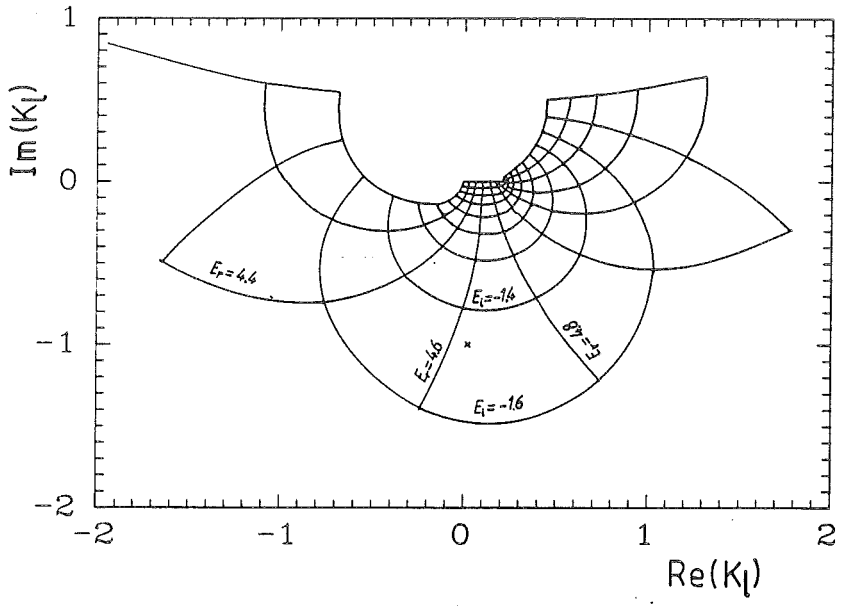

Fig. 20: Example of locating the resonance pole in the ℓ=0 partial wave scattering α-^{16}O (qATDHF). The cross indicates the position of the pole of the S-matrix. The real and imaginary parts of the energy E_r,E_i are given in MeV.

J^π	E_{th}	Γ_{th}	E_{exp}	Γ_{exp}
6^+	5.425	.005	4.05	.00011
8^+	12.435	.128	7.22	.000035
5^-	6.118	.175	5.53	.141
7^-	11.358	.658	10.61	.380
0^+	4.63	1.49	3.57	>.800
2^+	5.53	1.51	4.07	>.800
4^+	7.81	1.69	6.06	.350
6^+	11.31	2.47	7.85	.088
8^+	18.40	2.84	12.57	.213

Table 5: Energies with respect to the α-^{16}O threshold and widths in MeV obtained in qATDHF with the BKN interaction. Experimental values come from (Aj83).

As can be expected the widths only compare with the experimental ones if the position is close to the experimental position. Since the 0_2^+ band has a much smaller decay width we have to compare our second even-ℓ band with the 0_4^+ band

from the experiment. The spectra are shown in Fig. 21. The indicated calculated bound states are the ones from the GCM structure calculation.

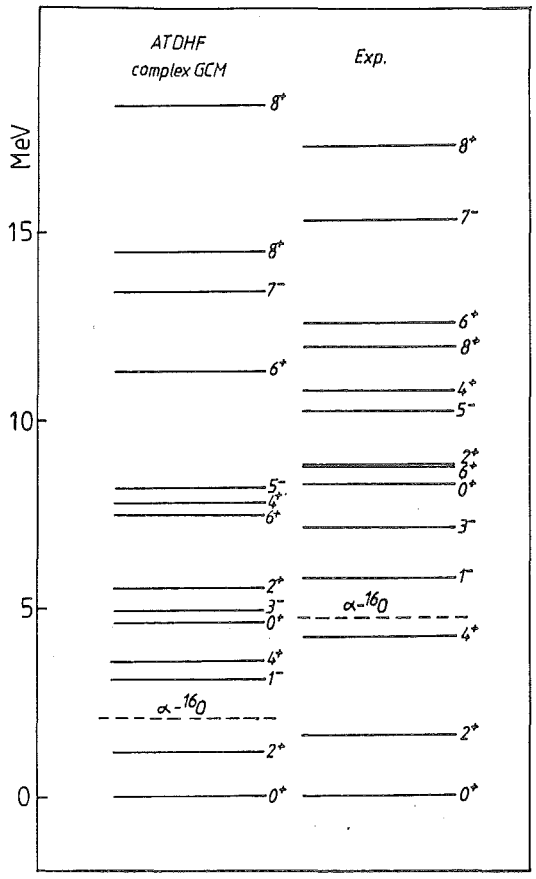

Fig. 21: α-^{16}O spectra of the 0_1^+, 0^- and 0_4^+ bands compared with the qATDHF calculation using the complex GCM method for the location of the scattering resonances. We indicated also the α-^{16}O threshold energies.

9. Inclusion of Other Structural Configurations

The $(sd)^4$-shell model calculation for ^{20}Ne (Ak69) describes the $K^\pi = 0_2^+$ band in ^{20}Ne as having the dominant $SU_3(4,2)$ component. Later on in a microscopic five alpha cluster model in the GCM framework it is found (Ne75) that these shell model configurations with $SU_3(4,2)$ symmetry can be expressed by the superpositions of the α-^{12}C-α configurations. The admixtures of the α+^{16}O cluster components in this picture then also explained the large α-reduced widths of this 0_2^+ band. The α+^{16}O and ^8Be+^{12}C coupling model (Fu79), on the other hand, obtains also the $K_\pi = 0_3^+$ band in good correspondence to the experimental features.

Since it is very easy in our program to start with different cluster configurations let us therefore also study the influence of enlarging the model space in order to investigate whether we can describe the different structure bands in the ^{20}Ne system.

i) The α=^{12}C=α symmetric configuration

We started the calculation with an α-^{12}C distance of 6 fm on both sides. We obtained in this way again a "collective" path which, due to the underlying symmetries, has to converge in the end to the same ^{20}Ne HF ground state. The path, followed in the (Q_{20},Q_{30}) plane, is shown in Fig. 22. The little deviations from the $Q_{30} = 0$ line are due to small numerical errors because in order to have an even number of points on the z-axis for the Fourier transform subroutines we have 1 point less on one side of the grid. 10 discretization points were selected along this path and the GCM structure calculation was performed. The results are summarized in Table 6.

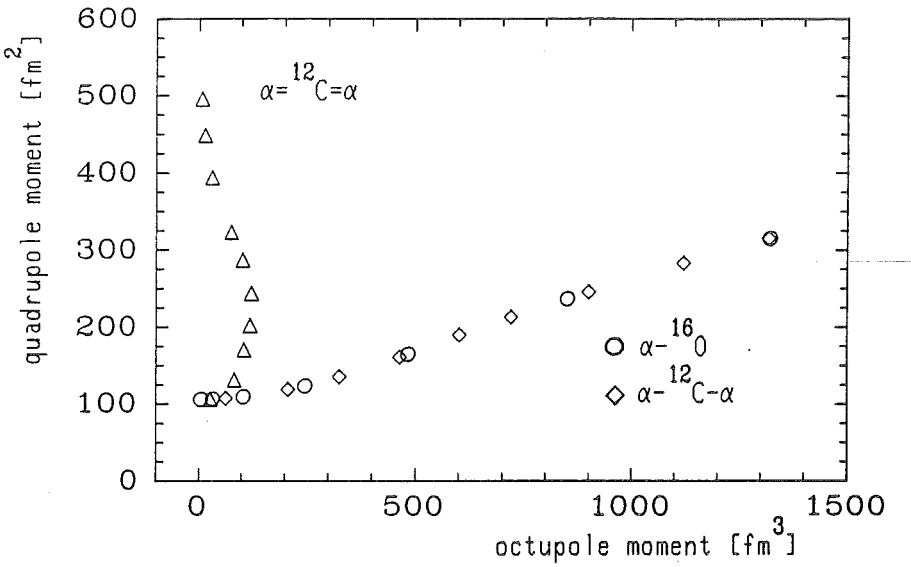

Fig. 22: The different collective ATDHF paths followed in the Q_{20},Q_{30} plane for α=^{12}C=α, α-^{16}O and α-^{12}C-α using the BKN interaction.

L	0	2	4	6	8
	-.32	.59	2.76	6.43	12.79
	14.03	14.55	15.75	18.21	23.06
	23.19	24.05	25.56	28.38	32.96
	32.33	32.94	34.23	36.60	39.96

Table 6: Energies in MeV with respect to the α-^{16}O threshold for the GCM structure calculation with the α=^{12}C=α wave functions.

Coupling the α-^{16}O wave functions to enlarge this basis gives the spectra of Table 7.

L	0	1	2	3	4	5	6	7	8
	-2.34	1.07	-1.33	2.91	1.05	6.27	4.94	11.25	11.31
	5.14	7.99	5.91	9.34	7.76	11.73	10.83	15.58	15.35
	10.92	16.25	11.67	17.54	13.46	19.95	16.45	23.82	21.23
	14.99	22.45	15.49	23.51	16.78	25.49	19.27	28.82	23.64
	20.92	27.99	21.74	29.25	23.62	31.48	26.88	35.23	31.81

Table 7: Energies in MeV with respect to the α-^{16}O threshold for the structure calculation with the coupling of the α-^{16}O configurations with α=^{12}C=α.

Comparing Table 7 with Table 3 and Table 6 shows that there is almost no mixing between the 2 configuration spaces except for the lowest band which has as a big component the HF ground state which is common to the 2 spaces.

If one would plot the energies that correspond to the points in the (Q_{20},Q_{30}) space one would immediately understand why inclusion of the $\alpha=^{12}C=\alpha$ configurations does not lead to an extra state between the 0_1^+ and 0_4^+ bands. The valley along the $\alpha-^{16}O$ path is really too steep in the Q_{20} direction to allow for a new mode. Repeating the full calculation with the Skyrme III force even worsens this situation a little.

ii) The $\alpha-^{12}C-\alpha$ asymmetric configuration

In order to fill up the configuration space between the two paths of $\alpha-^{16}O$ and $\alpha=^{12}C=\alpha$ in Fig. 22 we tried also to start with an asymmetric configuration. However, the ATDHF generating procedure immediately forces the system to fall down in the $\alpha-^{16}O$ path as shown in Fig. 22 even with taking as starting configuration an α-particle at 5 fm and the other at 6 fm with respect to the ^{12}C central system. This is in accordance with the fact that qATDHF is designed to describe the lowest modes of the system.

Within the one parameter ATDHF version it seems not possible to fill up the full (Q_{20},Q_{30}) plane; one would need a 2 dimensional ATDHF energy surface.

The $\alpha+\alpha \leftrightarrow {}^{8}Be$ System

1. Introduction

The existence of a strongly tight alpha particle has been one of the main fundaments which led to the alpha-particle model of the 4n nuclei. α-molecular aspects of a nuclear system can however only be expected when the nucleus can be divided into two (or more) subunits without a great loss in binding energy. This means that the threshold into the 2 cluster channel must be close to the quasibound or bound structure states of the compound nucleus under consideration. An example is the α-^{16}O system where the threshold lies inbetween the ground state band and the first odd parity band of the ^{20}Ne system. The reason why such an α-particle does not dissolve completely into the combined system can be understood by considering the Pauli principle. This influence of the antisymmetrization has already been often investigated (Sa69,FT76,Wi77,La79). Especially in the case of ^{8}Be the Pauli principle prevents the two α-particle s-waves to interpenetrate into each other such that the ^{8}Be ground state is almost a pure α+α cluster configuration and a narrow potential resonance with respect to the α+α decay channel.

The α-α system has been investigated in numerous models, among which the α-cluster model of Brink (Br65) is very convenient to calculate the equilibrium form of its nearly bound state ^{8}Be. In this state the α-clusters have been shown to be mutually polarized (Ra72,Ar81). In order to treat correctly the relative motion for 2 colliding nuclei one has to extend these models as is possible in the generator coordinate method. α-α scattering in the GCM framework can be found in the following references (Ho70,Ba70,dT72,Ta73,Fr74,Ba74, Hu77). All these calculations however do not take into account the distortion of the ions during the collision.

That distortion is important can be seen from our α-^{16}O results in the comparison qATDHF+GCM and HF-sudden+GCM and a similar result for ^{16}O-^{16}O was obtained by Reidemeister (Re72). However due to the tightness of the α-particle the effect of distortion in the α-α phase shift will be relatively minor (Ni71). Nevertheless, it has been pointed out by Schmid and Schwager (Sc73) that the inclusion of distortion can lead to narrow resonances which are caused by the presence of channels which are not open in the model space.

An extensive study including deformation in the α-α system was performed by Deumens (De82), where first the connection between the structure and scattering states is analyzed, and second, the conclusion is made that, although their model space only consists of 2 equally polarized α-particles, the α+α* configuration is also present in this model space. Therefore some resonances can be obtained with the α+α* structure if this channel is not open in the model space. If the additional channel is opened these resonances might turn into normal transit states. For quasibound states one would obtain a wiggle (Fu77,Fi81) in the phase shift which corresponds to a one-level-two-channel Breit-Wigner formula. It would therefore be good to know the effects of the distortion brought about by the qATDHF in comparison again with the HF sudden approximation.

2. GCM Structure Calculations

i) qATDHF

The diagonal kernels H_0/N_0 are shown in Fig. 1. For the GCM structure calculation points were taken into account up to 6 fm and the results are summarized in Table 1. A smaller cut-off estimate parameter was taken then in the α-^{16}O case because we want to consider also the high-lying structure levels in ^{8}Be.

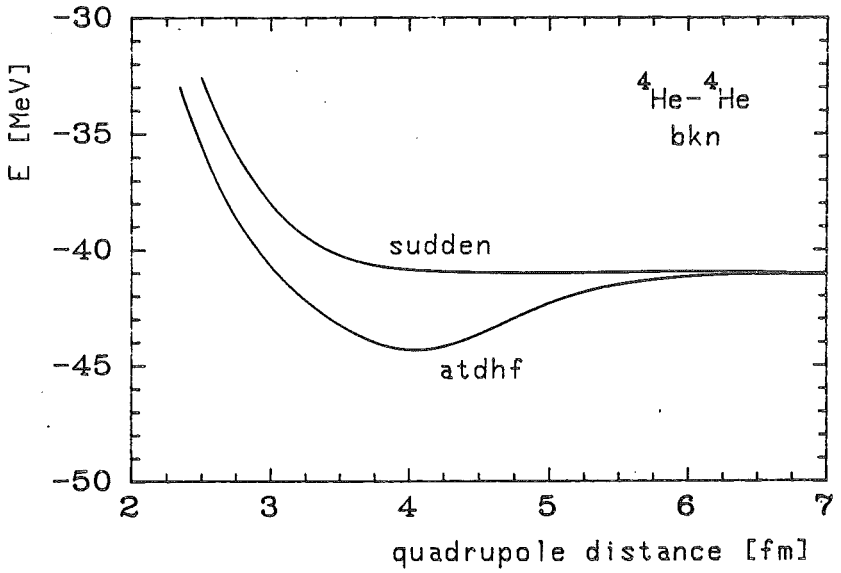

Fig. 1: Diagonal kernels H_0/N_0 obtained with qATDHF and in the HF-sudden approximation with the BKN interaction.

ii) HF sudden approximation

The H_0/N_0 potential is compared in Fig. 1 with the qATDHF one. It is a very flat potential which shows no such clear minimum as the qATDHF one. The results of the structure calculation are listed in Table 2. A comparison between both calculations and experiment is shown in Fig. 2. One notices that the first three levels are rather the same in these two model spaces. This is

L	0	2	4
	.36	2.85	8.69
	6.68	8.37	12.99
	18.28	19.69	23.21
	27.02	28.61	30.98
	35.58	37.49	40.48
	40.65	43.61	45.01
	48.75	50.70	62.11

Table 1: Energies in MeV of the GCM structure calculation with respect to the $\alpha+\alpha$ threshold using the qATDHF wave functions.

L	0	2	4
	1.35	3.68	8.64
	6.79	8.42	13.03
	16.69	18.08	21.15
	32.16	32.86	34.15
	52.11	52.91	52.04
	75.50	85.92	79.19

Table 2: Energies in MeV of the GCM structure calculation with respect to the $\alpha+\alpha$ threshold using the HF sudden approximation.

in complete agreement with the results obtained by Deumens (De82) in the comparison between his "T-model" (distortion at r=0) and the cluster model. He uses the B1 interaction. Our spectrum is however a little more compressed (considering one ℓ-value) which is in better agreement with experiment. The situation for the higher levels, on the other hand, is different. Deumens obtains 2 further levels in the T-model before the appearance of a level in the cluster model whereas in our spectrum the next level in the HF sudden approximation appears next to the 4th one obtained with qATDHF.

The position and number of these higher levels will however depend on the type of distortion that is taken into account, cfr in the "ψ model" (distortion

until some finite radius) of Deumens an extra level appears. Another important difference is that we have a one dimensional path in our qATDHF model space, which means for a definite distance that only 1 wave function is considered. We can compare it with taking wave functions along the valley of the energy surface constructed in this "ψ model". It further follows from his scattering analysis that the 4th structure state has the $\alpha+\alpha^*$ configuration structure and is seen as a sharp resonance in the scattering phase shifts.

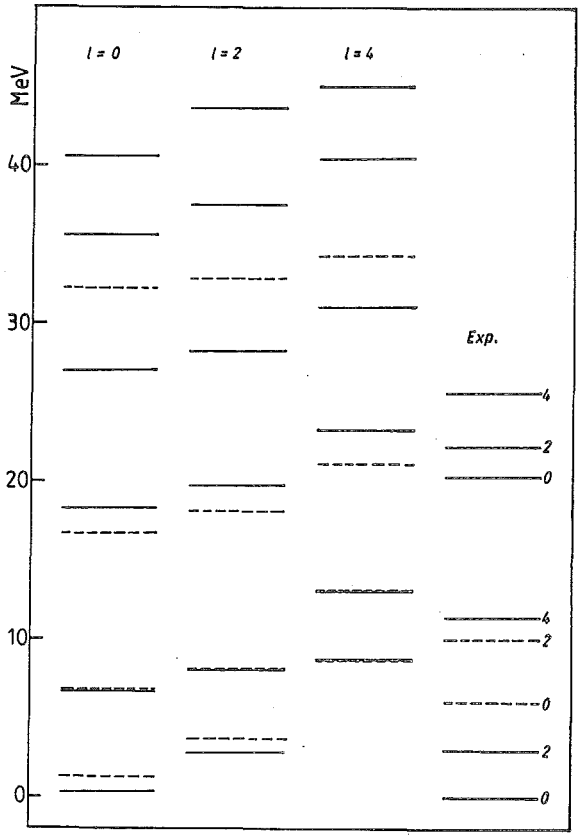

Fig. 2: qATDHF+GCM for bound states (full lines) compared with the HF-sudden + GCM bound states (broken lines) for the α-α system using the BKN force. The experimental situation is shown in the last column. The dashed lines correspond to the very broad resonances of the experimental second band.

3. GCM Scattering Calculations

i) HF sudden approximation

The phase shifts δ_0, δ_2, δ_4 are shown in Fig. 3. The ℓ=0 phase shift is not shown for smaller energies again because of the inclusion of the Coulomb interaction which, due to technical reasons, does not allow for very small energies. They agree with the experimental ones in this energy region so far as the ^{7}Li+p channel is not important, which is not included in our approach. This channel opens at 17.35 MeV.

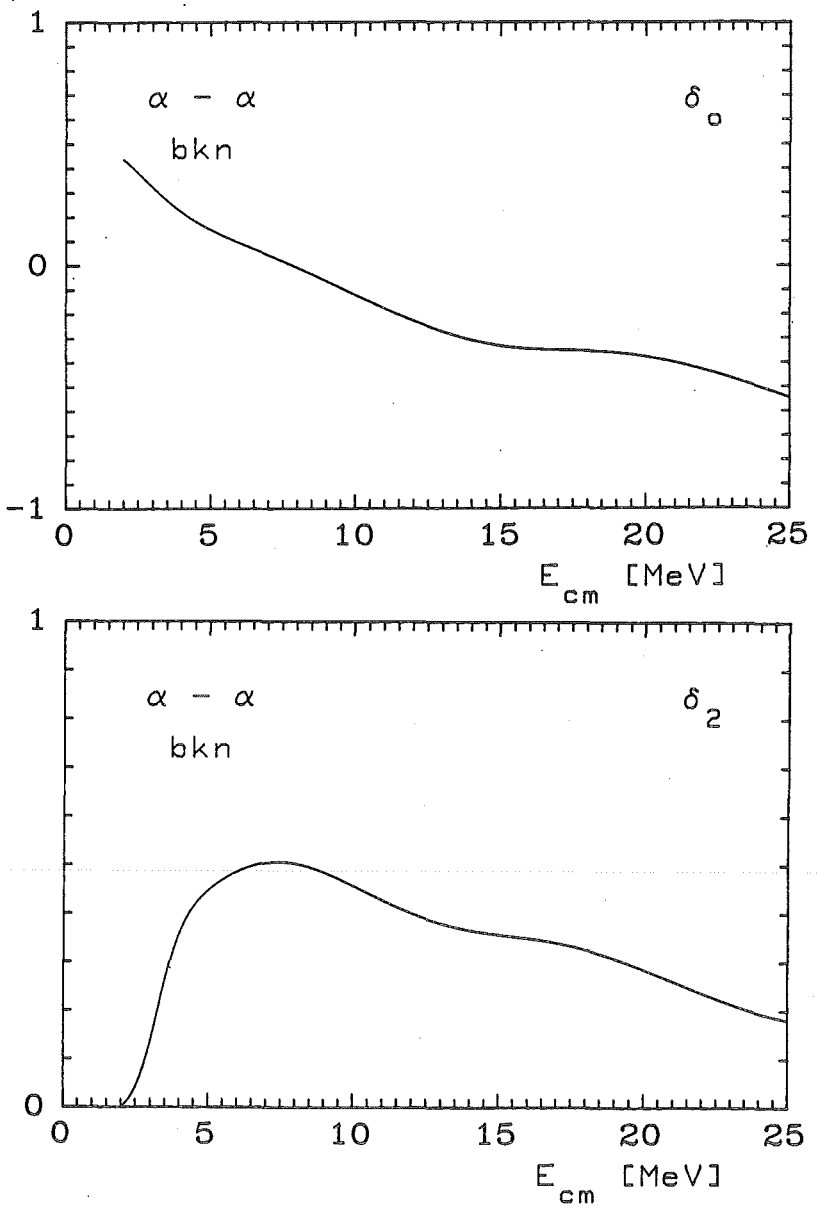

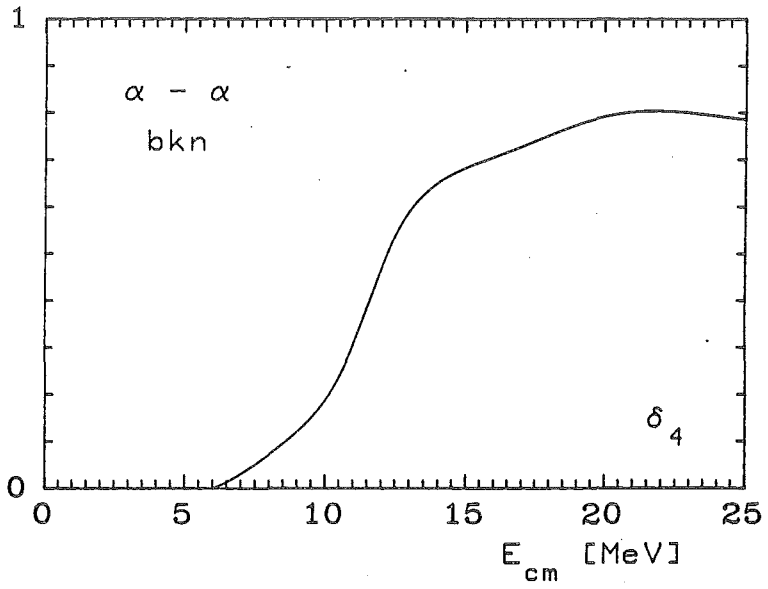

Fig. 3: Phase shifts δ_ℓ ℓ = 0,2,4 for α-α scattering in the HF-sudden approximation.

ii) qATDHF

The α-α phase shifts are compared with the experimental ones in Fig. 4 up to 20 MeV. The arrows mark the opening of other channels which are not included in our model space. The experimental data are copied from (De82) and are taken from (He56,To63,Ni58,Ch74,BR72). First calculations showed a broad bump structure with a small one on top of it starting at ±30 MeV in the ℓ=0,2,4 phase shifts. Throwing away linear dependent rows in the input matrix until only 6 discretization points are retained for the inner region results in the phase shifts shown in Fig. 5.

Although they are not nice sharp resonances according to their interpretation (De82), their position seems to correspond with the 27.02, 35.58 and 48.15 MeV levels obtained for ℓ=0 in the GCM structure calculation. This would then correspond with the results of the "ψ model" except for the fact that the 4th

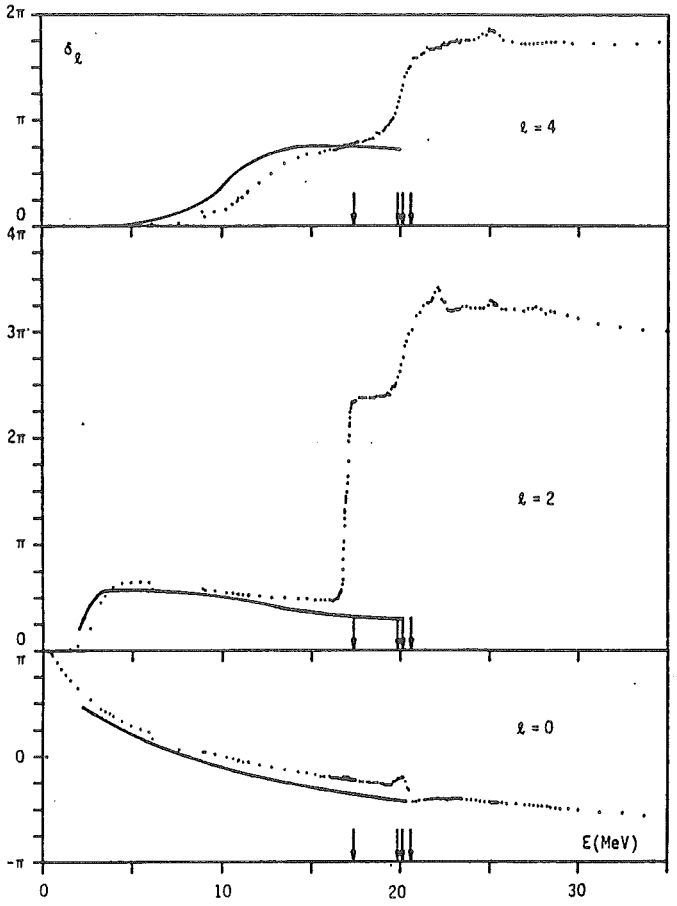

Fig. 4: Comparison of the experimental α-α phase shifts with our qATDHF calculated results. The arrows mark the thresholds of other channels.

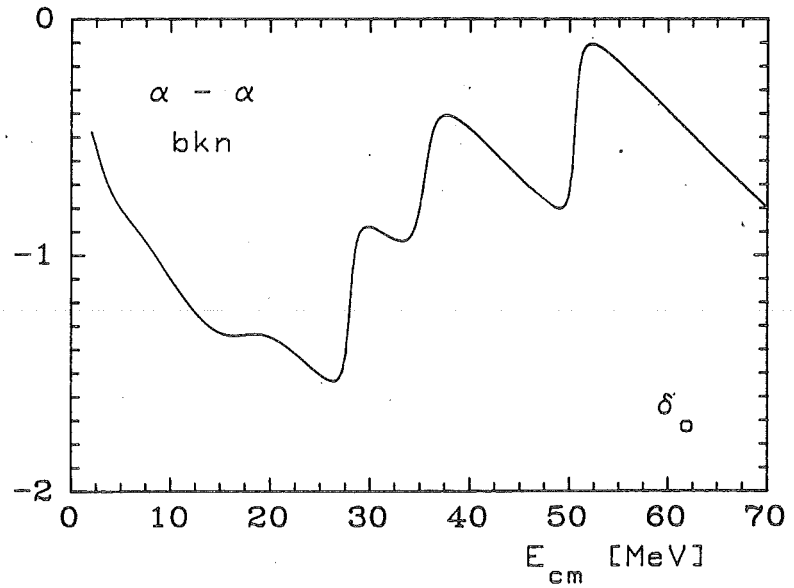

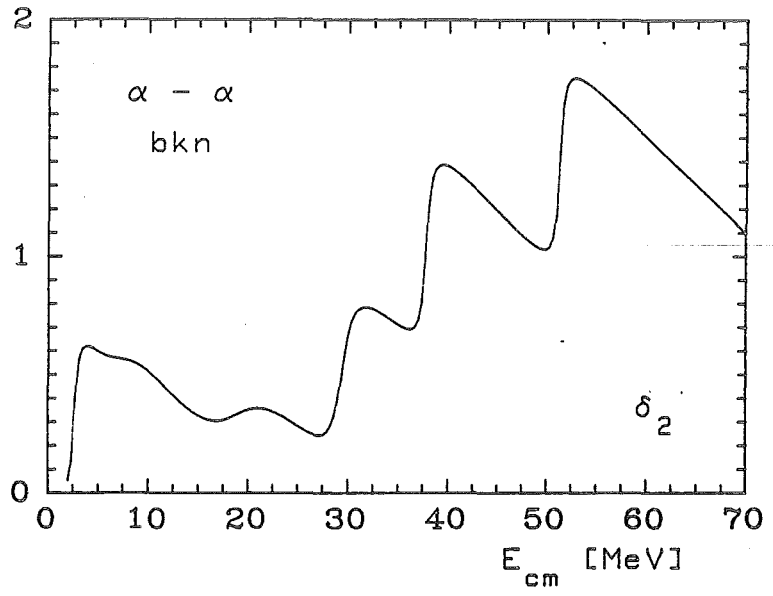

Fig. 5: Phase shifts δ_ℓ ℓ = 0,2 obtained in the qATDHF space.

state in the HF sudden approximation should lie somewhat higher if its structure is to be the same as that of the 40.65 MeV ℓ=0 level. A crucial test is the position of the α^* state in our model space which should then be expected to be at $\pm$27 MeV.

4. The Breathing Mode of 1 α-Particle

Experimentally the first excited state of the α-particle lies at 20.1 MeV, has $J^{\pi} = 0^+$ T=0 and is rather long-living until it decays into t+p. Theoretically it is usually treated as the shell model state of $2\hbar\omega$ excitation or the breathing mode state (Br82). Its character is however not so clear and because of its large single-nucleon reduced width attempts with a 3+1 nuclear structure have also been made (Fu78). Due to our quartet symmetry we are restricted to the breathing mode structure. We therefore change the oscillator width of the Gaussian input s-wave function for the α-particle and take it as $\delta \times 4^{1/6}$ fm.

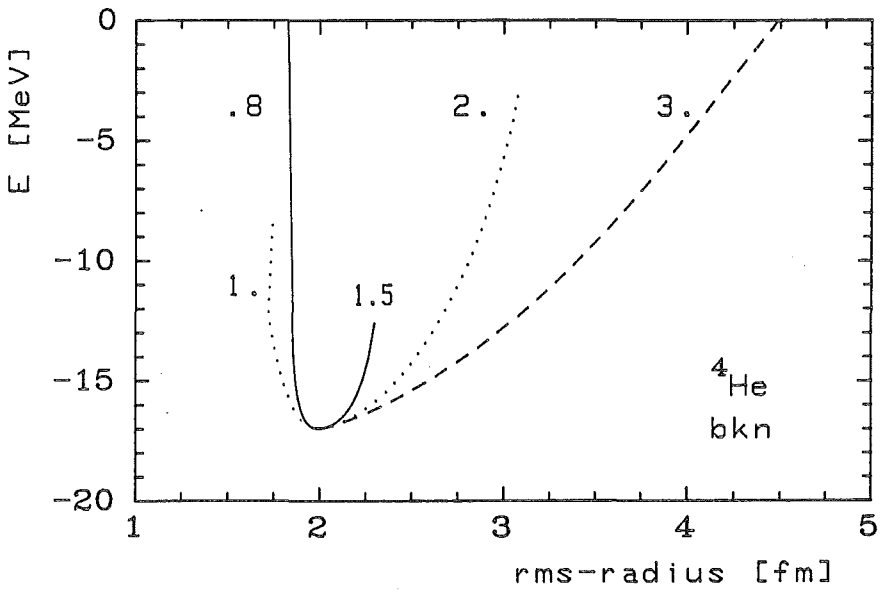

Fig. 6: "Collective" spaces obtained in qATDHF starting with different oscillator widths for the initial gaussian wave function. $b = \delta \cdot A^{1/4}$ fm and the δ is indicated in the figure.

In Fig. 6 we plotted the obtained qATDHF "paths" falling down to the HF ground state of ^{4}He. The indicated numbers are the different δ values which were chosen. This shows that the qATDHF procedure does not merge in this case into some maximal decoupled collective space.

Since all states are however Slater determinants we can interpret the lowest curves in energy as an approximation to a constrained Hartree-Fock calculation where the rms radius would be the constraint. Therefore taking the $\delta = 1.$ curve and the $\delta = 3.$ curve and performing a GCM calculation we obtain the spectrum of Table 3.

L=0
-16.78
0.94
9.10
11.20
28.65

Table 3: Energies in MeV of the GCM breathing mode calculation for 1 α-particle with the BKN force.

This would mean only an excitation energy of 17.72 MeV for the α* in contrast to the expected 27 MeV.

One could think of taking only a deformation in z-direction because our α-particles get deformed in the collision direction in performing qATDHF. However in this approximated model the excitation energy remains 17 MeV.

Several points should be considered now:

1. No centre-of-mass correction was performed which might be too crude for such a light system like α-α.

2. Since the α-particle is so small it is really going to the limits of our present grid dimensions. We can of course easily take smaller distances between the grid points but then in performing the angular momentum projection errors occur in the asymptotic region because then the dimensions

in x and y direction are getting too small (see Appendix) to rotate the α-α chain.

Especially for the phase shifts which do not look very smooth the grid effects were checked in some analytic model with kernels defined through

$$N_0(q,q') = \exp\{-\lambda(q-q')^2\}$$

$$H_0(q,q') = N_0(q,q')\{V_{SW}(q)+B_0(q-q')^2\}$$

with

$$V_{SW}(q) = \frac{V_0}{1+\exp\{\frac{q-q_0}{a}\}} + V_{clb.}$$

Adding oscillations to N_0 by multiplying with

$$\{1+\alpha \sin k(\frac{q+q'}{2})\}$$

causes oscillations to occur on top of previously obtained smooth phase shifts even for α = .01 values. As was mentioned at the end of the ^{20}Ne chapter there the phase shifts showed some structure at energies around 30 MeV, too. They might be of the same nature as the α-α ones.

3. It might also be that our qATDHF collective space, although it polarizes both α-particles too, does not include fully the combination of our constructed α^* wave function and normal α wave function as is the case in (De82). Therefore the qATDHF α^* present in the α-α space could be at a higher excitation energy.

The $\alpha+^{12}C$ Structure of ^{16}O

1. Introduction

So far we have been concerned with 2 cluster systems which are both spherical outside the interaction region. The α-^{12}C structure of ^{16}O encloses the possibility to investigate how the influence of the deformation of the carbon nucleus appears in the qATDHF concepts.

The first excited state of ^{16}O, often called the "mysterious second zero plus state" (Fu80), has been a keystone to the understanding of the structure of ^{16}O. Just as for the ground state of ^{20}Ne it is a head of a rotational band. Following the calculations of (Ca64,Mi64), the α-particle resonant scattering on ^{12}C shows a second rotational band of odd parity states which have a large reduced α-width (Ro60). This leads to the suggestion that these states of the $K_\pi = 0^-$ band consist of an α-cluster rotation outside the ^{12}C nucleus. This idea was then extended to the positive parity band because of the inversion doublet model of Horiuchi and Ikeda (Ho68).

The Orthogonality Condition Model (OCM), with inclusion of the 2^+_1, 4^+_1 excited states of ^{12}C in a coupled channel approach, is able (Su74,Su76,Su78) to reproduce the spectra of all T=0 levels below 13 MeV. This requires, however, the inclusion of adjustable strength parameters. Nevertheless this study found the 6.06 and 9.6 MeV rotational bands to be approximately represented by the α-^{12}C (0^+) channel alone. Therefore, since we are interested in the low energy spectra, we can restrict ourselves to the dynamics of the α+^{12}C system and compare our qATDHF results with the ones obtained in the usual GCM-like theories (Ho73,HH77,Ba77,Li80).

2. Approximate Projection of ^{12}C on 0^+

The partial wave version of the Hill-Wheeler equation (T12) is restricted to spherical nuclei. We therefore have to project first the ^{12}C nucleus on its 0^+ ground state. The details of the corresponding angular momentum projection are given in the Appendix A1. Using the BKN interaction, one obtains an energy gain of 4.26 MeV with respect to the unprojected energy expectation value.

The qATDHF procedure, however, describes the dynamics of the cluster system as a whole without allowing the projection of one cluster separately during the construction process (T36) of the collective path. However, one can study the changes in the dynamics of the cluster system by putting each deformed cluster in a different initial starting position (Ni85). Only afterwards one is then able to add up the different systems with weighing factors in order to obtain an angular momentum projected state of one of the clusters. This procedure is only meaningful in the asymptotic region for two well separated fragments since in the internal region of strong overlap one cannot distinguish between the different clusters and hence the projection becomes senseless. This becomes also clear through the fact that the different collective paths do not have necessarily the same range of the (identically chosen) collective coordinate. What we need is therefore a wave function which in the asymptotic region should be

$$|\phi\rangle = |\alpha - {}^{12}C(0^+)\rangle \qquad (01)$$

This wave function could be obtained through

$$|\phi\rangle = |\alpha - \int d\Omega\, D^0_{00}(\Omega) R(\Omega)\, {}^{12}C\rangle \qquad (02)$$

However, the qATDHF procedure would then have to construct the corresponding collective path for each Ω. Since this is too time consuming, we need an approximated method. Following the suggestion of Cugnon (Cu79) in the case of a ^{12}C nucleus we replace the integral in (02) by a 6 point $\{(0,\phi),(\pi,\phi),(1/2\pi,0),(1/2\pi,1/2\pi),(1/2\pi,\pi),(1/2\pi,3/2\pi)\}$ formula. This leads to

$$|\phi> = \frac{1}{\sqrt{3}} \{|\phi^x> + |\phi^y> + |\phi^z>\} \qquad (03)$$

where the notation $|\phi^x>$ means the 2 cluster Slater determinant consisting of an α-particle and the deformed ^{12}C nucleus with its symmetry axis pointing in x-direction. Because of the symmetries imposed on our grid and our initial wave functions the α-x and α-y collective paths can be obtained by constructing one of the paths and then interchanging the x and y axes to obtain the other configuration. Hence we are left with only 2 dynamical situations to be studied. Because the path propagator (T36) conserves the initially chosen parities in x and y direction the three different configurations will always stay orthogonal to each other, hence the norm factor will remain $1/\sqrt{3}$.

3. The Collective Paths

For this system a grid distance of .8 fm and E_{cut} = 155 MeV was chosen (Ni85). In Table 1 we summarize the binding energies of the different systems.

	E_{HF}	Z	E_{HF}-Z	exp.
^{4}He	-16.92	12.16	-29.18	-28.30
^{12}C(z)	-71.07	16.10	-87.17	-92.16
^{16}O	-116.72	10.68	-127.40	-127.62

Table 1: Binding energies in MeV for ^{4}He, ^{12}C with its symmetry axis pointing in z-direction and ^{16}O. E_{HF} denotes the uncorrected values, Z the amount of corrections and E_{HF}-Z the quantum-corrected binding energy. The experimental values are given in the last column.

What will be important for the following is the difference in binding energy between the asymptotic channel $\alpha+^{12}$C and the combined nucleus ^{16}O. Using the classical potential energy surfaces this energy difference amounts to 28.7 MeV, taking quantum-corrected values we get 11.0 MeV, whereas experimentally it is only 7.2 MeV. This difference between the theoretical and experimental binding energy, being primarily a property of the force, will certainly limit the quality of our calculations of the α-^{12}C scattering. In Fig. 1 we show the two different collective paths. For the axial situation in which the symmetry axis of the ^{12}C points towards the α-nucleus the combined system merges into the ^{16}O HF ground state. The non-axial configuration becomes also left right symmetric but has some 22 MeV less binding energy than the ^{16}O HF ground state. The reason why it has a finite octupole distance is due to the arbitrariness of our choice of a collective coordinate. The octupole distance has been constructed so as to obtain the right cluster distance in the asymptotic region. For the α-^{12}C system the equation (N4) reduces to

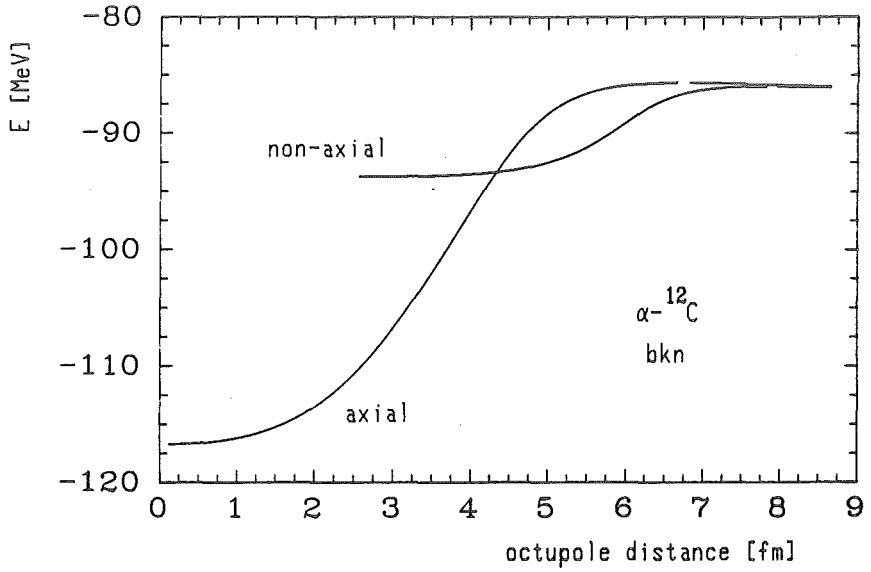

Fig. 1: Collective paths constructed with qATDHF for the α-^{12}C cluster system where the axial configuration is the one in which the symmetry axis of ^{12}C is pointing along the collision direction and the non-axial configuration has its ^{12}C symmetry axis pointing perpendicular to the collision axis.

$$3R^3 - \frac{3}{4} R\, Q_{20}(^{12}C) + Q_{30} = 0 \qquad (04)$$

with

$$Q_{20}(^{12}C) = -20.15 \text{ efm}^2 \text{ axial}$$
$$Q_{20}(^{12}C) = 10.35 \text{ efm}^2 \text{ non-axial}$$

For both cases one has $Q_{30} \to 0$ for the minimum of the energy curve but only for the axial symmetric case the R=0 solution is the continuous extension.

A similar problem holds for the quadrupole distance

$$6R^2 + Q_{20}(^{12}C) - Q_{20} = 0 \qquad (05)$$

which for both cases gives a finite value at the HF point, i.e. R = 4.46 fm in the non-axial case and R = 2.59 in the axial case although ^{16}O is a spherical symmetric system.

The mass parameters (T34) are very similar to the ones in the α-^{16}O case and are therefore not shown here. They tend again to the reduced value of 3 in the asymptotic region and have a maximum of 5 (4.5) around 4.75 (6.70) fm in the quadrupole distance. The values in brackets are for the non-axial case. Again a divergency emerges in coming closer to the HF point and it can be overcome if one is using the octupole distance.

4. GCM Structure and Scattering Calculation

Since we project the ^{12}C nucleus on its 0^+ ground state we need to calculate the kernels $\langle\phi_q|\hat{H}\hat{P}_\ell|\phi_{q'}\rangle$ and $\langle\phi_q|\hat{P}_\ell|\phi_{q'}\rangle$ with ϕ_q given by the linear combination of Slater determinants constructed in (03). Since this system is again axial symmetric the angular momentum projection involves only one integration. We may write using (03)

$$\begin{aligned}\langle \hat{P}_\ell\phi_q|\hat{H}|\hat{P}_\ell\phi_{q'}\rangle = \frac{1}{3}\{&\langle\phi_q^x|\hat{H}\hat{P}_\ell|\phi_{q'}^x\rangle + \langle\phi_q^y|\hat{H}\hat{P}_\ell|\phi_{q'}^y\rangle + \langle\phi_q^z|\hat{H}\hat{P}_\ell|\phi_{q'}^z\rangle \\ &+ \langle\phi_q^x|\hat{H}\hat{P}_\ell|\phi_{q'}^y\rangle + \langle\phi_q^x|\hat{H}\hat{P}_\ell|\phi_{q'}^z\rangle \\ &+ \langle\phi_q^y|\hat{H}\hat{P}_\ell|\phi_{q'}^x\rangle + \langle\phi_q^y|\hat{H}\hat{P}_\ell|\phi_{q'}^z\rangle \\ &+ \langle\phi_q^z|\hat{H}\hat{P}_\ell|\phi_{q'}^x\rangle + \langle\phi_q^z|\hat{H}\hat{P}_\ell|\phi_{q'}^y\rangle\}\end{aligned} \tag{06}$$

The mixed kernels in (06) were proven to be very small in comparison to the non-mixed ones and will therefore be neglected. For q=q' this is even not an approximation. The physical meaning, as pointed out by Cugnon (Cu79), is that the interaction cannot change the orientation of the fragments. (06) reduces therefore to

$$\langle\hat{P}_\ell\phi_q|\hat{H}|\hat{P}_\ell\phi_{q'}\rangle = \frac{1}{3}\{\langle\phi_q^x|\hat{H}\hat{P}_\ell|\phi_{q'}^x\rangle + \langle\phi_q^y|\hat{H}\hat{P}_\ell|\phi_{q'}^y\rangle + \langle\phi_q^z|\hat{H}\hat{P}_\ell|\phi_{q'}^z\rangle\} \tag{07}$$

The diagonal contributions divided by the norm kernels are plotted in Figs. 2, 3 and 4 respectively.

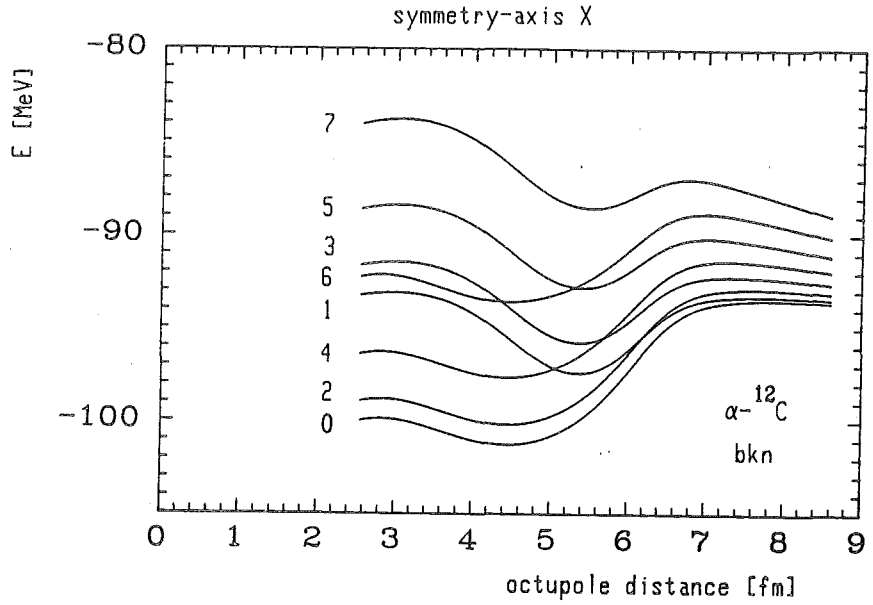

Fig. 2: $\langle\phi_q|\hat{H}\hat{P}_\ell|\phi_q\rangle/\langle\phi_q|\hat{P}_\ell|\phi_q\rangle$ for the qATDHF wave functions of the α-^{12}C system with initial symmetry axis of ^{12}C pointing in x direction.

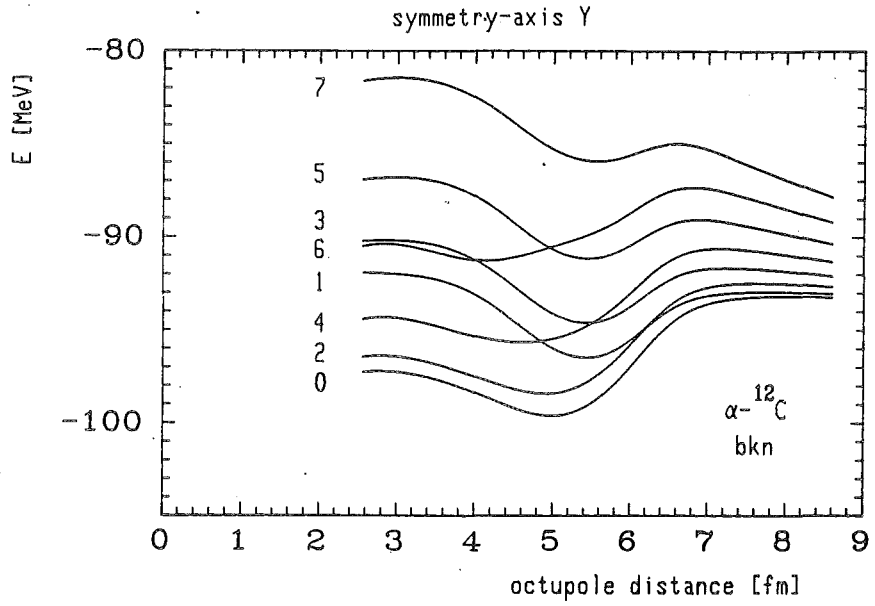

Fig. 3: Same as Fig. 2 but pointing in y direction.

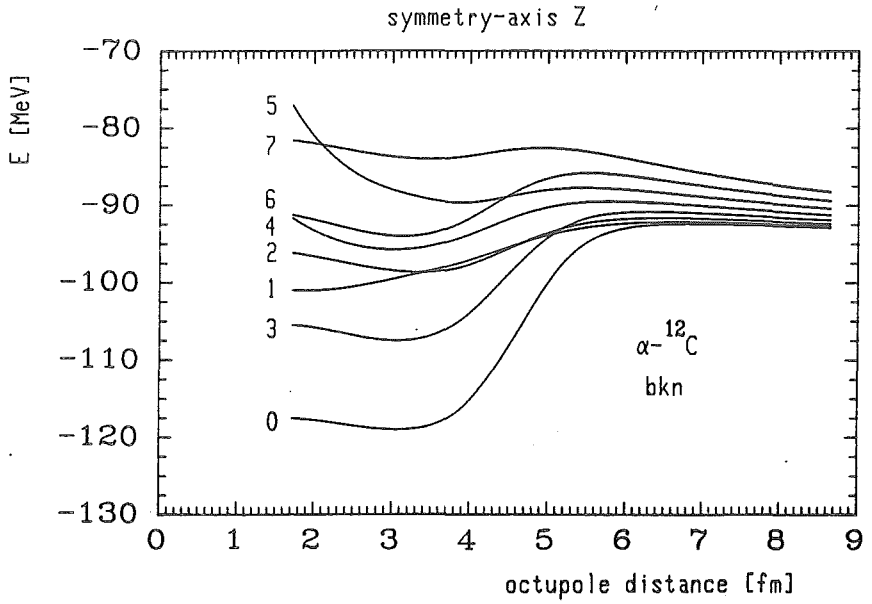

Fig. 4: Same as Fig. 2 but pointing in z direction.

As a first approximation we take only the kernels of the α-z configuration since it is the energetically more favourable one and because the kernels are very similar to the ones obtained by Hüsken (Hu77) in performing an unapproximated projection on 0^+. The GCM structure calculation was performed with a cut-off radius of 7.4 fm and a cut-off estimate for linear dependences of 1.D-4. We took 11 discretization points into account. The results are presented in Table 2 and compared with the experiment (As77) in Fig. 5. As can be

ℓ	0	1	2	3	4	5	6	7	8
	-20.06	-2.75		-8.55					
	-.83	4.39	-.67	5.53	2.28	7.23	4.48	11.08	13.14
	5.36	8.30	5.54	9.49	7.28	10.11	9.86	14.09	18.90
	11.52	15.09	11.08	16.46	13.13	17.52	16.38	19.44	25.73
	19.83	24.32	13.38	25.93	19.97	27.64	24.15	20.85	36.64
	31.61		18.49		28.85	40.67	34.28	30.43	50.35

Table 2: Energies in MeV with respect to the α-^{12}C threshold for the GCM structure calculation of the axial symmetric α-^{12}C configuration.

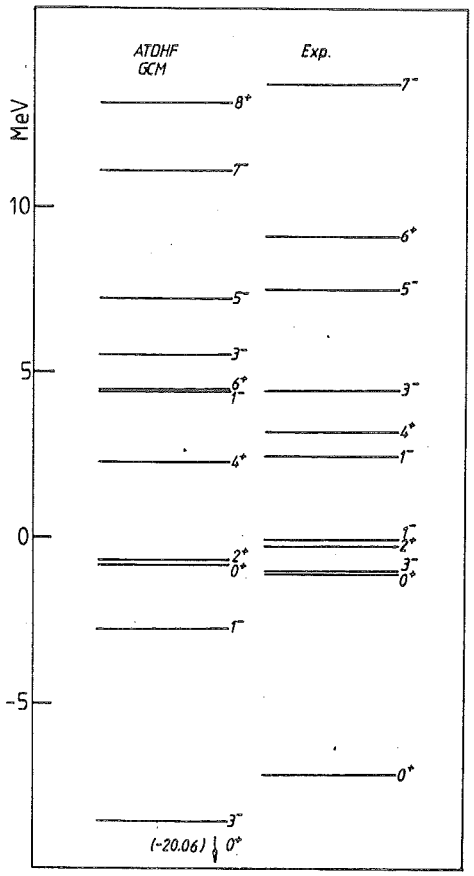

Fig. 5: Comparison between experimental levels and the calculated levels for the GCM structure calculation α-^{12}C axial configuration. The α-^{12}C threshold is taken to be the zero position. The BKN force has been used.

seen the ground state ℓ=0 is too tightly bound with respect to the α-^{12}C threshold, which, as already mentioned, is a consequence of the fact that the BKN force is not able to reproduce the binding energies of all 3 nuclei. A better value is to be expected if one projects also on vanishing total linear momentum, as shown in Table 1 where for the quantum-corrected values E_{HF}-Z_{trans} are given. Also the 3$^-$ bound state is some 7 MeV too low.

As can be seen the odd parity band has a too big moment of inertia and the even parity band with the 0$^+$ and 2$^+$ as bound states with respect to the α-^{12}C threshold does not look like a rotational band. The results of the GCM scattering calculation are presented in Fig. 6. We should note that the second

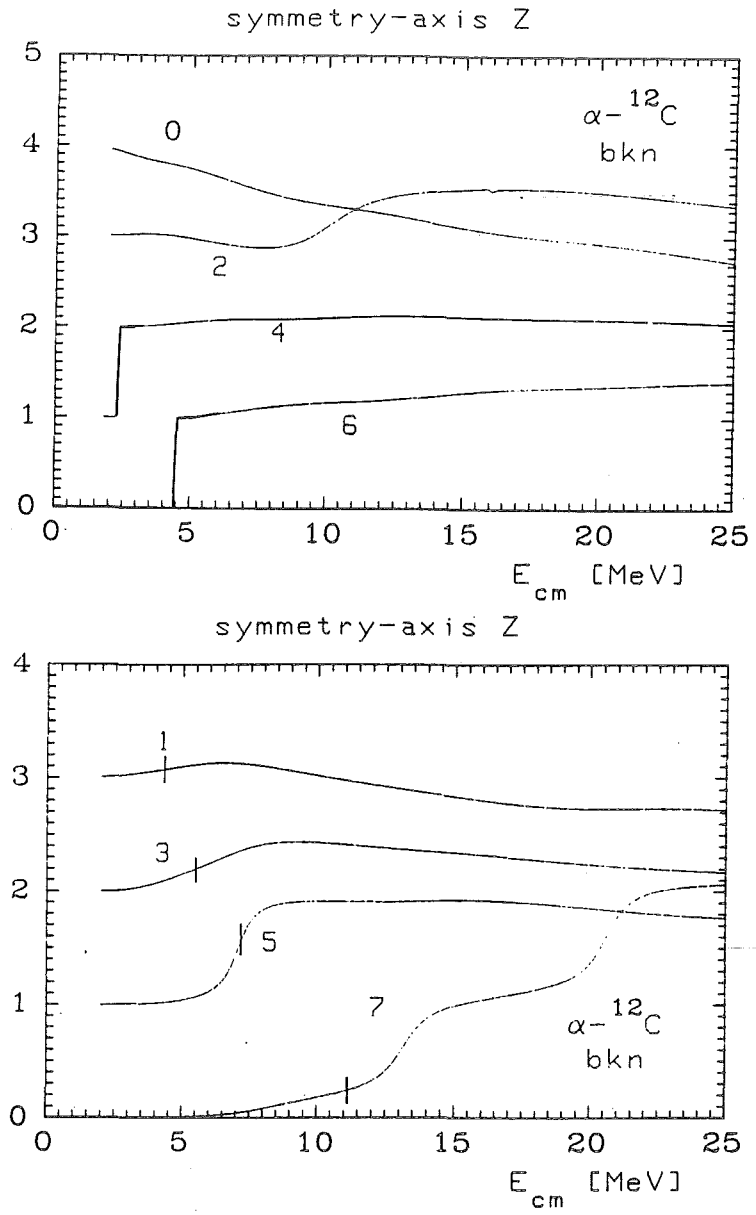

Fig. 6: qATDHF+GCM scattering phase shifts for the α-^{12}C axial configuration system. The vertical lines represent the results of the GCM structure calculation.

bump in the ℓ=7 phase shift is numerically unstable. Variation of the number of discretization points has a drastic effect on its position leaving the lower part unchanged. Also the rise inthe ℓ=2 phase shift has to be considered as spurious because the GCM calculation with imaginary energies results in an infinite width. The widths of the states are summarized in Table 3. The BKN force as well as the problem of the extension of an asymptotically well

defined angular momentum channel towards the combined system lead to much worse results than for the α-^{16}O case.

ℓ	E	Γ	E_{exp}	Γ_{exp}
4	2.45	.0005	3.19	.027
6	4.54	.005	9.13	.370
1	5.61	2.64	2.47	.510
3	6.59	1.89	4.44	.800
5	7.81	.78	7.51	.560
7	13.15	.76	13.72	.650

Table 3: Positions in MeV of the poles of the S-matrix in the α-^{12}C (axial symmetric configuration) scattering. Experimental values are taken from (AS77).

Appendix A1

Angular Momentum Projection Calculations on a Grid

A. Grid

All our calculations are performed on a 3 dimensional grid with a constant step size d in all 3 directions. The grid is constructed in such a way that it obeys the symmetries of the D_{2h}-group (El79), i.e. reflection symmetry in each direction. The importance of such a choice lies in the consequences on the operators which are constructed on the grid. A reduction of the numerical effort is the main intention. Two labelling types for the mesh-points can now be chosen according to an even or an odd number of points.

For an even number we choose ...-3/2 -1/2 1/2 3/2 ...

and for an odd number ...-2 -1 0 1 2 ...

This type of grid is especially convenient for an angular momentum projection method for wave functions represented on a grid which was proposed recently by D. Baye and P.-H. Heenen (Ba84).

B. Representations on a Grid

A wave function is represented on the grid by a column-matrix of dimension $N_x \cdot N_y \cdot N_z$ and each element is labelled by 3 numbers according to the labelling types for the 3 directions. An operator is represented by a square matrix of dimension $N_x \cdot N_y \cdot N_z$.

Since we will be interested in rotations we concentrate as an example on the orbital angular momentum operator $\hat{L}_z$. The exact relation

$$\hat{L}_z \Psi = \frac{1}{i} \left(x \frac{\partial}{\partial y} - y \frac{\partial}{\partial x} \right) \Psi \qquad \text{(in units } \hbar\text{)} \qquad \text{(P1)}$$

is transferred to a grid using an N-point Lagrange differentiation formula

$$(L_z \psi)_{\ell mn} = -i \sum_{\mu} c_\mu (\ell \psi_{\ell m+\mu n} - m \psi_{\ell+\mu mn}) \qquad \text{(P2)}$$

N odd
$c_\mu = 0 \quad \text{for } |\mu| > \frac{1}{2}(N-1)$
$c_\mu = -c_{-\mu}$

We used N=9 with the coefficients c_μ given by

$$c_1 = 4/5 \quad c_2 = -1/5 \quad c_3 = 4/105 \quad c_4 = -1/280$$

Since N_x and N_y do not change for different z-values one can define the 2 dimensional restriction of the operator $\hat{L}_z$

footnote: notation convention: $\hat{L}_z, \Psi$ "real" operators and wave functions
L_z, ψ their matrix representation on the grid

$$\boxed{(L_z)_{\ell m,\ell' m'} = -i\{\ell c_{m'-m}\delta_{\ell\ell'} - mc_{\ell'-\ell}\delta_{mm'}\}} \qquad (P3)$$

This matrix operator is hermitian and verifies following reflection symmetry relations, just as the exact operator,

$$[L_z,P] = \{L_z,P_x\} = \{L_z,P_y\} = 0 \qquad (P4)$$

because of the symmetries imposed on the grid. Note also that (P3) is independent of the chosen meshsize as it should be. Let us analyze this operator more carefully by studying its eigenvalues and eigenvectors. Indeed, it will be our aim to perform an angular momentum projection, which involves rotated wave functions: $e^{i\alpha L_z}\phi$. If we diagonalize the L_z matrix

$$g^+ L_z\, g = \ell_z$$

where ℓ_z is a diagonal matrix and g is the eigenvector matrix, the rotation matrix operator becomes

$$e^{i\alpha L_z} = g\, e^{i\alpha \ell_z}\, g^+ = \sum_i e^{i\alpha\lambda_i}\, V_i V_i^+$$

with i running over all eigenvalues λ_i and corresponding eigenvectors V_i. This will allow us to obtain a rotated wave function represented on the same grid.

C. Eigenvalues and Eigenvectors of L_z

If we divide the xy-grid space in 4 blocks according to the following figure

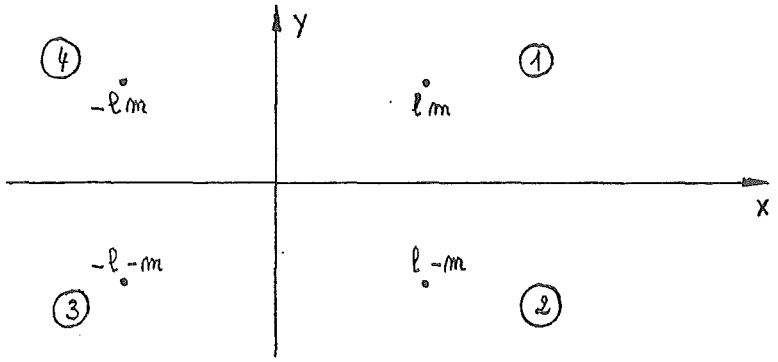

then one can write, using the relations (P4)

$$L_z = \begin{bmatrix} L_1 & L_2 & L_3 & L_4 \\ -L_2 & -L_1 & -L_4 & -L_3 \\ L_3 & L_4 & L_1 & L_2 \\ -L_4 & -L_3 & -L_2 & -L_1 \end{bmatrix} \qquad \text{(P5)}$$

where L_i combines points from the ith block with points from the first block.

Because of the definition of L_z (P3) all elements of the L_3 matrix are zero. The dimension of the submatrices is $1/4\ N_x \cdot N_y$ if N_x and N_y are even. If N_x and/or N_y are odd one has to replace N_x and/or N_y by N_x+1 and N_y+1. The invariant axis points have to be weighted in these cases by a factor $1/\sqrt{2}$ if they are common to 2 blocks and by a factor 1/2 if they are common to 4 blocks. Since L_z is hermitian and odd under time reversal λ and $-\lambda$ are simultaneous real eigenvalues of L_z with complex conjugate eigenvectors V and V*.

For a non-degenerate eigenvalue λ the corresponding eigenvector V obeys following relations, according to (P4),

$$
\begin{aligned}
PV &= \pi_1 V \\
P_x V &= \pi_2 V^* \\
P_y V &= \pi_3 V^*
\end{aligned}
$$

If we take V to be normalized then from the first relation it follows $\pi_1 = \pm 1$, and from relation 2 and 3 $|\pi_2| = |\pi_3| = +1$ because P, P_x, P_y are hermitian projection operators. Because V is defined within a phase factor one has the freedom to choose e.g. $\pi_3 = +1$. Since also $\pi_1 = \pi_2 \cdot \pi_3$ one can write $\pi_1 = \pi_2 \equiv \pi = \pm 1$. Labelling a specific eigenvector of L_z by π and another label k:

$$
\begin{aligned}
L_z V_{\pi k} &= \lambda_{\pi k} V_{\pi k} \\
P V_{\pi k} &= \pi \; V_{\pi k} \\
P_x V_{\pi k} &= \pi \; V^*_{\pi k} \\
P_y V_{\pi k} &= V^*_{\pi k}
\end{aligned}
\qquad \text{(P6)}
$$

Therefore the real and imaginary parts of V transform according to the A_π and B_π irreducible representations of the $C_s x C_i$ symmetry group (La66). We may therefore separate $V_{\pi k}$ for the different blocks

$$
V_{\pi k} = 2^{-3/2} \begin{bmatrix} v_{\pi k} \\ v^*_{\pi k} \\ \pi v_{\pi k} \\ \pi v^*_{\pi k} \end{bmatrix}
\qquad \text{(P7)}
$$

where a norm factor $2^{-3/2}$ is taken because the real and imaginary parts of $v_{\pi k}$ are separately normalized to unity. Inserting (P5) and (P7) in the equation

$$
L_z V_{\pi k} = \lambda_{\pi k} V_{\pi k}
$$

results in one independent equation only

$$L_1 v_{\pi k} + (L_2 + \pi L_4) v^*_{\pi k} = \lambda_{\pi k} v_{\pi k} \tag{P8}$$

Separation of the real and imaginary parts leads to

$$\begin{aligned} (L_1 + L_2 + \pi L_4) v^R_{\pi k} &= i\, \lambda_{\pi k} v^I_{\pi k} \\ (L_1 - L_2 - \pi L_4) v^I_{\pi k} &= -i\, \lambda_{\pi k} v^R_{\pi k} \end{aligned} \tag{P9}$$

Define

$$X_{A\pi} = L_1 + L_2 + \pi L_4 \equiv \sum_{i=1}^{4} X_{A\pi}(i) L_i$$

and

$$X_{B\pi} = L_1 - L_2 - \pi L_4 \equiv \sum_{i=1}^{4} X_{B\pi}(i) L_i$$

One has

$$X_{B\pi} = X^+_{A\pi}$$

such that following eigenvalue equation

$$\boxed{(X_{B\pi} X^+_{B\pi}) v^R_{\pi k} = \lambda^2_{\pi k} v^R_{\pi k}} \tag{P10}$$

has to be solved. For $\lambda_{\pi k} \neq 0$ the imaginary part is easily obtained from

$$\boxed{v^{I}_{\pi k} = -i \frac{1}{\lambda_{\pi k}} X_{A\pi} v^{R}_{\pi k}} \qquad \text{(P11)}$$

From (P10) and (P11) it follows that $\lambda_{\pi k}$ and $-\lambda_{\pi k}$ are eigenvalues corresponding to complex conjugate eigenvectors, as was mentioned earlier.

The $\lambda_{\pi k} = 0$ are special cases because they will turn out to be degenerate. However they can be avoided in the applications because of the existence of completeness relations.

D. Completeness Relations

Starting from the complete set $\{V_{\pi k}, V^*_{\pi k}\}$:

$$\sum_{\pi k} [V^*_{\pi k}]_i [V_{\pi k}]_j + \sum_{\pi k} [V^*_{\pi k}]^*_i [V_{\pi k}]^*_j = \delta_{ij} \qquad \text{(P12)}$$

one gets using $V_{\pi k} = R_{\pi k} + i\ I_{\pi k}$

$$2 \sum_{\pi k} \{[R_{\pi k}]_i [R_{\pi k}]_j + [I_{\pi k}]_i [I_{\pi k}]_j\} = \delta_{ij}$$

and inserting (P7)

$$\underset{===}{i=j} \quad \frac{2}{g} \sum_{\pi k} [v^R_{\pi k}]_\alpha [v^R_{\pi k}]_\alpha + [v^I_{\pi k}]_\alpha [v^I_{\pi k}]_\alpha = 1$$

where α is restricted to 1/4th of the original dimension

$\underset{===}{i\neq j}$ different possibilities occur together.

i) $$\frac{2}{g} \sum_{\pi k} [v^R_{\pi k}]_\alpha [v^R_{\pi k}]_\beta + [v^I_{\pi k}]_\alpha [v^I_{\pi k}]_\beta\} = 0 \qquad \alpha \neq \beta$$

ii) $$\frac{2}{g} \sum_{\pi k} \{[v^R_{\pi k}]_\alpha [v^R_{\pi k}]_\beta - [v^I_{\pi k}]_\alpha [v^I_{\pi k}]_\beta\} = 0 \qquad \alpha=\beta \text{ or } \alpha\neq\beta$$

iii) $$\frac{2}{g} \sum_{\pi k} \pi\{[v^R_{\pi k}]_\alpha [v^R_{\pi k}]_\beta + [v^I_{\pi k}]_\alpha [v^I_{\pi k}]_\beta\} = 0 \qquad \alpha=\beta \text{ or } \alpha\neq\beta$$

iv) $$\frac{2}{g} \sum_{\pi k} \pi\{[v^R_{\pi k}]_\alpha [v^R_{\pi k}] - [v^I_{\pi k}]_\alpha [v^I_{\pi k}]_\beta\} = 0 \qquad \alpha=\beta \text{ or } \alpha\neq\beta$$

Combining all these equations one obtains the following relations:

$$\sum_k [v^R_{\pi k}]_\alpha [v^R_{\pi k}]_\beta = \delta_{\alpha\beta} \qquad \pi=\pm 1$$

$$\sum_k [v^I_{\pi k}]_\alpha [v^I_{\pi k}]_\beta = \delta_{\alpha\beta} \qquad \pi=\pm 1 \qquad \text{(P13)}$$

E. Example

We took a $N_x = 17$, $N_y = 31$ grid. The eigenvalues for $\pi = +$ and $\pi = -$ are represented in Table 1 and 2 respectively. To every positive eigenvalue there corresponds a negative one.

pi = +

0	0	0	0	0	0	0	0	0	0	0	0
0	0	0	0	0	0	0	0	0	0	0	0
1.153	1.521	1.659	1.774	1.897	1.951	1.970	1.992	1.999	2.000	2.136	2.401
2.483	2.744	2.808	2.963	3.102	3.183	3.365	3.457	3.483	3.577	3.586	3.820
3.941	3.968	3.987	3.988	3.999	4.215	4.493	4.526	4.873	4.964	4.992	5.068
5.456	5.526	5.666	5.786	5.809	5.941	5.991	6.116	6.293	6.474	6.632	6.663
6.967	7.096	7.137	7.353	7.409	7.683	7.810	7.949	7.981	8.130	8.248	8.348
8.853	9.030	9.054	9.145	9.218	9.492	9.781	9.840	9.895	9.992	10.125	10.485
10.657	10.790	10.959	11.128	11.479	11.640	11.843	11.960	12.144	12.404	12.744	12.882
12.984	13.226	13.434	13.675	13.938	13.973	14.330	14.670	15.076	15.105	15.480	15.830
16.148	16.332	16.652	16.696	17.224	17.633	17.863	18.376	18.966	19.091	19.658	19.852
20.321	20.573	21.425	21.735	22.715	23.281	23.857	24.248	25.494	25.862	29.117	29.145

Table 1
Positive parity eigenvalues of Lz for a 17*31 grid

pi = -

0	0	0	0	0	0	0	0	0	0	0	0
0	0	0	0	0.624	0.801	0.897	0.939	0.971	0.991	0.998	1.000
1.000	1.110	1.360	1.615	1.649	1.867	2.071	2.116	2.115	2.358	2.455	2.517
2.568	2.702	2.794	2.813	2.916	2.976	2.996	3.000	3.101	3.199	3.365	3.538
3.577	3.746	4.142	4.187	4.327	4.664	4.747	4.821	4.889	4.916	4.972	4.996
5.307	5.516	5.604	5.700	5.915	6.120	6.285	6.376	6.500	6.608	6.656	6.735
6.893	6.980	7.096	7.171	7.227	7.350	7.431	8.015	8.062	8.198	8.278	8.622
8.777	8.914	8.982	9.075	9.167	9.512	9.768	9.847	10.052	10.134	10.422	10.488
10.674	10.787	10.919	11.077	11.134	11.667	11.876	11.952	12.153	12.441	12.739	12.877
12.937	13.217	13.559	13.688	13.895	13.995	14.338	14.612	15.076	15.116	15.477	15.836
16.149	16.332	16.652	16.696	17.226	17.632	17.864	18.376	18.966	19.090	19.659	19.852
20.321	20.573	21.425	21.735	22.715	23.281	23.857	24.248	25.494	25.862	29.117	29.145

Table 2
Negative parity eigenvalues of Lz for a 17*31 grid

The positive parity eigenvalues in Table 1 are an approximation to the even integer eigenvalues of $\hat{L}_z$, cf. $\hat{P}\, e^{im\varphi} = (-1)^m e^{im\varphi}$. The odd integer eigenvalues of $\hat{L}_z$ are approximated by the eigenvalues in Table 2.

Indeed it can be seen from Table 1 and 2 that there is an accumulation of eigenvalues in the neighbourhood of the even integer numbers for Table 1 and the odd integer numbers for Table 2. Some of these eigenvectors might be

interpreted as an approximation to the physical eigenfunctions of $\hat{L}_z$ restricted to one quadrant of the xy-plane. The other eigenvectors assure the completeness of the basis and have most of their norm in the outer regions.

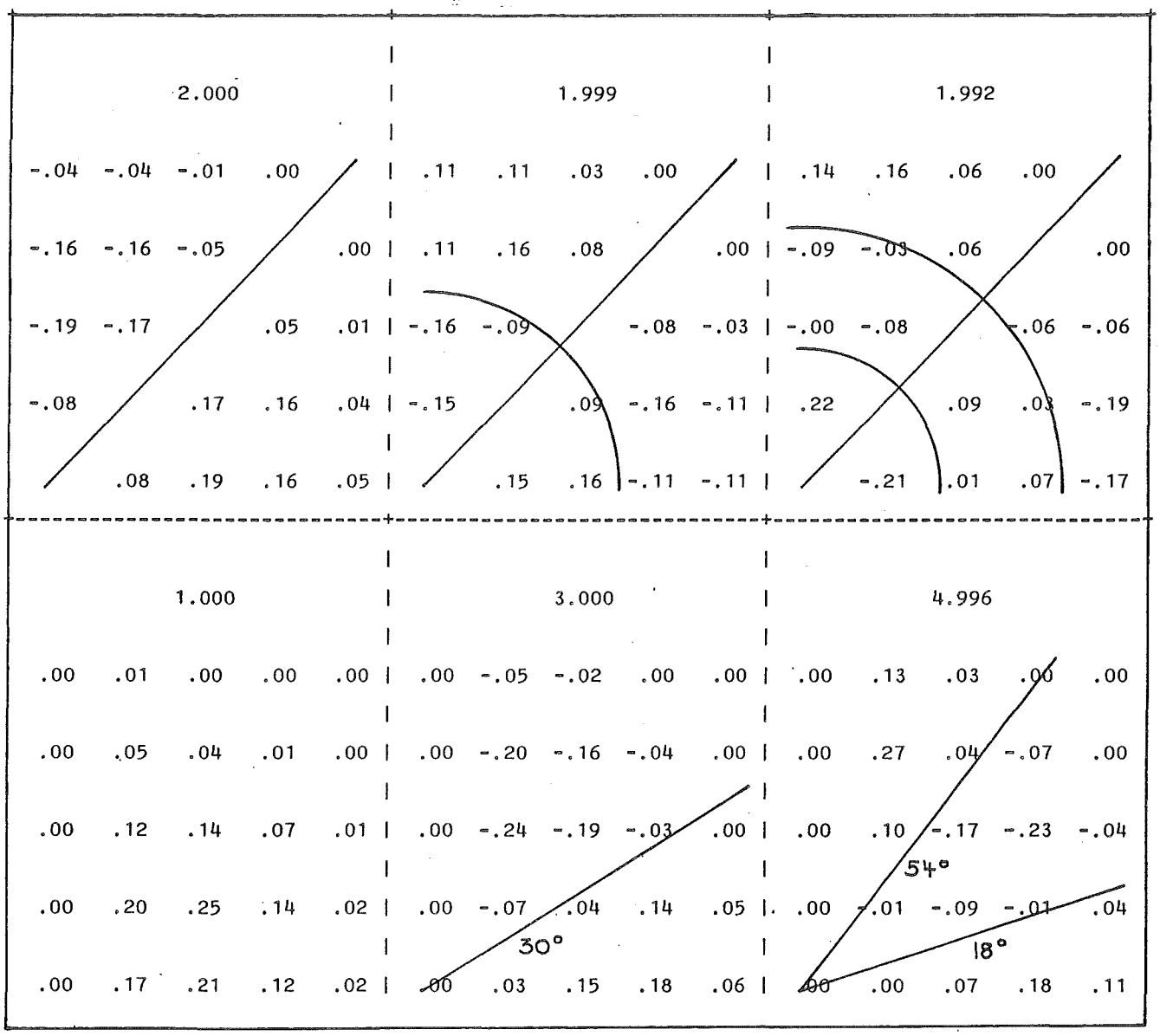

Fig. 1: Some physical eigenvectors of L_z belonging to the quoted eigenvalues, restricted to the first quadrant of the xy-plane.

Some of the physical eigenvectors, restricted to the first quadrant, are plotted in Fig. 1. The full lines represent nodal lines, which correspond to the nodal lines of the functions (Ba84)

$$\varphi_{\ell m}(r,\varphi) = (1+\delta_{m,0})^{-1/2}\, a(\tfrac{8}{\pi})^{1/2}\, [I'_m(\varepsilon_\ell^{(m)})]^{-1} I_m(\varepsilon_n^{(m)} r/a)\cos m\varphi$$

which are normalized over 1 quadrant of a circle with radius a=8. $\varepsilon_n^{(m)}$ are the zero's of the Bessel functions $I_{|m|}(x)$. These functions are eigenfunctions of $\hat{L}_z^2, \hat{P}_x, \hat{P}_y$ with eigenvalues m^2, $(-1)^m$ and +1 respectively.

Remark:

Although we started with a 17x31 grid we do not find 527 eigenvalues. We have 144x2 for π=+ and 144x2 for π=- which is 576 in total. This is due to the double counting of the points on the axes. There are 46 points (15+15+8+8) which were counted twice and the origin was 4 times taken into account. Therefore from the 576 eigenvalues one has to subtract 49 (46+3) which is just 527. These spurious eigenvalues have to be zero's since they come from linear dependences in the original L_z matrix.

F. Rotations

We concentrate e.g. on rotations around the z-axis. The rotation operator $\hat{R}_z(\alpha) = e^{i\alpha\hat{L}_z}$ for a rotation around the z-axis with an angle α is replaced by the matrix operator

$$R_z(\alpha) = e^{i\alpha L_z} \tag{P14}$$

on the grid.

It will be important to reduce as much as possible the dimension of this matrix to save calculation time. Therefore we want to rotate and project on the irreducible representations of $C_s \times C_i$ at the same time.

We therefore develop the wave function in the L_z eigenbasis

$$\psi_{\ell m n_o} = \sum_{\pi k} c_{\pi k} (V_{\pi k})_{\ell m} + \sum_{\pi k} d_{\pi k} (V^*_{\pi k})_{\ell m} \tag{P15}$$

with

$$\begin{aligned} c_{\pi k} &= V^+_{\pi k}\ \psi \\ d_{\pi k} &= V^T_{\pi k}\ \psi \end{aligned} \tag{P16}$$

and calculate:

$$R_z(\alpha, IR1 \to IR2)\psi = \frac{1}{4}\,(1+\chi_{IR2}(P_y)P_y+\chi_{IR2}(P_x)P_x+\chi_{IR2}(P)P)e^{i\alpha L_z}$$
$$\cdot\ \frac{1}{4}\,(1+\chi_{IR1}(P_y)P_y+\chi_{IR1}(P_x)P_x+\chi_{IR1}(P)P)\psi \qquad (P17)$$

Inserting (P6), (P15), (P16) results in

$$R_z(\alpha, IR1 \to IR2) = \delta_{\chi_{IR1}(P),\pi} \times \delta_{\chi_{IR2}(P),\pi} \times \frac{1}{4}$$
$$\sum_k e^{i\alpha\lambda_{\pi k}}\ \{V_{\pi k}V_{\pi k}^{+}+\chi_{IR1}(P_y)V_{\pi k}V_{\pi k}^{T}+\chi_{IR2}(P_y)V_{\pi k}^{*}V_{\pi k}^{+} \qquad (P18)$$
$$+\ \chi_{IR1}(P_y)\chi_{IR2}(P_y)V_{\pi k}^{*}V_{\pi k}^{T}\} + \text{complex conjugate.}$$

The characters of the different irreducible representations are listed in Table 3 (La66).

$C_s x C_i$	E	P_y	P_x	P
A_g	1	1	1	1
A_u	1	1	-1	-1
B_g	1	-1	-1	1
B_u	1	-1	1	-1

Table 3

Write again

$$V_{\pi k} = R_{\pi k} + i\ I_{\pi k} \qquad (P19)$$

then (P18) becomes for the different possibilities

$$
\begin{aligned}
R_z(\alpha, A_\pi \to A_\pi) &= 2 \sum_k \cos\alpha\lambda_{\pi k} R_{\pi k} R^T_{\pi k} \\
R_z(\alpha, A_\pi \to B_\pi) &= -2 \sum_k \sin\alpha\lambda_{\pi k} I_{\pi k} R^T_{\pi k} \\
R_z(\alpha, B_\pi \to A_\pi) &= -R^T_z(\alpha, A_\pi \to B_\pi) \\
R_z(\alpha, B_\pi \to B_\pi) &= 2 \sum_k \cos\alpha\lambda_{\pi k} I_{\pi k} I^T_{\pi k}
\end{aligned}
\qquad \text{(P20)}
$$

However because of the projections it is possible to make a study of the rotation of the first quadrant only. Therefore (P20) is reduced to smaller dimensions, using the notation of (P7)

$$
\begin{aligned}
R^1_z(\alpha, A_\pi \to A_\pi) &= \sum_k \cos\alpha\lambda_{\pi k} \, v^R_{\pi k} v^{R^T}_{\pi k} \\
R^1_z(\alpha, A_\pi \to B_\pi) &= -\sum_k \sin\alpha\lambda_{\pi k} \, v^I_{\pi k} v^{R^T}_{\pi k} \\
R^1_z(\alpha, B_\pi \to A_\pi) &= \sum_k \sin\alpha\lambda_{\pi k} \, v^R_{\pi k} v^{I^T}_{\pi k} = -R^1_z(\alpha, A_\pi \to B_\pi)^T \\
R^1_z(\alpha, B_\pi \to B_\pi) &= \sum_k \cos\alpha\lambda_{\pi k} \, v^I_{\pi k} v^{I^T}_{\pi k}
\end{aligned}
$$

where the upper index 1 shows the reduction to the first quadrant. Making use of the completeness relations (P13) we get the final forms:

$$
\begin{aligned}
R^1_z(\alpha, A_\pi \to A_\pi)_{ij} &= \delta_{ij} + \sum_k (\cos\alpha\lambda_{\pi k} - 1)[v^R_{\pi k}]_i [v^R_{\pi k}]_j \\
R^1_z(\alpha, A_\pi \to B_\pi)_{ij} &= - \sum_k \sin\alpha\lambda_{\pi k} [v^I_{\pi k}]_i [v^R_{\pi k}]_j \\
R^1_z(\alpha, B_\pi \to A_\pi)_{ij} &= + \sum_k \sin\alpha\lambda_{\pi k} [v^R_{\pi k}]_i [v^I_{\pi k}]_j = -R^1_z(\alpha, A_\pi \to B_\pi)_{ji} \\
R^1_z(\alpha, B_\pi \to B_\pi)_{ij} &= \delta_{ij} + \sum_k (\cos\alpha\lambda_{\pi k} - 1)[v^I_{\pi k}]_i [v^I_{\pi k}]_j
\end{aligned}
\qquad \text{(P21)}
$$

from which it is clear that the eigenvectors belonging to the zero eigenvalues are no longer needed.

For 3 dimensional rotations the same procedure is extended to 3 2-dimensional rotations around the z, y and again z axes. One additionally has to take care of the sum over the different possible irreducible representations after each rotation.

G. Example

Rotation of a $p_x s_y$-wave function around the z-axis. Again we take $N_x = 31$, $N_y = 17$

$$\psi(x,y) = x \exp -\frac{1}{2}\left\{\frac{x^2}{b_x^2} + \frac{y^2}{b_y^2}\right\} \tag{P22}$$

Analytic rotation around an angle α

$$R_z(\alpha)\psi(x,y) = \psi(x',y')$$

$$\text{with} \quad y' = y\cos\alpha - x\sin\alpha \tag{P23}$$

$$x' = x\cos\alpha - y\sin\alpha$$

and projection on A_u (or B_u) after rotation should be compared with multiplication of one of the matrices (P21) with the grid representation of the wave function (P22).

Two cases were studied: $b_x = 4$ $b_y = 2$ and $b_x = 3$ $b_y = 2$ for different angles $\alpha = \pi/8, \pi/4, \pi/2$ and summarized in Tables 4 and 5 for the first quadrant of the xy-plane. From Table 4 one sees that the absolute error increases from .01 for $\alpha = \pi/8$, .04 for $\alpha = \pi/4$ to .12 for $\alpha = \pi/2$. The reason for the increasing error is due to the asymmetry of the grid and the big b_x-value which makes it impossible to locate the rotated wave function on the grid. The results in Table 5 for $b_x = 3$ $b_y = 2$ show the improvement: .01 absolute error for $\alpha = \pi/8, \pi/4$ and $\pi/2$ increasing to .03 for $\alpha=\pi$.

In Table 6 we compare the results for $b_x = 3$ $b_y = 2$ with $b_x = 3$ $b_y = 1$ for $\alpha=\pi$. The error increases now from .03 to .07 which shows that for very narrow

Table 4

$A_u \rightarrow A_u$

$b_x = 4 \qquad b_y = 2$

$\alpha = 0$

0.00	0.89	1.25	1.60	1.72	1.62	1.38	1.07	0.77	0.51	0.31	0.18	0.09	0.05	0.02	0.01
0.00	0.86	1.56	2.00	2.14	2.02	1.72	1.34	0.96	0.63	0.39	0.22	0.12	0.06	0.03	0.01
0.00	0.59	1.07	1.37	1.47	1.39	1.18	0.92	0.66	0.43	0.27	0.15	0.08	0.04	0.02	0.01
0.00	0.31	0.57	0.74	0.79	0.74	0.63	0.49	0.35	0.23	0.14	0.08	0.04	0.02	0.01	0.00
0.00	0.13	0.24	0.31	0.33	0.31	0.26	0.20	0.15	0.10	0.06	0.03	0.02	0.01	0.00	0.00
0.00	0.04	0.08	0.10	0.11	0.10	0.09	0.07	0.05	0.03	0.02	0.01	0.01	0.00	0.00	0.00
0.00	0.01	0.02	0.03	0.03	0.03	0.02	0.02	0.01	0.01	0.00	0.00	0.00	0.00	0.00	0.00
0.00	0.00	0.00	0.00	0.01	0.01	0.00	0.00	0.00	0.00	0.00	0.00	0.00	0.00	0.00	0.00
0.00	0.00	0.00	0.00	0.00	0.00	0.00	0.00	0.00	0.00	0.00	0.00	0.00	0.00	0.00	0.00

$\alpha = \pi \div 8$

matrix method															
0.00	0.62	1.09	1.31	1.27	1.06	0.78	0.50	0.29	0.15	0.07	0.03	0.01	0.00	0.00	0.00
-0.00	0.81	1.43	1.73	1.71	1.45	1.09	0.73	0.44	0.24	0.12	0.05	0.02	0.01	0.00	0.00
0.00	0.63	1.13	1.41	1.45	1.29	1.02	0.73	0.47	0.27	0.14	0.07	0.03	0.01	0.00	0.00
-0.00	0.41	0.76	0.98	1.06	1.01	0.85	0.65	0.45	0.28	0.16	0.08	0.04	0.02	0.01	0.00
0.00	0.22	0.42	0.57	0.65	0.66	0.59	0.48	0.36	0.24	0.14	0.08	0.04	0.02	0.01	0.00
-0.00	0.10	0.19	0.27	0.33	0.35	0.34	0.29	0.23	0.16	0.11	0.06	0.03	0.02	0.01	0.00
-0.00	0.03	0.07	0.10	0.13	0.15	0.16	0.14	0.12	0.09	0.06	0.04	0.02	0.01	0.00	0.00
-0.00	0.01	0.02	0.03	0.04	0.05	0.06	0.05	0.05	0.04	0.03	0.02	0.01	0.01	0.00	0.00
0.00	0.00	0.00	0.01	0.01	0.02	0.02	0.02	0.02	0.02	0.01	0.01	0.01	0.00	0.00	-0.00
analytic															
0.00	0.62	1.09	1.31	1.27	1.06	0.78	0.50	0.29	0.15	0.07	0.03	0.01	0.00	0.00	0.00
0.00	0.81	1.43	1.73	1.71	1.45	1.09	0.73	0.44	0.24	0.12	0.05	0.02	0.01	0.00	0.00
0.00	0.63	1.13	1.41	1.45	1.29	1.02	0.73	0.47	0.27	0.14	0.07	0.03	0.01	0.00	0.00
0.00	0.41	0.76	0.98	1.06	1.01	0.85	0.65	0.45	0.28	0.16	0.08	0.04	0.02	0.01	0.00
0.00	0.22	0.42	0.57	0.65	0.66	0.59	0.48	0.36	0.24	0.14	0.08	0.04	0.02	0.01	0.00
0.00	0.10	0.19	0.27	0.33	0.35	0.34	0.29	0.23	0.16	0.11	0.06	0.03	0.02	0.01	0.00
0.00	0.03	0.07	0.10	0.13	0.15	0.15	0.14	0.12	0.09	0.06	0.04	0.02	0.01	0.00	0.00
0.00	0.01	0.02	0.03	0.04	0.05	0.06	0.06	0.05	0.04	0.03	0.02	0.01	0.01	0.00	0.00
0.00	0.00	0.00	0.01	0.01	0.01	0.02	0.02	0.02	0.01	0.01	0.01	0.01	0.00	0.00	-0.00

$\alpha = \pi \div 4$

matrix method

0.00	0.46	0.73	0.74	0.57	0.35	0.18	0.08	0.03	0.01	0.01	0.00	0.00	0.00	-0.00	0.00
-0.00	0.66	1.06	1.10	0.87	0.56	0.29	0.13	0.04	0.01	-0.00	-0.00	-0.00	-0.00	0.00	-0.00
0.00	0.67	1.10	1.20	1.01	0.70	0.41	0.20	0.09	0.04	0.01	0.01	0.00	0.00	-0.00	0.00
-0.00	0.61	1.05	1.21	1.10	0.82	0.51	0.27	0.11	0.04	0.01	-0.00	-0.00	-0.00	0.00	0.00
0.00	0.49	0.87	1.07	1.04	0.85	0.59	0.35	0.18	0.08	0.03	0.01	0.00	0.00	-0.00	0.00
-0.00	0.33	0.61	0.79	0.83	0.73	0.54	0.33	0.17	0.07	0.02	0.01	0.00	0.00	0.00	0.00
-0.00	0.19	0.37	0.51	0.59	0.57	0.47	0.33	0.20	0.11	0.05	0.02	0.01	0.00	0.00	0.00
-0.00	0.09	0.18	0.26	0.31	0.32	0.28	0.20	0.12	0.06	0.03	0.01	0.00	0.00	0.00	0.00
0.00	0.04	0.09	0.14	0.19	0.22	0.22	0.19	0.13	0.08	0.04	0.02	0.01	0.00	0.00	0.00

analytic

0.00	0.46	0.73	0.74	0.57	0.35	0.18	0.08	0.03	0.01	0.01	0.00	0.00	0.00	0.00	0.00
0.00	0.66	1.06	1.10	0.87	0.56	0.30	0.13	0.05	0.02	0.00	0.00	0.00	0.00	0.00	0.00
0.00	0.67	1.10	1.20	1.01	0.70	0.40	0.20	0.08	0.03	0.01	0.00	0.00	0.00	0.00	0.00
0.00	0.61	1.05	1.21	1.10	0.82	0.52	0.27	0.12	0.05	0.02	0.00	0.00	0.00	0.00	0.00
0.00	0.49	0.87	1.07	1.04	0.85	0.58	0.34	0.16	0.07	0.02	0.01	0.00	0.00	0.00	0.00
0.00	0.33	0.61	0.80	0.84	0.74	0.55	0.35	0.19	0.09	0.03	0.01	0.00	0.00	0.00	0.00
0.00	0.19	0.36	0.51	0.58	0.55	0.45	0.31	0.18	0.09	0.04	0.01	0.00	0.00	0.00	0.00
0.00	0.09	0.18	0.27	0.33	0.35	0.31	0.23	0.15	0.08	0.04	0.01	0.00	0.00	0.00	0.00
0.00	0.03	0.08	0.12	0.16	0.19	0.18	0.15	0.10	0.06	0.03	0.01	0.01	0.00	0.00	0.00

$\alpha = \pi \div 2$

matrix method

0.00	0.00	0.02	0.06	0.09	0.08	0.03	0.00	0.00	0.00	0.00	0.00	-0.00	0.00	0.00	0.00
-0.00	-0.01	-0.03	-0.09	-0.12	-0.10	-0.04	-0.01	-0.00	-0.00	-0.00	0.00	-0.00	0.00	0.00	0.00
0.00	0.02	0.06	0.09	0.09	0.07	0.05	0.02	0.00	-0.00	0.00	-0.00	0.00	0.00	0.00	0.00
-0.00	-0.04	-0.09	-0.10	-0.07	-0.05	-0.05	-0.03	-0.01	0.00	-0.00	-0.00	0.00	0.00	0.00	0.00
-0.00	0.09	0.12	0.09	0.04	0.03	0.04	0.04	0.02	0.00	-0.00	0.00	0.00	0.01	0.01	0.00
-0.00	-0.10	-0.12	-0.08	-0.04	-0.02	-0.02	-0.03	-0.03	-0.01	0.00	0.00	0.01	0.01	0.01	0.00
-0.00	0.11	0.12	0.07	0.03	0.01	0.02	0.02	0.03	0.02	0.00	0.00	0.01	0.01	0.00	0.00
-0.00	-0.07	-0.09	-0.07	-0.03	-0.01	-0.00	-0.01	-0.02	-0.02	0.00	0.02	0.02	0.01	0.00	-0.00
0.00	0.03	0.05	0.06	0.04	0.02	0.01	0.01	0.02	0.03	0.03	0.02	0.01	0.00	-0.00	0.00

analytic values for $\alpha = \pi \div 2$
are all zero

Table 5

$A_u \rightarrow A_u$

$b_x = 3 \qquad b_y = 2$

$\alpha = 0$

0.00	0.67	1.13	1.29	1.16	0.88	0.57	0.33	0.16	0.07	0.03	0.01	0.00	0.00	0.00	0.00
0.00	0.83	1.41	1.61	1.45	1.10	0.72	0.41	0.20	0.09	0.03	0.01	0.00	0.00	0.00	0.00
0.00	0.57	0.97	1.10	1.00	0.76	0.49	0.28	0.14	0.06	0.02	0.01	0.00	0.00	0.00	0.00
0.00	0.31	0.52	0.59	0.53	0.40	0.26	0.15	0.07	0.03	0.01	0.00	0.00	0.00	0.00	0.00
0.00	0.13	0.22	0.25	0.22	0.17	0.11	0.06	0.03	0.01	0.01	0.00	0.00	0.00	0.00	0.00
0.00	0.04	0.07	0.08	0.07	0.05	0.04	0.02	0.01	0.00	0.00	0.00	0.00	0.00	0.00	0.00
0.00	0.01	0.02	0.02	0.02	0.01	0.01	0.01	0.00	0.00	0.00	0.00	0.00	0.00	0.00	0.00
0.00	0.00	0.00	0.00	0.00	0.00	0.00	0.00	0.00	0.00	0.00	0.00	0.00	0.00	0.00	0.00
0.00	0.00	0.00	0.00	0.00	0.00	0.00	0.00	0.00	0.00	0.00	0.00	0.00	0.00	0.00	0.00

$\alpha = \pi \div 8$

							matrix method								
0.00	0.61	1.00	1.09	0.91	0.63	0.37	0.18	0.08	0.03	0.01	0.00	0.00	0.00	0.00	0.00
-0.00	0.79	1.30	1.41	1.20	0.84	0.49	0.25	0.11	0.04	0.01	0.00	0.00	0.00	0.00	0.00
0.00	0.59	0.99	1.09	0.95	0.68	0.42	0.22	0.10	0.04	0.01	0.00	0.00	0.00	0.00	0.00
-0.00	0.37	0.62	0.70	0.63	0.47	0.30	0.17	0.08	0.03	0.01	0.00	0.00	0.00	0.00	0.00
0.00	0.19	0.32	0.37	0.35	0.27	0.18	0.10	0.05	0.02	0.01	0.00	0.00	0.00	0.00	0.00
-0.00	0.08	0.13	0.16	0.16	0.13	0.09	0.05	0.03	0.01	0.01	0.00	0.00	0.00	0.00	0.00
-0.00	0.02	0.04	0.06	0.06	0.05	0.04	0.02	0.01	0.01	0.00	0.00	0.00	0.00	0.00	0.00
-0.00	0.01	0.01	0.02	0.02	0.01	0.01	0.01	0.00	0.00	0.00	0.00	0.00	0.00	0.00	0.00
0.00	0.00	0.00	0.00	0.00	0.00	0.00	0.00	0.00	0.00	0.00	0.00	0.00	0.00	0.00	0.00
							analytic								
0.00	0.61	1.00	1.08	0.91	0.63	0.37	0.18	0.08	0.03	0.01	0.00	0.00	0.00	0.00	0.00
0.00	0.79	1.30	1.41	1.20	0.84	0.49	0.25	0.11	0.04	0.01	0.00	0.00	0.00	0.00	0.00
0.00	0.59	0.99	1.09	0.95	0.68	0.42	0.22	0.10	0.04	0.01	0.00	0.00	0.00	0.00	0.00
0.00	0.37	0.62	0.70	0.63	0.47	0.30	0.17	0.08	0.03	0.01	0.00	0.00	0.00	0.00	0.00
0.00	0.19	0.32	0.37	0.35	0.27	0.18	0.10	0.05	0.02	0.01	0.00	0.00	0.00	0.00	0.00
0.00	0.08	0.13	0.16	0.15	0.13	0.09	0.05	0.03	0.01	0.01	0.00	0.00	0.00	0.00	0.00
0.00	0.02	0.04	0.06	0.06	0.05	0.04	0.02	0.01	0.01	0.00	0.00	0.00	0.00	0.00	0.00
0.00	0.01	0.01	0.02	0.02	0.01	0.01	0.01	0.00	0.00	0.00	0.00	0.00	0.00	0.00	0.00
0.00	0.00	0.00	0.00	0.00	0.00	0.00	0.00	0.00	0.00	0.00	0.00	0.00	0.00	0.00	0.00

$\alpha = \pi \div 4$

matrix method

0.00	0.46	0.70	0.67	0.47	0.26	0.12	0.04	0.01	0.00	0.00	0.00	0.00	0.00	-0.00	0.00
-0.00	0.63	0.97	0.94	0.68	0.38	0.17	0.06	0.02	0.00	0.00	0.00	0.00	0.00	0.00	-0.00
0.00	0.58	0.91	0.90	0.68	0.40	0.19	0.08	0.02	0.01	0.00	0.00	0.00	0.00	0.00	0.00
-0.00	0.47	0.76	0.78	0.61	0.38	0.20	0.08	0.03	0.01	0.00	0.00	0.00	0.00	0.00	0.00
0.00	0.33	0.54	0.58	0.48	0.32	0.17	0.08	0.03	0.01	0.00	0.00	0.00	0.00	0.00	0.00
-0.00	0.19	0.32	0.36	0.31	0.22	0.13	0.06	0.02	0.01	0.00	0.00	0.00	0.00	0.00	0.00
-0.00	0.09	0.16	0.19	0.17	0.13	0.08	0.04	0.02	0.01	0.00	0.00	0.00	0.00	0.00	0.00
-0.00	0.04	0.06	0.08	0.07	0.06	0.04	0.02	0.01	0.00	0.00	0.00	0.00	0.00	0.00	0.00
0.00	0.01	0.02	0.03	0.03	0.03	0.02	0.01	0.01	0.00	0.00	0.00	0.00	0.00	0.00	0.00

analytic

0.00	0.46	0.70	0.67	0.47	0.26	0.12	0.04	0.01	0.00	0.00	0.00	0.00	0.00	-0.00	0.00
0.00	0.63	0.97	0.94	0.68	0.38	0.17	0.06	0.02	0.00	0.00	0.00	0.00	0.00	0.00	-0.00
0.00	0.58	0.91	0.90	0.67	0.40	0.19	0.08	0.02	0.01	0.00	0.00	0.00	0.00	0.00	0.00
0.00	0.47	0.76	0.78	0.61	0.38	0.20	0.08	0.03	0.01	0.00	0.00	0.00	0.00	0.00	0.00
0.00	0.33	0.54	0.58	0.48	0.32	0.17	0.08	0.03	0.01	0.00	0.00	0.00	0.00	0.00	0.00
0.00	0.19	0.32	0.36	0.31	0.22	0.13	0.06	0.02	0.01	0.00	0.00	0.00	0.00	0.00	0.00
0.00	0.09	0.16	0.19	0.17	0.13	0.08	0.04	0.02	0.01	0.00	0.00	0.00	0.00	0.00	0.00
0.00	0.04	0.06	0.08	0.08	0.06	0.04	0.02	0.01	0.00	0.00	0.00	0.00	0.00	0.00	0.00
0.00	0.01	0.02	0.03	0.03	0.02	0.02	0.01	0.00	0.00	0.00	0.00	0.00	0.00	0.00	0.00

$\alpha = \pi \div 2$

matrix method

0.00	0.00	0.00	0.00	0.00	0.00	0.00	0.00	-0.00	-0.00	0.00	0.00	-0.00	0.00	0.00	0.00
-0.00	0.00	-0.00	-0.01	-0.01	-0.00	-0.00	-0.00	-0.00	-0.00	0.00	0.00	0.00	0.00	0.00	0.00
0.00	0.00	0.01	0.00	0.00	0.00	0.00	0.00	-0.00	0.00	0.00	0.00	0.00	0.00	0.00	0.00
-0.00	-0.00	-0.01	-0.01	-0.00	-0.00	-0.00	-0.00	-0.00	-0.00	-0.00	0.00	0.00	0.00	0.00	0.00
-0.00	0.01	0.01	0.00	0.00	0.00	0.00	0.00	0.00	0.00	0.00	0.00	0.00	0.00	0.00	0.00
-0.00	-0.01	-0.01	-0.01	-0.00	-0.00	-0.00	-0.00	-0.00	-0.00	0.00	0.00	0.00	0.00	0.00	0.00
-0.00	0.01	0.01	0.01	0.00	0.00	0.00	0.00	0.00	0.00	0.00	0.00	0.00	0.00	0.00	-0.00
-0.00	-0.01	-0.01	-0.01	-0.00	-0.00	0.00	-0.00	-0.00	-0.00	0.00	0.00	0.00	0.00	-0.00	-0.00
0.00	0.00	0.01	0.01	0.01	0.00	0.00	0.00	0.00	0.00	0.00	0.00	0.00	-0.00	-0.00	0.00

analytic values for $\alpha = \pi \div 2$
are all zero

Table 6

$A_u \rightarrow A_u$

$b_x = 3 \quad b_y = 1$

$\alpha = 0$

0.00	0.67	1.13	1.29	1.16	0.88	0.57	0.33	0.16	0.07	0.03	0.01	0.00	0.00	0.00	0.00
0.00	0.83	1.41	1.61	1.45	1.10	0.72	0.41	0.20	0.09	0.03	0.01	0.00	0.00	0.00	0.00
0.00	0.57	0.97	1.10	1.00	0.76	0.49	0.28	0.14	0.06	0.02	0.01	0.00	0.00	0.00	0.00
0.00	0.31	0.52	0.59	0.53	0.40	0.26	0.15	0.07	0.03	0.01	0.00	0.00	0.00	0.00	0.00
0.00	0.13	0.22	0.25	0.22	0.17	0.11	0.06	0.03	0.01	0.01	0.00	0.00	0.00	0.00	0.00
0.00	0.04	0.07	0.08	0.07	0.05	0.04	0.02	0.01	0.00	0.00	0.00	0.00	0.00	0.00	0.00
0.00	0.01	0.02	0.02	0.02	0.01	0.01	0.01	0.00	0.00	0.00	0.00	0.00	0.00	0.00	0.00
0.00	0.00	0.00	0.00	0.00	0.00	0.00	0.00	0.00	0.00	0.00	0.00	0.00	0.00	0.00	0.00
0.00	0.00	0.00	0.00	0.00	0.00	0.00	0.00	0.00	0.00	0.00	0.00	0.00	0.00	0.00	0.00

$\alpha = \pi$

matrix method

0.00	-0.66	-1.14	-1.28	-1.16	-0.88	-0.57	-0.33	-0.16	-0.07	-0.01	0.01	0.00	-0.00	-0.00	-0.00
-0.00	-0.84	-1.42	-1.60	-1.45	-1.10	-0.71	-0.41	-0.21	-0.08	-0.01	0.01	0.00	-0.00	-0.00	0.00
0.00	-0.58	-0.96	-1.11	-1.00	-0.76	-0.49	-0.28	-0.14	-0.06	-0.01	0.01	0.00	-0.00	0.00	-0.00
-0.00	-0.31	-0.51	-0.60	-0.53	-0.41	-0.26	-0.15	-0.08	-0.03	-0.00	0.01	0.00	-0.00	-0.00	0.00
-0.00	-0.13	-0.22	-0.25	-0.21	-0.17	-0.11	-0.06	-0.04	-0.01	0.00	0.00	0.00	-0.00	0.00	-0.00
-0.00	-0.04	-0.07	-0.07	-0.08	-0.06	-0.03	-0.02	-0.02	-0.00	0.00	0.00	-0.00	0.00	-0.00	0.00
-0.00	-0.01	-0.02	-0.02	-0.03	-0.01	-0.01	-0.01	-0.01	0.00	0.00	0.00	0.00	-0.00	0.00	-0.00
-0.00	-0.00	-0.00	-0.00	-0.00	0.00	-0.01	-0.01	-0.00	0.00	-0.00	0.00	-0.00	0.00	-0.00	0.00
0.00	-0.00	-0.00	-0.00	-0.00	-0.00	-0.00	0.00	0.00	0.00	0.00	-0.00	0.00	-0.00	0.00	-0.00

the analytic values are
-1 * the input values

$b_x = 3 \quad b_y = 2$

$\alpha = 0$

0.00	0.67	1.13	1.29	1.16	0.88	0.57	0.33	0.16	0.07	0.03	0.01	0.00	0.00	0.00	0.00
0.00	0.57	0.97	1.10	1.00	0.76	0.49	0.28	0.14	0.06	0.02	0.01	0.00	0.00	0.00	0.00
0.00	0.13	0.22	0.25	0.22	0.17	0.11	0.06	0.03	0.01	0.01	0.00	0.00	0.00	0.00	0.00
0.00	0.01	0.02	0.02	0.02	0.01	0.01	0.01	0.00	0.00	0.00	0.00	0.00	0.00	0.00	0.00
0.00	0.00	0.00	0.00	0.00	0.00	0.00	0.00	0.00	0.00	0.00	0.00	0.00	0.00	0.00	0.00
0.00	0.00	0.00	0.00	0.00	0.00	0.00	0.00	0.00	0.00	0.00	0.00	0.00	0.00	0.00	0.00
0.00	0.00	0.00	0.00	0.00	0.00	0.00	0.00	0.00	0.00	0.00	0.00	0.00	0.00	0.00	0.00
0.00	0.00	0.00	0.00	0.00	0.00	0.00	0.00	0.00	0.00	0.00	0.00	0.00	0.00	0.00	0.00
0.00	0.00	0.00	0.00	0.00	0.00	0.00	0.00	0.00	0.00	0.00	0.00	0.00	0.00	0.00	0.00

$\alpha = \pi$

matrix method

0.00	-0.64	-1.06	-1.18	-1.05	-0.81	-0.50	-0.30	-0.16	-0.05	-0.00	-0.00	-0.00	0.01	-0.01	0.00
-0.00	-0.62	-1.03	-1.19	-1.07	-0.81	-0.55	-0.30	-0.14	-0.06	-0.01	0.01	0.00	-0.01	0.01	-0.01
0.00	-0.12	-0.23	-0.29	-0.29	-0.21	-0.13	-0.07	-0.06	-0.01	0.01	-0.00	-0.00	0.01	-0.01	0.01
-0.00	0.04	0.05	0.06	0.09	0.03	0.04	0.02	0.02	-0.00	-0.01	0.01	0.00	-0.01	0.01	-0.00
0.00	-0.05	-0.05	-0.04	-0.01	-0.00	-0.00	0.01	-0.01	-0.01	0.01	-0.00	-0.00	0.01	-0.01	0.00
-0.00	-0.01	-0.03	-0.01	-0.05	-0.05	-0.04	-0.00	-0.02	0.01	-0.01	0.01	0.00	-0.00	0.00	-0.00
-0.00	0.07	0.07	0.03	0.02	0.02	0.04	-0.01	0.01	0.00	0.00	0.00	-0.00	0.00	-0.00	0.00
-0.00	-0.05	-0.04	-0.02	0.01	0.02	-0.01	-0.00	0.02	-0.01	-0.00	0.00	0.00	-0.00	0.00	-0.00
0.00	0.00	-0.01	-0.01	-0.03	-0.01	-0.01	0.02	-0.00	-0.00	0.01	-0.00	-0.00	0.00	-0.00	0.00

the analytic values are
-1 * the input values

wave functions the matrix method will get worse. For the $A_u \rightarrow B_u$ case with $b_x = 3$ $b_y = 2$ the error is .01 for $\alpha=\pi/8$ and $\alpha=\pi/4$ and increases to .03 for $\alpha=\pi/2$.

Since rotations over π can be done exactly on the grid the largest rotation angle which should be considered is $\pi/2$ since

$$R_z(\tfrac{\pi}{2} + \alpha) = R_z(\pi) \times R_z(\alpha - \tfrac{\pi}{2}) \qquad \text{(P24)}$$

Let us now consider the norms, with ψ from (P22),

$$\langle \tfrac{1}{2}(1+P_y)R_z(n\pi)\psi | \tfrac{1}{2}(1+P_y)R_z(n\pi)\psi \rangle$$

and

$$\langle \psi | \tfrac{1}{2}(1+P_y)R_z(n\pi)\psi \rangle$$

The analytic value is +1, however due to the small admixtures of the B_u components in the wave function using the matrix method this exact value will not be obtained. The $b_x = 3$ $b_y = 2$ case is listed in Table 7.

$\alpha = n\times\pi$	$\langle \psi \mid R_z(\alpha, A_u \rightarrow A_u)\psi \rangle$	$\langle R_z(\alpha, A_u \rightarrow A_u)\psi \mid R_z(\alpha, A_u \rightarrow A_u)\psi \rangle$
0	1.00000	1.00000
1	.99993	.99995
2	.99990	.99992
3	.99987	.99989
4	.99983	.99985
5	.99980	.99982
6	.99977	.99978
7	.99974	.99972
8	.99970	.99969
9	.99968	.99965

Table 7: Norm and overlap matrix elements for rotations over $n\pi$ in the $b_x = 3$ $b_y = 2$ case.

H. Angular Momentum Projection

The HF determinant $|\phi>$ is not necessarily an eigenfunction of J^2; however it is usual to interpret it as an intrinsic state. One associates then its rotational states with the real physical states. They are commonly obtained by use of the angular momentum projection operator technique (RS80)

$$|\phi^{LM}> = \sum_K g_K \hat{P}^L_{MK} |\phi> \tag{P25}$$

$$\hat{P}^L_{MK} = \frac{2L+1}{8\pi^2} \int D^{L*}_{MK}(\Omega) \hat{R}(\Omega) d\Omega \tag{P26}$$

Ω denotes the 3 Euler angles, $R(\Omega)$ the rotation operator

$$\hat{R}(\Omega) = e^{i\alpha\hat{L}_z} e^{i\beta\hat{L}_y} e^{i\gamma\hat{L}_z} \tag{P27}$$

in the convention of Edmonds (Ed57) and the Wigner functions $D^{L*}_{MK}(\Omega)$. The coefficients g_K are obtained by variation

$$\frac{\delta <\phi^{LM}|\hat{H}|\phi^{LM}>}{<\phi^{LM}|\phi^{LM}>} = 0$$

resulting in the equations

$$\sum_{K'} (H^L_{KK'} - E^L N^L_{KK'}) g_{K'} = 0 \tag{P28}$$

with

$$H^L_{KK'} = <\phi|\hat{H}\ \hat{P}^L_{KK'}|\phi> \tag{P29}$$

$$N^{L}_{KK'} = \langle\phi|\hat{P}^{L}_{KK'}|\phi\rangle \tag{P30}$$

We will now assume the following symmetry properties of the wave function $|\phi\rangle$

$\hat{P}_x|\phi\rangle = |\phi\rangle$	As 1
$\hat{P}_y|\phi\rangle = |\phi\rangle$	As 2

Since $\hat{P}_z|\phi\rangle$ can be calculated exactly on the grid we define

$$\hat{P}_z|\phi\rangle = |\bar{\phi}\rangle \tag{P31}$$

then the matrix elements (P29) and (P30) can be reduced to

$$\langle\phi|\hat{H}\hat{P}^{L}_{KK'}|\phi\rangle = \frac{2L+1}{8\pi^2}\int_0^{\pi/2} d\alpha \int_0^{\pi/2} \sin\beta d\beta \int_{-\alpha}^{+\alpha} d\gamma \{1+(-1)^K+(-1)^{K'}+(-1)^{K+K'}\}$$

$$\times \{ D^{L}_{KK'}(\alpha\beta\gamma)\langle\phi|\hat{H}\hat{R}(\alpha\beta\gamma)|\phi\rangle + (-1)^L e^{-i(\alpha K-\gamma K')} d^{L}_{K',-K}(\beta)\langle\bar{\phi}|\hat{H}\hat{R}(\alpha\beta\gamma)|\phi\rangle$$

$$+ D^{L}_{KK'}(\gamma\beta\alpha)\langle\bar{\phi}|\hat{H}\hat{R}(\alpha\beta\gamma)|\bar{\phi}\rangle + (-1)^L e^{-i(\alpha K'-\gamma K)} d^{L}_{K',-K}(\beta)\langle\phi|\hat{H}\hat{R}(\alpha\beta\gamma)|\bar{\phi}\rangle$$

$$+ \text{hermitian conjugate } \} \tag{P32}$$

which shows that under assumptions As 1 and As 2 both K and K' have to be even. In the case of axial symmetry

$$\hat{L}_z|\phi\rangle = M|\phi\rangle \tag{P33}$$

the integrations over α and γ vanish and one can write immediately for (P29) and (P30) (even without assumptions As 1 and As 2)

$$\langle\phi|\hat{H}\hat{P}^{L}_{KK'}|\phi\rangle = \delta(K-M)\delta(K'-M) \times \frac{2L+1}{2}$$

$$\{ \int_0^{\pi/2} \sin\beta \, d^{L}_{KK}(\beta) \langle\phi| e^{i\beta\hat{L}_y} \hat{H}|\phi\rangle d\beta \qquad (P34)$$

$$+ \int_0^{\pi/2} \sin\beta \, d^{L}_{K-K}(\beta)(-1)^{L-K} \langle\phi| e^{-i\beta\hat{L}_y} \hat{H}|\bar{\phi}\rangle d\beta \}$$

Since $K=K'=M$ the operator $\hat{P}^{L}_{KK}$ is now a hermitian projection operator such that the system of equations (P28) breaks down and only one g_M remains as norm factor.

For real wave functions only $M=0$ is possible such that

$$\boxed{\begin{aligned}\langle\phi|\hat{H}\hat{P}^{L}_{00}|\phi\rangle = \frac{2L+1}{2} \times \{ & \int_0^{\pi/2} \sin\beta \, d^{L}_{00}(\beta) \langle\phi|\hat{H} e^{i\beta\hat{L}_y}|\phi\rangle d\beta \\ & + (-1)^{L} \int_0^{\pi/2} \sin\beta \, d^{L}_{00}(\beta) \langle\phi|\hat{H} e^{-i\beta\hat{L}_y}|\bar{\phi}\rangle d\beta\}\end{aligned}} \qquad (P35)$$

Under assumption As 1 one has the further property

$$\langle\phi|\hat{H} e^{-i\beta\hat{L}_y}|\bar{\phi}\rangle = \langle\phi|\hat{H} e^{i\beta\hat{L}_y}|\bar{\phi}\rangle \qquad (P36)$$

I. Calculation of Matrix Elements $\langle\phi|H|\Psi\rangle$ with the BKN and Skyrme-Type Forces

1. Denoting the s.p. wave functions of the normalized Slater determinant ϕ by φ_α and those of Ψ by ψ_α then (Br65)

$$\langle\phi|\Psi\rangle = \det\{\langle\psi_\alpha|\psi_\beta\rangle\}^{-1/2} \quad \det\{\langle\varphi_\alpha|\varphi_\beta\rangle\}^{-1/2} \quad \det\{\langle\varphi_\alpha|\psi_\beta\rangle\} \qquad (P37)$$

$$\langle\phi|\hat{T}|\Psi\rangle = \langle\phi|\Psi\rangle \sum_{\alpha\beta} \langle\varphi_\alpha|\hat{t}|\psi_\beta\rangle (B^{-1})_{\beta\alpha} \tag{P38}$$

for $\hat{T} = \sum_\alpha \hat{t}_\alpha$ one particle operator, and the matrix B defined through

$$B_{\alpha\beta} = \langle\varphi_\alpha|\psi_\beta\rangle$$

$$\langle\phi|\hat{V}_2|\Psi\rangle = \frac{1}{2}\langle\phi|\Psi\rangle \sum_{\alpha\beta\gamma\delta} \langle\varphi_\alpha\varphi_\beta|\hat{v}^2|\psi_\gamma\psi_\delta\rangle \times \{(B^{-1})_{\gamma\alpha}(B^{-1})_{\delta\beta} - (B^{-1})_{\gamma\beta}(B^{-1})_{\delta\alpha}\} \tag{P39}$$

for $\hat{V}_2 = \sum_\alpha \sum_\beta \hat{v}^2_{\alpha\beta}$ 2 particle operator.

$$\begin{aligned}\langle\phi|\hat{V}_3|\Psi\rangle = \frac{1}{6}\langle\phi|\Psi\rangle \sum_{\alpha\beta\gamma\varepsilon\eta\xi} &\langle\varphi_\alpha\varphi_\beta\varphi_\gamma|\hat{v}^3|\psi_\varepsilon\psi_\eta\psi_\xi\rangle \\ &\times \{B^{-1}_{\varepsilon\alpha}B^{-1}_{\eta\beta}B^{-1}_{\xi\gamma} - B^{-1}_{\varepsilon\alpha}B^{-1}_{\eta\gamma}B^{-1}_{\xi\beta} - B^{-1}_{\varepsilon\gamma}B^{-1}_{\eta\beta}B^{-1}_{\xi\alpha} \\ &- B^{-1}_{\varepsilon\beta}B^{-1}_{\eta\alpha}B^{-1}_{\xi\gamma} + B^{-1}_{\varepsilon\gamma}B^{-1}_{\eta\alpha}B^{-1}_{\xi\beta} + B^{-1}_{\varepsilon\beta}B^{-1}_{\eta\gamma}B^{-1}_{\xi\alpha}\}\end{aligned} \tag{P40}$$

for $\hat{V}_3 = \sum_\alpha \sum_\beta \sum_\gamma \hat{v}^3_{\alpha\beta\gamma}$ 3 particle operator.

2. The BKN force is given by

$$\hat{V}_{BKN} \equiv \hat{T} + \hat{V}^2 + \hat{V}^3 = \sum_{i\neq j\neq k} v_{BKN}(ijk)$$

$$\begin{aligned}v_{BKN} = &-\frac{\hbar^2}{2m}\Delta_1 + t_0\,\delta(\bar{r}_1-\bar{r}_2) + V_0\,\frac{e^{-r_{12}/a}}{r_{12}/a} + \frac{1}{4}\,\frac{e^2}{r_{12}}\,(1+\tau_3(1))(1+\tau_3(2)) \\ &+ t_3\,\delta(\bar{r}_1-\bar{r}_2)\delta(\bar{r}_2-\bar{r}_3)\end{aligned} \tag{P41}$$

Assuming quartet symmetry, the indices i run only from 1 to 1/4 of the particle number and the dimension of the matrix B is also reduced with a factor 4

$$\langle\phi|\hat{T}|\Psi\rangle = 4 \times \langle\phi|\Psi\rangle \sum_{ij} \langle\varphi_i| - \frac{\hbar^2}{2m} \Delta \psi_j\rangle B^{-1}_{ji} \tag{P42}$$

$$\begin{aligned}\langle\phi|\hat{V}^2|\Psi\rangle &= 6 \times \langle\phi|\Psi\rangle t_o \int \tilde{\rho}^2(\bar{r})d\bar{r} \\ &+ 2 \times \langle\phi|\Psi\rangle e^2 \int \frac{\tilde{\rho}(\bar{r}_1)\tilde{\rho}(\bar{r}_2)}{r_{12}} d\bar{r}_1 d\bar{r}_2 \\ &+ 8 \times \langle\phi|\Psi\rangle V_o \int \tilde{\rho}(\bar{r}_1)\tilde{\rho}(\bar{r}_2) \frac{e^{-r_{12}/a}}{r_{12}/a} d\bar{r}_1 d\bar{r}_2\end{aligned} \tag{P43}$$

neglecting the exchange parts of the Coulomb and Yukawa contributions, and with $\tilde{\rho}$ given by

$$\begin{aligned}\tilde{\rho}(\bar{r}) &= \sum_{ik} \rho_{ik}(\bar{r}) B^{-1}_{ki} \\ \rho_{ik}(\bar{r}) &= \varphi^*_i(\bar{r})\psi_k(\bar{r})\end{aligned} \tag{P44}$$

and

$$\langle\phi|\hat{V}^3|\Psi\rangle = 4\langle\phi|\Psi\rangle t_3 \int \tilde{\rho}^{2+\alpha}(\bar{r})d\bar{r} \tag{P45}$$

3. In the case of the Skyrme forces for N-Z spin saturated nuclei in the LS coupling:

$$V_{Skyrme} = -\frac{\hbar^2}{2m}\Delta_1 + t_o\,\delta(\bar{r}_1-\bar{r}_2) + \frac{1}{2}t_1\{k'^2\delta(r_1-r_2) + k^2\delta(r_1-r_2)\} \tag{P46}$$

$$+ t_2\,\bar{k}'\cdot\bar{k}\,\delta(\bar{r}_1-\bar{r}_2) + t_3\delta(\bar{r}_1-\bar{r}_2)\delta(\bar{r}_1-\bar{r}_3)$$

one obtains

$$\langle\phi|\hat{H}|\Psi\rangle = \langle\phi|\Psi\rangle\cdot\int H(\bar{r})d\bar{r}$$

with the Hamiltonian density $H(\bar{r})$ given by

$$H(\bar{r}) = \frac{\hbar^2}{2m}\tau(\bar{r}) + 6t_o\tilde{\rho}^2 + 4t_3\tilde{\rho}^3 + (3t_1+5t_2)(\tilde{\rho}\tau+\tilde{j}^2) + \frac{1}{4}(9t_1-5t_2)(\nabla\tilde{\rho})^2 \tag{P47}$$

with $\tilde{\rho}(r)$ given by (P44)

$$\tau(\bar{r}) = \sum_{i,j}\nabla\varphi_i^*\cdot\nabla\psi_j(B^{-1})_{ji} \tag{P48}$$

$$\tilde{j}(\bar{r}) = \frac{1}{2}\sum_{i,j}(\varphi_i^*\nabla\psi_j - \nabla\varphi_i\,\psi_j^*)(B^{-1})_{ji}$$

J. Numerical Example

As a test example we take a ^{12}C nucleus constructed with harmonic oscillator wave functions and put the "pancake" with its symmetry axis in z-direction. The grid dimensions are $N_x = 17$, $N_y = 17$, $N_z = 31$. The oscillator width b is taken as $A^{1/6}$, and quartet symmetry is imposed.

The kernels (P29) and (P30) can be written as (P35) and since $|\bar{\phi}\rangle = |\phi\rangle$ we have to the analytic calculation:

$$N_{oo}^{L} = \frac{2L+1}{2}\left(1+(-1)^{L}\right)\int_{0}^{\pi/2} \sin\beta P_{\ell}(\cos\beta)\langle\phi|e^{i\beta\hat{L}_y}|\phi\rangle d\beta$$

$$= \frac{2L+1}{2}\left(1+(-1)^{L}\right)\int_{0}^{\pi/2} \sin\beta P_{\ell}(\cos\beta)\cos^{4}\beta d\beta$$

$$= \frac{2L+1}{2}\left(1+(-1)^{L}\right)\int_{0}^{1} x^{4} P_{\ell}(x) dx$$

$$= \frac{2L+1}{2}\left(1+(-1)^{L}\right)(-1)^{L/2}\frac{\Gamma(\frac{L}{2}-2)\Gamma(\frac{1}{2}+2)}{2\Gamma(-2)\Gamma(\frac{L}{2}+\frac{7}{2})}$$

Therefore

$$N_{oo}^{0} = 1/5$$
$$N_{oo}^{2} = 4/7$$
$$N_{oo}^{4} = 8/35$$
$$N_{oo}^{6} = 0$$

The approximate calculation performed on the grid makes use of the Gauss integration formula (AS64)

$$\int_a^b f(y)dy = \frac{b-a}{2} \sum_{i=1}^{N} w_i \, f(y_i) \qquad \text{(P49)}$$

with

$$y_i = \left(\frac{b-a}{2}\right)x_i + \frac{b+a}{2}$$

x_i is the ith zero of $P_N(x)$

$$w_i = \frac{2}{(1-x_i^2)} \left[P_N'(x_i)\right]^2$$

N is taken to be N = 16.

The calculation is performed for a grid size d = .7 fm and 1. fm, the results are shown in Table 8. A factor 10 improvement is obtained between the 2 sizes bringing the error down to an absolute value of 1.D-4. Note, however, that it is the better representation of the wave function on the grid which makes the improvement because the changing gridmesh has no influence on the matrix method itself. The increase of N=16 to N=24 does not show any change up to 1.D-5 in the d = .7 fm case neither for the norm as for the Hamilton kernel up till angular momentum L=16; the $H_{00}^{\downarrow}/N_{00}^{\downarrow}$ value, however, is constant up to 1.D-5 to L=4, for L=6 the change is already 1.D-3 and increases for higher L. It is indeed clear that for a more rapid oscillating function more discretization points are needed in (P49).

In Table 9 we make the same comparison for the matrix element (N=16)

$$n(\beta) = \langle\phi| e^{i\beta\hat{L}_y} |\phi\rangle = \cos^4\beta$$

The results confirm an improvement for the smaller grid and an increase in the relative error for increasing angles.

	analytic	d = .1 fm	d = .7 fm
N^0_{00}	.200000	.20067	.20005
N^2_{00}	.571429	.57216	.57149
N^4_{00}	.228571	.22738	.22848
N^6_{00}	.000000	-.00029	-.00003

Table 8: Comparison between the analytic calculation of the kernel N_{00} and the approximation on the grid for a harmonic oscillator ^{12}C nucleus for 2 different grid sizes.

ß (rad)	analytic	d = 1 fm	d = .7 fm
.008324	.9998614	.999862	.999861
.043531	.9962161	.996229	.996217
.105533	.9779313	.978005	.977937
.192105	.9284236	.928658	.928443
.300119	.8328399	.833365	.832884
.425673	.6880465	.688960	.688123
.564227	.5098371	.511107	.509941
.710776	.3298727	.331305	.329989
.860021	.1811812	.182486	.181285
1.006569	.0817797	.082730	.081854
1.145124	.0290750	.029618	.029117
1.270677	.0076387	.007873	.007657
1.378691	.0013288	.001400	.001334
1.465263	.0001231	.000136	.000124
1.527266	.0000036	.000005	.000004
1.562472	.0000000	.000000	.000000

Table 9: Comparison between the analytic calculation of the element n(ß) and the approximation on the grid.

K. Hartree-Fock Spectra of Deformed Light Nuclei with BKN, Modified BKN and Skyrme-Type Forces

Hartree-Fock calculations for ground state properties of nuclei base on a long-standing tradition. Systematic investigations have been performed with the Skyrme interaction and led to a satisfactory description of binding energies, radii, deformations ... of the ground states (Va72,Be75). Angular momentum projection in the Hartree-Fock theory has mainly been performed with various phenomenological density independent interactions (Bo69,Ri68). They led to a quite successful description of the rotational bands of light nuclei for which it is possible to take one Slater determinant for the intrinsic function (Bo69). A variation after projection should be done if one wants to minimize the energy of each projected state separately (Cu73).

Variation after projection calculations were performed for light nuclei like ^{8}Be, ^{12}C, ^{20}Ne and ^{24}Mg with the Skyrme-3 interaction by Caurier and Grammaticos (Ca77), in the LS coupling scheme. In a next paper (Ca80) they obtain an improvement for ^{12}C by adding a spin-orbit force with a strength of 90 MeV fm^5. However, even by realistic changes of the parameters of the force they are not able to get the right moment of inertia for ^{20}Ne. These too compressed spectra are a common feature in all projected Hartree-Fock calculations. We therefore want to investigate the differences in the spectra of these light nuclei by using different density-dependent Skyrme forces and the BKN-force. One additional advantage of a grid calculation is that there is no more the problem of choosing a large enough basis to construct the HF wave functions. Only axially symmetric configurations are considered in the LS coupling. Quartet symmetry is imposed and the exchange part of the Coulomb contribution is neglected as well as the exchange Yukawa part for the BKN-type forces. Fur-

thermore no corrections are performed to the centre-of-mass motion and to the problem of a non-rotational invariant Hamiltonian in the case of modified BKN (MBKN) and Skyrme a and M*. The parameters of the Skyrme forces are listed in Table 10.

	t_0	t_1	t_2	t_3	γ
Sk3 (Be75)	-1128.75	395.	-95.	14000.	1
Ska (Ko76)	-1602.78	570.88	-67.7	8000	1/3
SkM* (Ba82)	-2645	410	-135	15595	1/6

Table 10: Parameters of Skyrme forces.

They were chosen because of the increasing importance of the density-dependent term.

All calculations are performed on the $N_x=N_y=17$ and $N_z=31$ grid with a spacing of .8 fm and a corresponding E_{cut} value of 155 MeV to construct the HF wave functions. The full angular momentum projection of ^{20}Ne using 24 discrete angles takes 22.7 seconds on the CRAY X-MP. The absolute binding energies and the moments of inertia of each level with respect to the $\ell=0$ state are tabulated in Table 11. The MBKN force leads in all cases to the strongest binding. The smallest moment of inertia is obtained with the BKN force except for the $\ell=2$ level in the axial prolate configuration of ^{24}Mg.

The spectra are compared with the experimental spectra in Fig. 2. For ^{24}Mg we compare with the ground state band which is known to be mostly K=0.

Only in the case of the axial oblate configuration of ^{24}Mg there is a clear difference between the interactions. Although the position of the $\ell=2$ is quite stable, BKN gives a spacing of .43 MeV between $\ell=2$ and $\ell=4$ whereas for Ska only .02 MeV is obtained.

	E_o	θ_2	θ_4	θ_6	θ_8	θ_{10}
			^{12}C $(000)^4$ $(100)^4$ $(010)^4$			
BKN	-74.83	58.1	49.6			
MBKN	-76.27	66.5	65.4			
Sk3	-71.50	72.2	60.2			
Ska	-71.61	71.5	62.0			
SkM*	-71.56	75.5	66.7			
			^{20}Ne $(000)^4$ $(100)^4$ $(010)^4$ $(001)^4$ $(002)^4$			
BKN	-144.74	173.6	159.2	136.5	108.2	
MBKN	-152.87	201.9	184.5	152.5	115.2	
Sk3	-140.50	200.4	179.5	152.8	119.2	
Ska	-140.52	182.5	168.5	147.1	117.4	
SkM*	-140.01	193.5	177.2	152.7	120.7	
			^{24}Mg $(000)^4$ $(100)^4$ $(010)^4$ $(001)^4$ $(101)^4$ $(011)^4$			
			axial prolate			
BKN	-162.77	211.6	406.5	504.6	434.0	443.2
MBKN	-162.66	204.5	581.4	781.8	754.8	823.6
Sk3	-159.21	208.0	555.5	880.1	683.7	823.7
Ska	-158.18	162.0	526.3	997.4	758.0	1078.6
SkM*	-158.32	189.4	532.1	839.4	695.1	875.8
			^{24}Mg $(000)^4$ $(100)^4$ $(010)^4$ $(001)^4$ $(002)^4$ $(003)^4$			
			axial oblate			
BKN	-167.23	227.7	226.2	223.9	220.9	217.2
MBKN	-175.94	246.1	244.1	241.1	237.1	232.3
Sk3	-159.27	258.2	256.4	253.6	250.0	245.6
Ska	-159.69	252.3	250.4	247.6	243.9	239.4
SkM*	-159.46	265.3	263.5	260.7	257.1	252.6
	^{28}Si $(000)^4$	$(100)^4$	$(010)^4$	$(001)^4$	$(002)^4$	$(101)^4$ $(011)^4$
BKN	-214.79	153.5	149.7	143.9	136.4	127.6
MBKN	-228.05	190.4	184.7	175.8	163.8	149.3
Sk3	-212.51	181.5	176.7	169.2	159.6	148.6
Ska	-212.29	187.2	182.5	175.1	165.4	154.0
SkM*	-209.60	201.3	196.1	187.9	176.9	163.6

Table 11: Moments of inertia and absolute binding energies of some light nuclei with different interactions. The initial harmonic oscillator wave function, to be used in the ATDHF-procedure, is indicated by $(n_x n_y n_z)$.

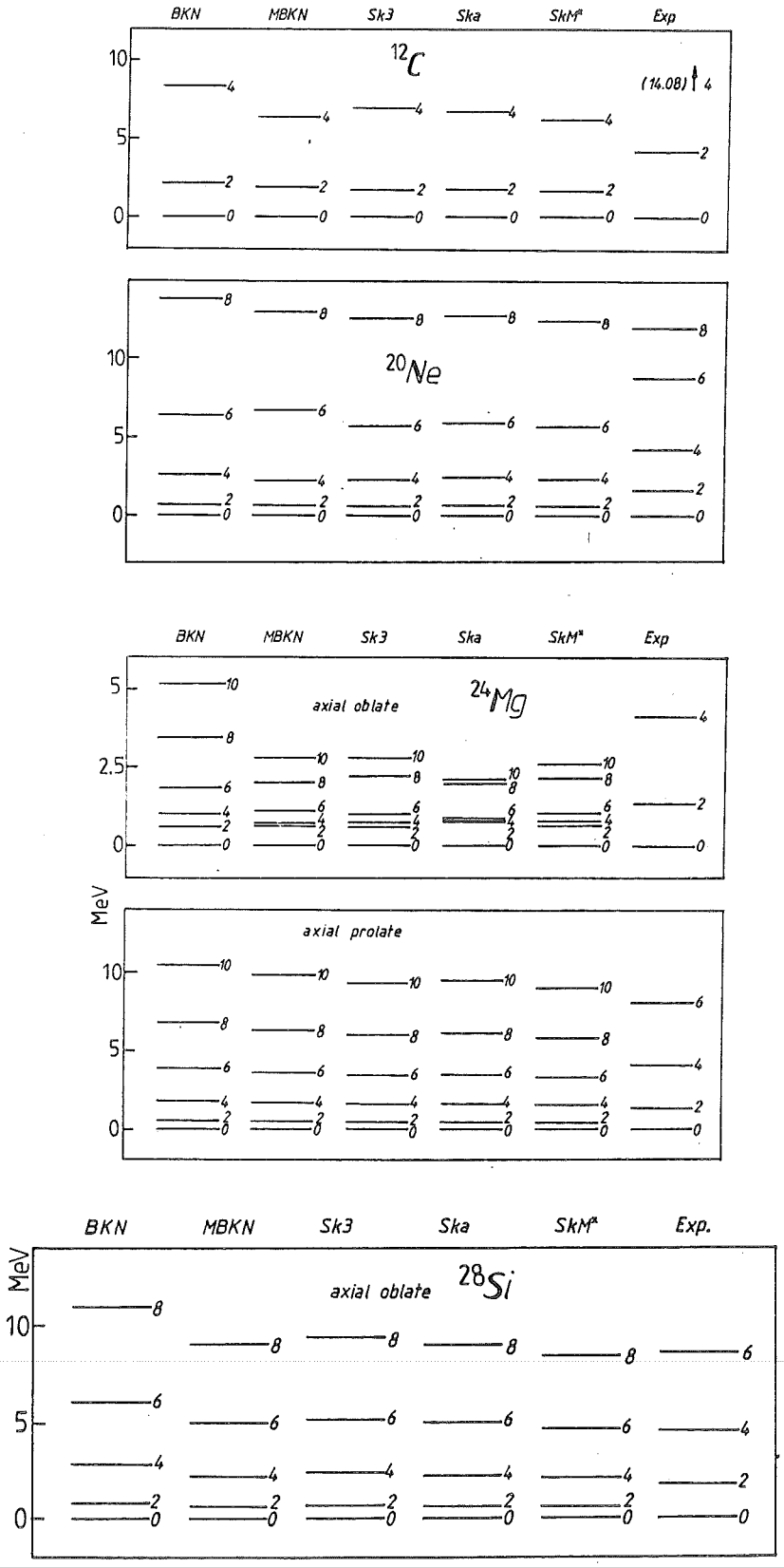
BKN
MBKN
Sk3
Ska
SkM*
Exp
12C
(14.08)
20Ne
24Mg
axial oblate
axial prolate
28Si
MeV
10
5
2.5
0

Fig. 2

Concerning the Skyrme forces only, there seems to be no systematics neither in binding energy nor in the moments of inertia.

In Table 12 we compare the N^L_{00} values for ^{12}C, ^{20}Ne and ^{28}Si for BKN and SkM* with the ones obtained by Ripka (Ri68) using a deformed harmonic oscillator with spin-orbit and ℓ^2 corrections. The BKN force favours the higher L contributions in comparison to SkM* or Ripka. The calculation of Ripka gives for every case a bigger contribution for L=0 and L=2 than our calculation. As is clear from Fig. 2 all calculated spectra are compressed with respect to the experimental spectra. This illustrates a shortage of the present interaction and/or the need of a variation after projection calculation.

	^{12}C			^{20}Ne			^{28}Si		
L	BKN	SkM*	Ri68	BKN	SkM*	Ri68	BKN	SkM*	Ri68
0	.179	.186	.230	.083	.093	.109	.061	.064	.079
2	.534	.548	.582	.325	.355	.398	.253	.264	.313
4	.258	.248	.188	.331	.335	.336	.298	.304	.326
6	.027	.018	0	.186	.165	.134	.219	.216	.194
8	.002	.001	0	.061	.045	.022	.112	.105	.071

Table 12: N^L_{00} contributions to the intrinsic HF wave functions are compared with the calculation of Ripka (Ri68).

Appendix A2

Elimination of Linear Dependence in the GCM Matrix Equation

To eliminate the linear dependences two procedures can be used which are equivalent for exact linear dependence:

1. First diagonalize then eliminate (Ch78).

Suppose we have an original dimension of the problem n. The first step is the diagonalization of the norm matrix N to the diagonal matrix D

$$G^T N\ G = D \tag{E1}$$

$$G^T\ G\ = 1 \tag{E2}$$

For exact linear dependence some of the eigenvalues in D will be zero. Due to numerical errors one will however compute small positive and negative eigenvalues.

With some appropriate cut-off parameter, see Deumens (De82), one throws away these small eigenvalues. One is then left with a problem of smaller dimension $\tilde{n}$

$$\tilde{G}^T\ N\ \tilde{G} = \tilde{D} \tag{E3}$$

where $\tilde{D}$ is now an $\tilde{n}\times\tilde{n}$ matrix and the dimension of $\tilde{G}$ is $n\times\tilde{n}$. The original GCM equation

$$(H-E\ N)f = 0 \tag{E4}$$

is multiplied with $\tilde{D}^{-1/2} \cdot \tilde{G}^T$ and because $\tilde{D}^{-1/2}\tilde{G}^T\ N\ \tilde{G}\tilde{D}^{-1/2} = 1$ one arrives at the following matrix equation

$$(\tilde{D}^{-1/2}\tilde{G}^{T}\ H\ \tilde{G}\tilde{D}^{-1/2}-E1)\tilde{D}^{1/2}\tilde{G}^{T}\ f\ =\ 0 \qquad \text{(E5)}$$

which has to be solved.

2. First eliminate then diagonalize (IBM).

Suppose we would like to eliminate the linear dependent rows and columns from the input matrices. As a first step one pivotes the input nxn matrix to H^1. Then one makes use of the unique decomposition

$$\begin{pmatrix} h^1_{11} & H^1_{12} \\ H^1_{21} & H^1_{22} \end{pmatrix} = \begin{pmatrix} 1 & 0 \\ L^1_{21} & 1 \end{pmatrix} \times \begin{pmatrix} 1 & 0 \\ 0 & D^1_{22} \end{pmatrix} \times \begin{pmatrix} u^1_{11} & U^1_{12} \\ 0 & 1 \end{pmatrix} \qquad \text{(E6)}$$

with

$$\begin{aligned} u^1_{1k} &= h^1_{1k} && k = 1,\ldots,n \\ \ell^1_{i1} &= \frac{h^1_{i1}}{h^1_{11}} && i = 1,\ldots,n \\ d^1_{ik} &= h^1_{ik} - \frac{h^1_{i1}\times h^1_{1k}}{h^1_{11}} && i = 2,\ldots,n \\ & && k = 2,\ldots,n \end{aligned} \qquad \text{(E7)}$$

The next step is pivoting the matrix D^1_{22} such that one arrives to an interchanged matrix H^2. The matrix D^2_{22} is now decomposed according to (E6) and one ends up with

$$H^2 = \begin{pmatrix} 1 & 0 & 0 \\ \ell^2_{21} & 1 & 0 \\ L^2_{31} & L^2_{32} & 1 \end{pmatrix} \times \begin{pmatrix} 1 & 0 & 0 \\ 0 & 1 & 0 \\ 0 & 0 & D^2_{33} \end{pmatrix} \times \begin{pmatrix} u^1_{11} & u^2_{12} & U^2_{13} \\ 0 & u^2_{22} & U^2_{23} \\ 0 & 0 & 1 \end{pmatrix} \qquad \text{(E8)}$$

The same procedure is continued until all elements of $D^r_{r+1,r+1}$ are smaller than some estimated cut-off parameter, see (De82). From this, one can conclude that the rank of the input matrix H is r.

Neglecting these small terms one arrives at

$$H^r = \underbrace{\begin{pmatrix} 1 & 0 & \dots & 0 \\ \ell^2_{21} & 1 & \dots & 0 \\ \ell^3_{31} & \ell^3_{32} & 1 & \dots 0 \\ \vdots & \vdots & \vdots & \vdots \\ \ell^r_{r1} & \ell^r_{r2} & & 1 \\ L^r_{r+1,1} & \dots & \dots & L^r_{r+1,r} \end{pmatrix}}_{n\times r} \underbrace{\begin{pmatrix} u^1_{11} & u^2_{12} & \dots & u^r_{1r} & U^r_{1r+1} \\ 0 & u^2_{22} & \dots & u^r_{2r} & U^r_{2r+1} \\ \vdots & \vdots & \vdots & \vdots & \vdots \\ 0 & \dots & 0 & u^r_{rr} & U^r_{r,r+1} \end{pmatrix}}_{r\times n} \qquad \text{(E9)}$$

To know the linear dependences between the different rows (or columns) one writes down the following matrix equation:

$$H^r X^r = B^r \qquad \text{(E10)}$$

Inserting (E9) and partitioning X^r to $\begin{pmatrix} x_1 \\ x_2 \end{pmatrix}$, B^r to $\begin{pmatrix} B_1 \\ B_2 \end{pmatrix}$ and H^r to $\begin{pmatrix} L \\ LR \end{pmatrix} \cdot (U\ UR)$:

$$\begin{aligned} L\cdot U\cdot X_1 + L\cdot UR\cdot X_2 &= R1 \\ LR\cdot U\cdot X_1 + LR\cdot UR\cdot X_2 &= R2 \end{aligned} \qquad \text{(E11)}$$

Since L and U are invertible one has

$$R_2 = LR\cdot L^{-1}\cdot R1 \qquad \text{(E12)}$$

and the same should hold for the input matrix H^r on the left side of (E10).

Conclusions

Until now, most of the microscopic approaches towards the description of large amplitude collective motions in nuclei aim to reduce the complicated many-body problem to a simpler one in terms of a few collective coordinates; e.g. relative distance of heavy ions during their collision or necking and elongation in a fission process.

About ten years ago, a new impulse was introduced due to the desire of determining, instead of an educated guess, the collective degrees of freedom and the associated mass parameters and potentials by a detailed study of the many-body dynamics of the collective motion.

The most promising theories in this direction use Slater determinants and are mainly based on the time-dependent Hartree-Fock dynamics. Rowe and Bassermann, Villars, Goeke and Reinhard, Baranger and Véneroni have presented theories based on these concepts. Similar attempts have been made by Holzwarth, Yukawa and Marumori. These various approaches give, in principle, a prescription for the derivation of a family of Slater determinants from which the collective Hamiltonian is to be extracted by means of a proper quantization procedure. However, the prescriptions differ from each other and one should test their validity in calculating observables of realistic nuclear systems. Actually, the Goeke and Reinhard prescription has been shown to be suitable for a numerical treatment, however, a direct and thorough comparison with experiment was still missing. Hence it was the aim of this work to build a bridge between this theory and the observables by means of appropriate many body techniques particularly designed to be used on three dimensional grids. To this end we have studied three different nuclear systems within the quantized adiabatic

time-dependent Hartree-Fock formalism from the structural and dynamical point of view.

The collective Schrödinger equation, with the classical potential and the added quantum corrections and a centrifugal term, has been solved for scattering and bound states. The BKN type interactions do not lead to enough binding energy for the ^{20}Ne system but it turns out that qATDHF provides a reasonable description for the ground state rotational band of ^{20}Ne. In addition, the experimental elastic differential scattering cross sections for α on ^{16}O are well reproduced. Although there are no free parameters in the formalism the theoretical results are at least as good as the Woods-Saxon best fits to the data.

In order to conserve explicitly the rotational symmetries of the physical system, we have also inserted the qATDHF wave functions into the GCM formalism. The kernels have been calculated with the angular momentum projection technique proposed by D. Baye and P.-H. Heenen. The method, which is meant for wave functions represented on a grid, has been tested by applications to rotational bands and heavy ion collisions.

It is an important result of this thesis that the combination of qATDHF with GCM and angular momentum projection is indeed technically feasible and allows without further approximations the evaluation of relevant observables. With the qATDHF wave functions of the α-^{16}O collective path and the BKN interaction we obtain in this way stable phase shifts which are similar to those in the literature. In case of the α-α-system they reproduce the experimental data up to an energy of 20 MeV. However, if we insert, on the other hand, the model wave functions of the HF sudden approximation drastic changes occur. This is an indication that the use of density-dependent interactions also requests

more appropriate model wave functions which reflect fully the dynamical aspects of a heavy ion collision, see also (Gi86). This sheds some interesting light on many results in the literature which are obtained within the sudden approximation using harmonic oscillator type wave functions.

Attempts to improve the wave function of ^{20}Ne by including other structural configurations like α-^{12}C-α, besides the α-^{16}O one, were not successful. This is due to the properties of the forces used and since the present qATDHF procedure is constructed to describe the maximal decoupled lowest energy mode of the system. The distortion of the α-particles in the α-α scattering leads to resonance structures which might indicate that an α^* structure is contained in our qATDHF wave functions.

In summary, the above results show that it is indeed possible to connect general and symmetry conserving many body techniques to the qATDHF theory and to obtain in this way a pure microscopic framework which can be handled in a numerical way and allows for the evaluation of observables which are accessible to experiments. Since the theory does not contain any adjustable parameters all results obtained are only dependent on the effective nucleon-nucleon force and on the symmetries of the initial wave functions.

It is, however, clear from the examples, particularly for the system α-^{12}C, that a generalization to the coupling of more channels is still to be performed in order to study transfer, break up and other inelastic reactions. Furthermore, in all adiabatic theories, the usefulness of which we have shown by our results, the transition from an asymptotically well defined channel to the combined system is not yet understood when at least one of the fragments is deformed. In addition, also the statistical coupling of other open channels remains to be considered which would enable the description of an imaginary

part added to the collective potential. This seems to us the path to be followed towards a fully selfconsistent microscopic description of static and low energy dynamical nuclear properties.

References

(Aj83) F. Ajzenberg-Selove, Nucl. Phys. A392 (1983) 141

(Ak69) Y. Akiyama, A. Arima and T. Sebe, Nucl. Phys. A138 (1969) 273

(Ar67) A. Arima, H. Horiuchi, T. Sebe, Phys. Lett. 24B (1967) 129

(Ar81) F. Arickx, J. Broeckhove, E. Deumens, P. van Leuven, J. Comp. Phys. 39 (1981) 272

(AS64) M. Abramowitz and I. Stegun, Handbook of Mathematical Functions, New York (1964) p. 887

(AS77) F. Ajzenberg-Selove, Nucl. Phys. A281 (1977) 1

(Ba70) H. Bando, S. Nagata, Y. Yamamoto, Prog. Theor. Phys. 44 (1970) 646

(Ba72) C. Bardin, Y. Dandeu, L. Gauthier, J. Guillermin, T. Lena, J.M. Pernet, H.H. Wolter and T. Tamura, Comp. Phys. Comm. 3 (1972) 73

(Ba74) D. Baye, P.-H. Heenen, Nucl. Phys. A233 (1974) 304

(Ba77) D. Baye, P.-H. Heenen, Fizika 9, Suppl. 3 (1977) 1

(Ba78) M. Baranger and M. Véneroni, Ann. Phys. 114 (1978) 123

(Ba82) J. Bartel, P. Quentin, M. Brack, C. Guet, H.-B. Hakansson, Nucl. Phys. A386 (1982) 79

(Ba84) D. Baye, P.-H. Heenen, Phys. Rev. C29 (1984) 1056

(BD79) J. Broeckhove, E. Deumens, Z. Phys. A292 (1979) 243

(Be75) M. Beiner, H. Flocard, N.V. Giai, Ph. Quentin, Nucl. Phys. A238 (1975) 29

(Bo69) M. Bouten, Hartree-Fock Calculations for Light Nuclei, Theory of Nuclear Structure, Trieste Lectures (1969) p. 361

(Bo75) M. Bouten, P. van Leuven, Proc. 2nd Int. Seminar on the GCM for Nuclear Bound States and Reactions, Mol (1974)

(Bo76) P. Bonche, S. Koonin and J.W. Negele, Phys. Rev. C13 (1976) 1226

(Br65) D. Brink, Proc. Int. School of Physics "Enrico Fermi", Course 36 (1965) p. 247

(Br76) D.M. Brink, M.J. Giannoni, M. Véneroni, Nucl. Phys. A258 (1976) 237

(Br82) J. Broeckhove, doctoral dissertation 1982, RUCA, Antwerpen, The Sp(2,R) Model for the Nuclear Breathing Mode

(BR72) A.D. Bacher, F.G. Resmini, H.E. Conzett, R. de Swiniarski, H. Meiner, J. Ernst, Phys. Rev. Lett. 29 (1972) 1331

(Ca64) E.B. Carter, G.E. Mitchell, R.H. Davis, Phys. Rev. B133 (1964) 1421

(Ca77) E. Caurier, B. Grammaticos, Nucl. Phys. A279 (1977) 333

(Ca80) E. Caurier, B. Grammaticos, Phys. Lett. 92B (1980) 236

(Ch74) W.S. Chien, R.E. Brown, Phys. Rev. C10 (1974) 1767

(Ch78) P. Chattopadhyay, R.M. Dreizler, M. Trsic and M. Fink, Z. Phys. A285 (1978) 7

(CL84) Clustering aspects of nuclear structure, 4th Int. Conf. on Clustering Aspects of Nuclear Structure and Reactions, Chester 1984, ed. J.S. Lilley and H.A. Nagarajan

(Co59) J.C. Corelli et al., Phys. Rev. 116 (1959) 1184

(Cu73) R.Y. Cusson, H.G. Lee, Nucl. Phys. A211 (1973) 429

(Cu79) J. Cugnon, H. Doubre, H. Flocard, Nucl. Phys. A331 (1979) 213

(Da63) R.H. Davis, Proc. 3rd Conf. on Reactions between Complex Nuclei (1963) 61

(De82) E. Deumens, doctoral dissertation 1982, RUCA, Antwerpen, The Generator Coordinate Method and the Analysis of Resonances

(Di28) P.A.M. Dirac, Principles of Quantum Mechanics, Oxford Clarendon Press (1928)

(Di86) V. Dimitrov, B. Slavov, K. Goeke, P.-G. Reinhard, Nucl. Phys. to be published

(dT72) N.B. de Takacsy, Phys. Rev. C5 (1972) 1883

(Ed57) A.R. Edmonds, Angular Momentum in Quantum Mechanics, Princeton Univ. Press (1957)

(El79) J.P. Elliott and P.G. Dawber, Symmetry in Physics, The MacMillan Press Ltd. (1979)

(Fi76) H.R. Fiebig and A. Weiguny, Z. Phys. A279 (1976) 275

(Fi81) H.R. Fiebig, W. Timm, Ann. Phys. 134 (1981) 141

(Fl76) T. Fließbach, J. Phys. G, Vol. 2, no. 8 (1976) 531

(Fr65) W. Franz, Z. Phys. 184 (1965) 181

(Fr70) W. Franz, Quantentheorie, Springer Verlag (1970) 208

(Fr74) H. Friedrich, H. Hüsken and A. Weiguny, Nucl. Phys. A220 (1974) 125

(FT76) T. Fließbach, Z. Phys. A277 (1976) 151

(Fu77) H. Furutani, H. Horiuchi, R. Tamagaki, Fizika 9 Suppl. 2 (1977) 29

(Fu78) H. Furutani, H. Horiuchi, R. Tamagaki, Prog. Theor. Phys. 60 (1978) 307

(Fu79) Y. Fujiwara, Prog. Theor. Phys. 62 (1979) 122, 138

(Fu80) Y. Fujiwara, H. Horiuchi, K. Ikeda, M. Kamimura, K. Sato, Y. Suzuki and E. Negaki, Prog. Theor. Phys. Suppl. 68 (1980) 43, 109

(GG85) R. Gissler, K. Goeke, F. Grümmer, to be published

(Gi81) M.J. Giannoni, J. Math. Phys. 22 (1981) 352

(Gi85) R. Gissler, doctoral dissertation 1985, KFA Jülich

(Gi86) R. Gissler, D. Provoost, F. Grümmer, K. Goeke, Phys. Lett. 166B (1986) 385

(Go78) K. Goeke and P.-G. Reinhard, Ann. Phys. 112 (1978) 328

(Go80) K. Goeke and P.-G. Reinhard, Ann. Phys. 124 (1980) 249

(Go81) K. Goeke, P.-G. Reinhard and D.J. Rowe, Nucl. Phys. A359 (1981) 408

(Go83) K. Goeke, F. Grümmer, P.-G. Reinhard, Ann. Phys. 150 (1983) 504

(GW57) J.J. Griffin, J.A. Wheeler, Phys. Rev. 108 (1957) 311

(He56) N.P. Heydenburg, G.M. Temmer, Phys. Rev. 104 (1956) 123

(He76) P.-H. Heenen, Nucl. Phys. A272 (1976) 399

(HH77) H. Hüsken, Nucl. Phys. A291 (1977) 206

(Hi83) M.M. Hindi, J.H. Thomas, D.C. Radford and P.D. Parker, Phys. Rev. C27 (1983) 2902

(Ho68) H. Horiuchi and K. Ikeda, Prog. Theor. Phys. 40 (1968) 277

(Ho70) H. Horiushi, Prog. Theor. Phys. 43 (1970) 375

(Ho73) H. Horiuchi, Prog. Theor. Phys. 51 (1974) 745

(Hu74) H. Hüsken, Proc. 2nd Int. Seminar on the Generator Coordinate Method for Nuclear Bound States and Reactions, Mol, Sept. 1974, ed. M. Bouten and P. van Leuven, p. 122

(HU77) H. Hüsken, W. Wedekind, A. Weiguny, Nucl. Phys. A286 (1977) 163

(HW53) D.L. Hill, J.A. Wheeler, Phys. Rev. 89 (1953) 1102

(IBM) Subroutine DMFGR of the IBM Scientific Subroutine Package

(Ik68) K. Ikeda, N. Takigawa and H. Horiuchi, Suppl. Prog. Theor. Phys., Extra Number (1968) 464

(Ik72) K. Ikeda, T. Marumori, R. Tamagaki, H. Tanaka, Suppl. Prog. Theor. Phys., Extra Number (1968) 464

(Ko76) H.S. Köhler, Nucl. Phys. A258 (1976) 801

(La66) L. Landau and E. Lifschitz, Mécanique Quantique, MIR, Moscow (1966)

(La74) K. Langanke, Diplomarbeit, Münster (1974)

(La79) K. Langanke, J. Leutenantsmeyer, M. Stingl and A. Weiguny, Z. Phys. A291 (1979) 267

(Li80) M. Libert-Heinemann, D. Baye, P.-H. Heenen, Nucl. Phys. A339 (1980) 429

(Ma75) T. Matsuse, M. Kamimura, Y. Fukushima, Prog. Theor. Phys. 53 (1975) 706

(Ma83) S. Marcos, H. Flocard, P.-H. Heenen, Nucl. Phys. A410 (1983) 125

(Me67) M.K. Mehta, W.E. Hunt and R.H. Davis, Phys. Rev. 160 (1967) 791

(Mi64) G.E. Mitchell, E.B. Carter, R.H. Davis, Phys. Rev. B133 (1964) 1434

(Mi73) M.V. Mihailovic, M. Rosina, Ljubljana 1972, GCM for Nuclear Bound States and Reactions, Fizika Vol. 5 Suppl. 1973

(Mi76) Y. Mito and M. Kamimura, Prog. Theor. Phys. 56 (1976) 583

(Ne32) J. v. Neumann, Mathematische Grundlagen der Quantenmechanik, Springer Verlag, Berlin (1932)

(Ne75) F. Nemoto, Y. Yamamoto, H. Horiuchi, Y. Suzuki and K. Ikeda, Prog. Theor. Phys. 54 (1975) 104

(Ni58) R. Nilson, W.K. Jentschke, G.R. Briggs, R.O. Kerman, J.N. Snyder, Phys. Rev. 109 (1958) 850

(Ni71) L.C. Niem, P. Heiss, H.H. Hackenbroich, Z. Phys. 244 (1971) 346

(Ni85) M. Niklas, Diplomarbeit 1985, Wilhelms-Universität Münster

(Ra72) M. Rayet, Nucl. Phys. B38 (1972) 387

(Re72) G. Reidemeister, Nucl. Phys. A197 (1972) 631

(Re76) P.-G. Reinhard, Nucl. Phys. A261 (1976) 291

(Re78) P.-G. Reinhard and K. Goeke, Nucl. Phys. A312 (1978) 121

(Re79) P.-G. Reinhard and K. Goeke, Phys. Rev. C20 (1979) 1546

(Re84) P.-G. Reinhard, J. Friedrich, K. Goeke, F. Grümmer and D.H.E. Gross, Phys. Rev. C30 (1984) 878

(Ri68) G. Ripka, Advances in Nuclear Physics Vol. 1, Plenum Press, New York (1968)

(Ro60) B. Roth, K. Wildermuth, Nucl. Phys. 20 (1960) 10

(RS80) P. Ring and P. Schuck, The Nuclear Many-Body Problem, Springer Verlag, New York (1080) p. 473

(Sa69) S. Saito, Prog. Theor. Phys. 41 (1969) 705

(Sa79) S.J. Sanders, L.M. Martz and P.D. Parker, Phys. Rev. C20 (1979) 1743

(Sc73) J. Schwager, Nuov. Cim. 18A (1973) 787

(Sh60) R.K. Sheline and K. Wildermuth, Nucl. Phys. 21 (1960) 196

(Sm69) W.R. Smith, Comp. Phys. Comm. 1 (1969) 106

(Su74) Y. Suzuki, K. Ikeda, Prog. Theor. Phys. 51 (1974) 1621

(Su76) Y. Suzuki, Prog. Theor. Phys. 55 (1976) 1751

(Su78) Y. Suzuki, T. Ando, B. Imanishi, Nucl. Phys. A295 (1978) 365

(Ta73) F. Tanabe, A. Tohsaki, R. Tamagaki, Prog. Theor. Phys. 50 (1973) 1774

(Ta74) F. Tanabe and F. Nemoto, Prog. Theor. Phys. 51 (1974) 2009

(To63) T.A. Tombrello, L.S. Senhouse, Phys. Rev. 129 (1963) 2252

(Va72) D. Vautherin, D.M. Brink, Phys. Rev. C5 (1972) 626

(Vi77) F. Villars, Nucl. Phys. A285 (1977) 269

(VW38) C.F. von Weizsäcker, Naturwiss. 26 (1938) 209, 225

(We37) W. Wefelmeier, Naturwiss. 25 (1937) 525

(Wh37) J.A. Wheeler, Phys. Rev. 32 (1937) 1083

(Wi77) K. Wildermuth, Y.C. Tang, A Unified Theory of the Nucleus, 1977 (Vieweg, Braunschweig)

Acknowledgements

I wish to express my gratitude towards my promoters M. Bouten and K. Goeke for their support and the possibilities they offered to me. I am also indebted to F. Grümmer, R. Gissler and M. Niklas for their help and discussions in every-day problems and for their friendship.

Thanks also to the IIKW and the Kernforschungsanlage Jülich GmbH for their financial support.

Furthermore I may not forget to thank my colleagues of the Limburgs Universitair Centrum and the members of the theory group of IKP at KFA Jülich, E. Brökel for his help in practical computing problems and for drawing the figures and M. Heese for typing this manuscript.

I should also acknowledge the theory group of the Wilhelms-Universität Münster for making available their GCM scattering computer program.

B. Poelsema and K. Lenz of the IGV at KFA Jülich are gratefully acknowledged for my "bijstelling" towards experimental work in TEAS.